Characterizing the Effect of Reduced Gravity on Rover Wheel-Soil Interactions

Parna Niksirat

A Thesis
In
The Department
of
Electrical and Computer Engineering

Presented in Partial Fulfillment of the Requirements
For the Degree of Master of Applied Science (Electrical and Computer Engineering) at
Concordia University
Montreal, Quebec, Canada

December 2018

CONCORDIA UNIVERSITY

SCHOOL OF GRADUATE STUDIES

This is to certify that the thesis prepared

By: Parna Niksirat

Entitled: Characterizing the Effect of Reduced Gravity on Rover Wheel-Soil Interactions

and submitted in partial fulfillment of the requirements for the degree of

Master of Applied Science

Complies with the regulations of the University and meets the accepted standards with respect to originality and quality.

Signed by the final Examining Committee:

_____ Chair
Dr. Rastko Selmic

_____ Examiner, External
Dr. Adel Hanna To the Program

_____ Examiner
Dr. Rastko Selmic

_____ Supervisor
Krzysztof Skonieczny

Approved by: _____
Dr. W. E. Lynch, Chair
Department of Electrical and Computer Engineering

_____ 20_____ _____
Dr. Amir Asif, Dean
Gina Cody School of Engineering and
Computer Science

ABSTRACT

Characterizing the effect of reduced gravity on rover wheel-soil interactions

Parna Niksirat

The entrapment of the Mars Exploration Rover Spirit in soft regolith and the tears and punctures in the Mars Science Laboratory Curiosity rover's wheels demonstrate some of the current mobility challenges in granular terrains on extraterrestrial planetary surfaces.

Classical wheel-terrain interaction models used in the literature are unable to sufficiently predict the effects of reduced-gravity on rover performance. Several researchers today highlight the insufficient predictive power of classical terramechanics models for planetary rovers, thus implying a need to renew the experimental underpinnings of our theories. Only a single dataset has been reported in the literature for wheels driving in soil during reduced-g flights, and the actual data collected is limited. This thesis presents data that more than doubles the number of existing reduced-g wheel-soil interaction experiments for the study of terramechanics. One of the key contributions is that it includes the measurement of drawbar pull (i.e. net traction force) data as well as direct observation of wheel-soil interactions (through a glass sidewall), both for the first time ever in reduced gravity.

The experimentation campaign is designed to inform the upcoming ExoMars space mission, through the use of ExoMars wheel prototype and Martian soil simulant in simulated Martian gravity produced in parabolic flights. An advanced automated gantry system is developed to support this activity with improved control and repeatability over the prior published experiments. In addition to Martian gravity, wheel-soil interactions are also studied in Lunar gravity, all achieved aboard Canada's National Research Council's (NRC) Falcon 20 aircraft. Wheel rotation rate, horizon-

tal advance rate, and vertical wheel loading are controlled independently. To address the constraints imposed by testing aboard an aircraft performing parabolic flights and to achieve experimental repeatability and consistency, a novel rapid automated soil preparation subsystem is developed. The consistency and repeatability of the soil preparation is studied and verified both through cone penetration tests and through examining triplicates of terramechanics (i.e. traction force, wheel sinkage) datasets.

A key observation from the terramechanics dataset is a significant reduction of traction (over 30% less) in partial gravity experiments (PGE) compared to on-ground experiments (OGE), at the same wheel loading. The complementary visualization analysis results indicate that, with wheel normal load held equal between experiments, the amount of soil mobilized by wheel-soil interaction substantially increases as gravity decreases. The results of the visualization analysis suggest a deterioration in the soil strength at lower gravities, which thus undermines the rover mobility by reducing the net traction. The results have important implications regarding the practice of using a reduced-mass rover on Earth to assess the performance of a full-mass rover in similar soil on a reduced-gravity surface. Other details discovered in the dataset are also further elaborated in this study.

The analysis of terramechanics data and high-speed images that are collected at Lunar and Martian gravities, and contrasted against OGE, not only guide the understanding of the influence of gravity on wheel performance but also holds promise to fill the gaps of research in the literature. The congruity of analysis of computer vision/clustering techniques with terramechanics results in this campaign highlights a promising technique for studying these interactions in a planetary context. The richness of the data produced, unprecedented in the study of robot-terrain interactions, can highlight gaps and discrepancies in existing models and enables validation of new models that approach robot-terrain interactions with an appropriate and efficient level of detail.

Acknowledgements

I would like to express my appreciation to my supervisor Professor Skonieczny whom without his guidance, insightful comments, and encouragements this thesis would not be possible. I would like to thank Amir Nassiraei for his incredible technical/mechanical support and sharing his knowledge throughout this project. I would like to thank Tyson Boer in supporting software development for data collection for the flight campaign.

This project is undertaken with the financial support of the Canadian Space Agency. I am grateful to Steeve Montminy and Francis Martin at the Canadian Space Agency for their project guidance and technical structural analysis guidance, respectively. This project owes its progress to Canada's National Research Council Flight Research Laboratory. A special mention with respect to executing the flight experiments, goes to Derek Duff Gowanlock, for facilitating the parabolic flight campaign. I thank Michel van Winnendael at the European Space Agency and St'ephane Michaud at RUAG Space for support regarding Martian soil simulants, and MDA for the loan of a prototype ExoMars rover wheel.

I would like to express my sincere gratitude to my parents and my sister for supporting and encouraging me throughout my life and in whatever I pursue.

Contents

List of Tables

List of Figures

Nomenclature

$(p_1 - p_0)/(\zeta/2)(F/nF_c)^2$ Pressure drop in manifold

$k_{\phi}^{'}$ Frictional modulus of deformation

$k_c^{'}$ Cohesive modulus of deformation

$\dot{z}$ Sinkage velocity

η Newtonian viscosity

γ Soil bulk unit weight

μ_p Soil yielding constant

μ_v Soil Compression constant

ω Angular wheel velocity

ϕ Friction angle

σ_B Ultimate bearing capacity

τ Soil shear stress

A Wheel-soil contact patch area

B Width or the diameter of the foundation/footing

b Wheel's contact patch width

c Soil cohesion

c_f Stiffness

CI Cone index (cone penetrometer)

D Inner diameter of manifold

$D_{o,i}$ Outlet hole diameter

DP Drawbar pull

E Ratio of manifold length to diameter

F_{DP} Drawbar pull reaction force

F_n Normal load

G Cone index gradient

$I(x, y, t)$ Image intensity

$I_{m,i}$ Motor i current

j Shear deformation

k Shear modulus of deformation

k_ϕ Soil friction angle pressure-sinkage parameter

k_c Soil cohesion pressure-sinkage parameter

K_m Motor constant

L Distance between first and last open port

l Contact patch length

M Ratio of sum of all the port areas to area of manifold

n	Sinkage exponent
N_γ	Bearing capacity factor of effective unit weight
N_c	Bearing capacity factor of cohesion
N_q	Bearing capacity factor of overburden pressure
p	Pressure
q	Overburden pressure
R	Compaction resistance
r	Wheel radius
S	Slip
T	Thrust
u_n	Horizontal velocity of neighbouring pixel
V	Horizontal wheel velocity
v_c	Dimensionless volume flow rate in manifold ports
v_n	Vertical velocity of neighbouring pixel
W	Wheel loading
w	Dimensionless volume flow rate
W_D	Data term fixed window
$w_{i,j}$	Weighting matrix
W_s	Spatial term fixed window
X	Dimensionless position along manifold

x Axial coordinate along manifold

z Sinkage

Chapter 1

Introduction

The Global Exploration Roadmap identifies Mars, the Moon, and asteroids as priority destinations for space exploration [3]. The terrains of Mars and the Moon consist of fine granular regolith with embedded rocks, as do those of a recently discovered class of rubble-pile asteroids [24], [49]. Understanding the nature of interactions with granular terrains is thus crucial to exploring these high priority destinations. The entrapment of the Mars Exploration Rover Spirit in soft regolith (Figure 1.1) and the tears and punctures in the Mars Science Laboratory Curiosity rover's wheels (Figure 1.2) demonstrate some of the current mobility challenges of such granular terrains.

Figure 1.1: NASA's Mars Exploration Rover Spirit stuck during the rover's 2,099th sol. Image credit: NASA/JPL-Caltech

Figure 1.2: Punctures in the Curiosity rover wheel reduce rover mobility. Image credit: NASA/JPL-Caltech

At NASA's Jet Propulsion Laboratory engineers used a 3/8 th mass rover to try to replicate the conditions of Spirit's entrapment here on Earth. The extensive investigations attempted to resume Spirit driving. However, these test demonstrated that Earth-based experiments cannot exactly replicate the conditions on Mars (Figure 1.3).

Figure 1.3: Sandbox setup at NASA's Jet Propulsion Laboratory, Pasadena, Calif., where engineers used a 3/8 mass test rover to assess possible moves for getting Mars rover Spirit out of a patch of loose Martian soil. Image credit: NASA/JPL-Caltech

Martian soil is a fine regolith with a broad range of different properties in different contexts (Figure 1.4). To search for past and present life on Mars, there is a need to explore and gather information regarding geology, biology, habitability and climate on this planet. The areas on Mars identified as highest priority for exploration (that hold promise for finding evidence of organics, chemical building blocks of life and

(a) Mount Sharp

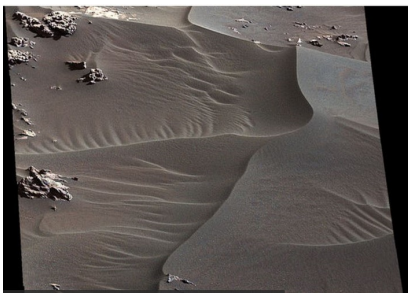

(b) Nectaris Montes sand dunes

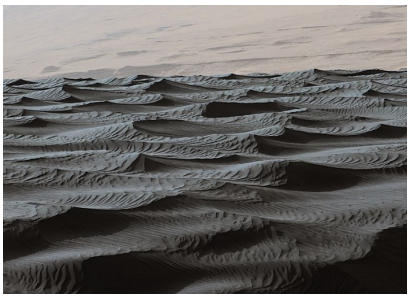

(c) Troughts of ripples

(d) Gale Crater

Figure 1.4: Soft terrains are common and widespread on Mars (a-d) Diversity of Martian terrains increase the possibility of rover entrapment. Soft terrains on Martian dunes are interesting to study and to search for life. Traverse through some interesting areas on Mars has not been done due to the risks of mission termination. Image credit: NASA/JPL-Caltech

potentially providing habitable conditions) are hazardous for the rovers as the wheel can easily slip on the loose soil and consequently get stuck. Subsequently, any path crossing loose soil becomes a difficult mission for the rover due to the existing mobility challenges. It is thus necessary to advance the state-of-the-art in rover mobility on granular terrains.

1.1 Literature Review

In this section, literature on the topics of terramechanics and experiments, machine-soil visualization, gravity-offloaded terramechanics, reduced-g terramechanics, reconciling reduced-g experiments with theory, and modern approaches in soil modeling are respectively discussed.

1.1.1 Terramechanics

The study of wheel-terrain interaction is called Terramechanics. The purpose of this field is to evaluate and hopefully predict the performance of off-road systems. Even though the wheel-soil interaction mechanics and the empirical models of the soil stress distributions beneath the wheel have been widely investigated, a model that consistently predicts wheel forces and torques accurately has not been developed. Therefore continued investigation of the contact and traction mechanics between wheels and soil is imperative for the successful operation of a rover on soft soil.

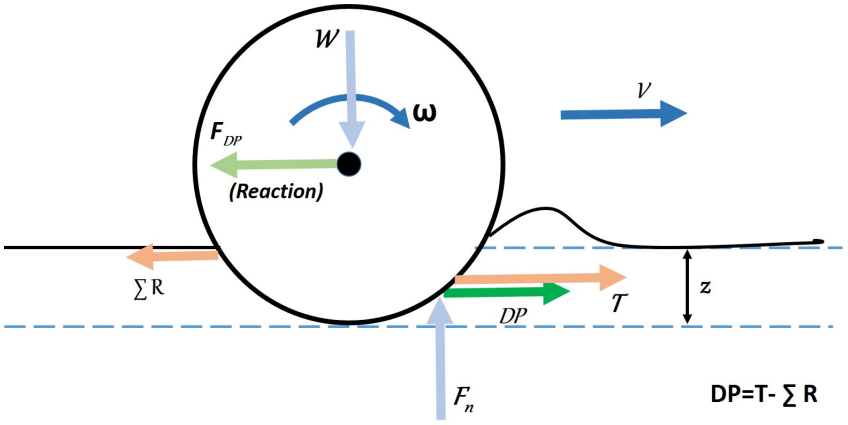

Figure 1.5: Forces acting on a driving wheel, and other relevant parameters. The wheel is driven with angular velocity, ω, ultimately causing forward velocity v.

In studying rover-terrain interaction, sinkage and drawbar pull (DP) parameters are used as mobility performance indicators. A rover wheel exerts a vertical load on the terrain, which leads to sinkage. Wheel sinkage can be composed of static and dynamic components. The static sinkage is induced by the vertical load on the wheel, while the sinkage produced by wheel rotation is called dynamic sinkage. Static sinkage is considered further here.

Bekker [7] proposed the following relationship between pressure, p, and sinkage, z:

$$p(z) = \left(\frac{k_c}{b} + k_\phi\right) z^n \tag{1.1}$$

Where the wheel's contact patch width is denoted as b. Soil parameters k_c and k_ϕ, and the sinkage exponent n, in pressure-sinkage formulations are based on empirical study found though infield testing with an instrument called a bevameter (Figure 1.6). Examples of fitted data are shown in Figure 1.7.

Further, Bekker proposed a relationship for sinkage as a function of normal load (equation (1.2)) and compaction resistance, R, as a function of sinkage for rigid wheels (equation (1.3)):

$$z = \left[\frac{3F_n}{b(3-n)(k_c/b + k_\phi)\sqrt{2r}}\right]^{2/(2n+1)} \tag{1.2}$$

$$R = b\left[(\frac{k_c}{b} + k_\phi)\frac{z^{n+1}}{n+1}\right] \tag{1.3}$$

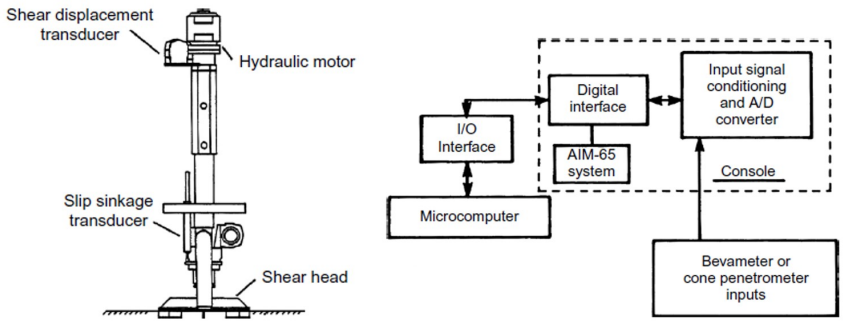

Figure 1.6: Schematic diagram of a bevameter used for extracting terrain parameters and block diagram of terrain data acquisition process [71].

In equation 1.2, F_n is the normal load on the wheel, and r is wheel radius.

Reece [47] proposed that the pressure-sinkage relationship can also be expressed as a function of two dimensionless coefficients $\acute{k}_c$ (cohesive modulus of deformation) and $\acute{k}_\phi$ (frictional modulus of deformation) such that

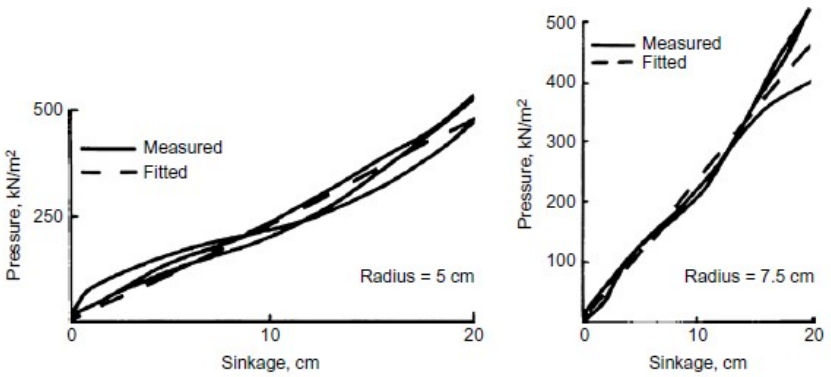

Figure 1.7: Example of pressure-sinkage curves; for wheels of radius 5 & 7.5 cm (fitted curves use the pressure-sinkage formula by Bekker) [71].

$$p(z) = \left(c\acute{k}_c + \gamma b\acute{k}_\phi \right) (\frac{z}{b})^n \tag{1.4}$$

Where c is cohesion and γ is soil bulk unit weight.

Apfelbeck et al. [4] investigated the influence of the Bevameter test setup and an appropriate soil preparation methods. The results indicated that different penetration velocities and different penetration tool dimensions affect the pressure-sinkage relationship. Accomplishing a reliable and consistent characterization of soft soil is very challenging, since the soil parameter determination often is influenced to a large extent by several testing practices, and the soil preparation method. These issues make the terrain parameter identification intricate. Applying soil parameters identified with improper testing and initial setup compromise the validity and accuracy of the models.

A driving rover applies shear load to the terrain surface, which results in generation of thrust and corresponding slip. Slip, S, is a function of body velocity, V, and rotational velocity, ω, (see equation 1.5).

$$S = 1 - \frac{V}{r\ \omega} \tag{1.5}$$

Wheel thrust is a force vector in the direction of wheel heading that is related to the wheel's contact patch with the terrain surface and the pressure at that contact area (equation (1.6)). Moreover, thrust force depends on the wheel slip where the characteristic of this relationship will be discussed later in this section. The maximum thrust, T_{max}, that can be generated on a contact area, A, is:

$$T_{max} = \tau A \tag{1.6}$$

where τ is shear stress calculated based on Mohr-Coulomb criterion (equation (1.7)) in which the failure in terrain is considered the transition point from the state of plastic equilibrium to that of plastic flow.

$$\tau = c + \sigma tan(\phi) \tag{1.7}$$

σ is the normal stress on the terrain and the product of σA corresponds to the normal load on the terrain. Thus, equation (1.8) indicates that on the frictional soil thrust is a function of normal load and angle of internal friction whereas on cohesive soil the thrust is more dominated by the contact area of the wheel with the terrain.

$$T_{max} = cA + Wtan(\phi) \tag{1.8}$$

Thrust as a function of slip can be estimated as in equation (1.9), where S represents slip, $\tilde{x}$ is a point located along the contact patch (from 0 at the front to l at the full length of the patch), and k is the shear modulus of deformation.

It is based on an assumption of experimentally asymptotic approach to the soil's max shear strength as a function of shear displacement (which is related to slip). *p(x̃)* can be related to *p(z)* (equation (1.1) or (1.4)) based on wheel contact patch geometry.

$$T = b \int_0^l (c + p(\tilde{x})\ tan(\phi))(1 - e^{-S\tilde{x}/k}) d\tilde{x} \tag{1.9}$$

Drawbar pull is a developed net force assisting the driving rover. Under steady state operating conditions, this force is defined as the difference between the thrust and the sum of all resisting forces acting on the rover (see Figure 1.5); the formulation will be discussed further in Chapter 3.

Bekker [7] developed semi-empirical methods for terramchanics applications based on experimental observations and theoretical formulations estimating the drawbar pull as a function of slip, combining equations (1.1) through (1.9). Other predictive models exist, but in general DP vs slip curve is central in characterizing a wheel's terramechanics performance. Examples of thrust vs. slip and DP vs. slip are shown in Figure 1.8 and Figure 1.9, respectively.

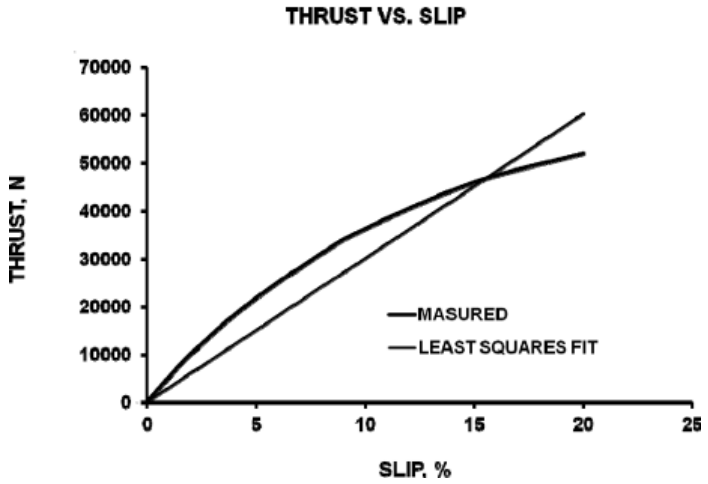

Figure 1.8: Example of thrust force as a function of slip ratio [73]

There are several studies pertaining to traction of a wheel on loose soil; however, not all studies focus on DP, which is obtained through a particular type of control denoted as slip control. The slip control single-wheel test is compared and contrasted to other options, such as the free-slip test, in depth in Chapter 3.

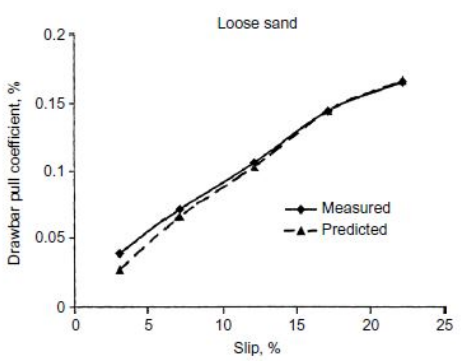

(a) DP coefficient vs slip on loose sand

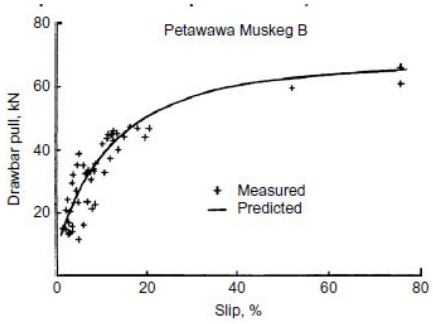

(b) DP vs slip on Muskeg B terrain

Figure 1.9: Different methods exist for predicting the drawbar pull, depending on the terrain type and slip (a) Measured drawbar pull coefficient of a rigid wheel on loose sand, and predicted obtained using the finite element method (DP coefficient is normalized $\frac{DP}{W}$) (b) Measured and predicted drawbar performance by computed method on Muskeg soil [71].

The ultimate bearing capacity of soil is the maximum pressure that can be supported without failure. Terzaghi's formulation of soil bearing capacity is in equation (1.10) and consists of three terms; the first term in the equation is related to cohesion of the soil, the second term is related to the overburden pressure, q (which is a product of density and depth of the footing $\gamma\ D$), and the third term is related to the width of the footing, B, and therefore the length of shear stress area (γB) [63]. N_c, N_q, N_γ, are the bearing capacity factors which are the functions of internal friction angle, ϕ (see equation (1.11)).

$$\sigma_B = cN_c + qN_q + \gamma BN_\gamma \tag{1.10}$$

$$N_\gamma = \frac{2(N_q+1)tan(\phi)}{1+0.4sin(4\phi)}, N_c = \frac{N_q-1}{tan(\phi)}, N_q = \frac{e^{(1.5\pi-\phi)tan(\phi)}}{2cos^2(\pi/4+\phi/2)} \tag{1.11}$$

1.1.2 Terramechanics Experiments and Soil Preparation

Soil prepared with an unreliable preparation method as an input for terramechanics testing leads to inaccurate output results and consequently to incorrect predictive models. Therefore, an applicable and stable soil preparation method is indispensable.

A crucial element of robot-soil interaction experimentation is soil preparation, which consists of 3 elements: loosening, leveling, and compaction [20]. Repeatability of test results requires repeatability of initial soil conditions for the tests. Soil that has been disturbed by digging, penetration, or driving should be reset to its prior state. If not, the soil's prior stress history can affect later results; an example of this is the "multipass effect" observed if a wheel drives over the same soil more than once [36], [52].

Cone penetrometer tests are widely used as an indicator of soil conditions. These data can be used to obtain in-place shear strength characteristics of soil. Rahmatian et. al [45] describes the difficulties in adequate compaction and preparation for low-cohesion, and other, simulants.

1.1.3 Overview of Single-Wheel Testbeds

Single-wheel testbeds are very commonly used to study terramechanics in general, and for planetary rover wheels in particular.

Researchers at the Field and Space Robotics Laboratory (FSRL) of the Massachusetts Institute of Technology (MIT) developed the first single-wheel testbed for planetary rovers (see Figure 1.10a). The system measures vertical load and the tractive force acting on the wheel using a force-torque sensor. The slip ratio of the experimental wheel is controlled by the wheel's angular velocity and the carriage's traveling velocity.

Figure 1.10b shows a single wheel testbed at DLR, Germany, used for terramechanics experiments. Michaud et al. validated and improved the predictive capabilities of

terramechancis models for NASA MER using the single-wheel setup at DLR [38] and also used it to characterize ExoMars wheel sinkage, torque and DP [43]. Pantel et al. also used DLR apparatus to evaluate ExoMars rover wheel design terramechanics performance [42]. At Carnegie Mellon University, Skonieczny et al. performed studies with a single-wheel testbed (that included a novel terramechanics imaging technique; see the next subsection) to find the appropriate grouser spacing for rigid wheels [53] (Figure 1.10c). Liu et al. conducted experiments to analyze the effect of slip on tractive performance in loose sand [35]. Furthermore, they studied the effect of wheel design, with and without grousers, on motion performance (Figure 1.10d).

Ding et al. performed terramechanics experiments with different wheel geometries investigating the effect of wheel load, velocity and repetitive passing on mobility [22] (Figure 1.10e). Guo et al. proposed a new model to estimate the soil normal stress as a function of sinkage and wheel-soil contact angle [27]. Researchers at JAXA used a single-wheel testbed to study a new wheel design for sloped lunar terrain [30] (Figure 1.10f).

Jia et. al derived a wheel-terrain interaction model based on the stress distributions along the wheel-terrain interface, predicting the reaction forces exerted on the wheel while considering the forces and torques contributed by the bulldozing effect. The model then was verified by using single-wheel experiments [32] (Figure 1.10g).

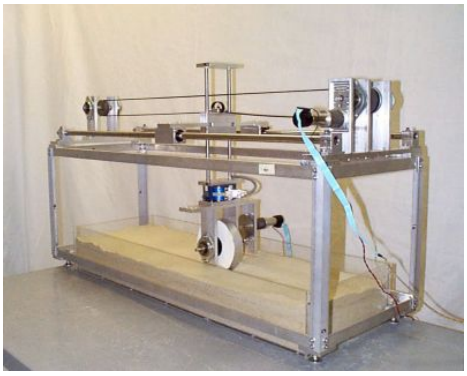

(a) Single-wheel testbed developed by MIT [51]

(b) Single-wheel testbed developed by DLR [38]

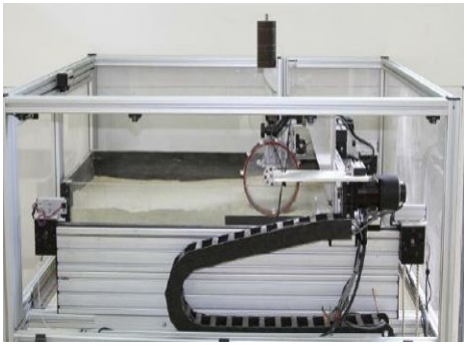

(c) Single-wheel testbed developed by CMU [53]

(d) Single-wheel testbed developed by Jilin University [35]

(e) Single-wheel testbed developed by HIT [22]

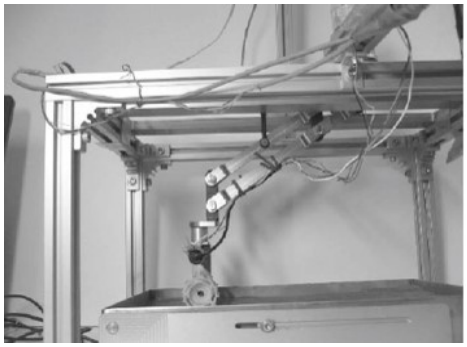

(f) Single-wheel testbed developed by Jaxa [30]

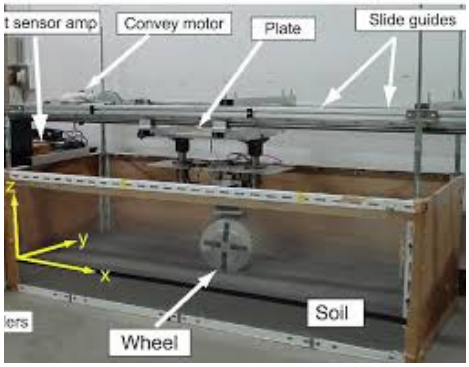

(g) Single-wheel testbed developed by Tokyo [32]

1.1.4 Machine-soil Visualization Experiments

The influence of wheel design parameters on soil motion have not generally been studied closely. Investigating the soil motion below the machine soil interface can provide insights beyond those that can be drawn from observing the soil surface. It is possible to observe such interactions through a glass-sided soil bin. Glass sidewalls have been used to directly observe and study the soil motion for terramchanics applications while the wheel drives along side of the glass wall [6]. A photographic method studied soil motion using long-exposure photos [28]. Other imaging techniques includes particle image velocimetry, and particle tracking velocimetry [40] [25]. However, these techniques impose limitations such as requiring specialized equipment (see Figure 1.11), and compromising between data resolution and accuracy. In these techniques, the images are divided into grids estimating per grid velocity. The technique described in [54], optical flow, is utilized here to estimate the velocity at each pixel without as significant a tradeoff between resolution and accuracy as other techniques. It is described in more detail in Section 3.2.

Researchers at the FSRL later adopted a similar particle image velocimetry (PIV) analysis [51] to study the soil kinematics under the wheel.

1.1.5 Gravity-offloaded Terramechanics Experiments

One way to try to capture the effect of gravity on rover mobility is with gravity offload, such as the Active Response Gravity Offload System (AFGOS) used by NASA to simulate partial gravity environments [18]. Raura et al. designed a Low-gravity Offset and Motion Assistance (LOMASS) (see Figure 1.12), which is an overhead automated gantry suspending the rover in the testbed [46] to simulate the reduced gravity environments. NASA JPL's 'SCARECROW' rover [68], whose $3/8^{\text{th}}$ mass loads the wheels equivalently to the full mass Curiosity rover on Mars, is another example of a way to achieve the equivalent of a gravity-offloaded system. In all these

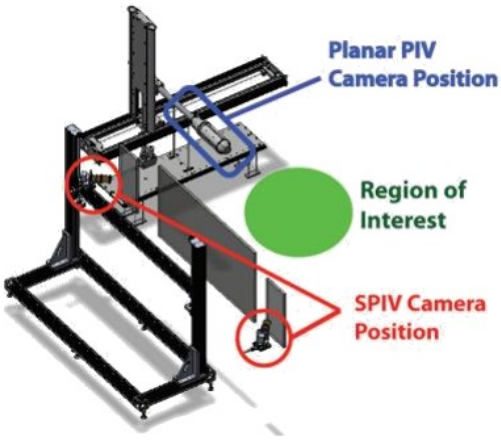

(a) Generic setup of particle image velocimetry [12].

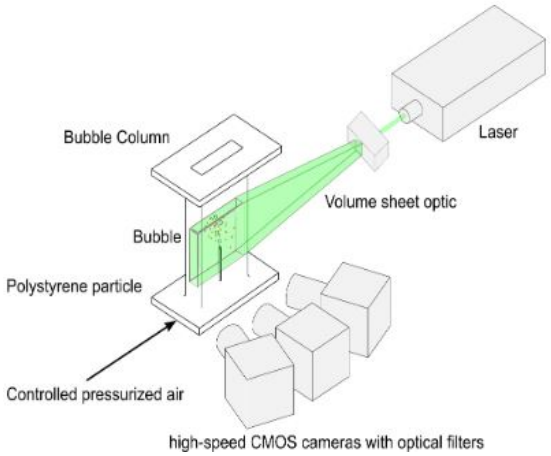

(b) Example setup of particle tracking velocimetry [57].

Figure 1.11: Optical method of flow visualization measuring velocity field by using the motion of the seeding particles (Eulerian method measures the velocity field in a grid). (b) Optical measurement technique estimating the velocity of flow by tracking particles (Lagrangian approach).

systems, although rover weight is properly adjusted, the effect of gravity on the soil particles themselves is not taken into account. Skonieczny et al. utilized gravity offload in robot excavation simulating lunar gravity (see Figure 1.13). Skonieczny et al. [55], [56] argue that gravity offload over-predicts mobility performance relative to reduced gravity.

1.1.6 Reduced-g Terramechanics Experiments

Flights aboard aircraft flying parabolic arcs are the best opportunity to achieve significant stretches of effectively reduced gravity in a controlled fashion without actually travelling to extraterrestrial surfaces. Only a single dataset has been described in the literature, by Kobayashi, for wheels driving in soil during reduced-g flights [34]. This dataset is based on a self-propelled wheel driving in FJS-1 lunar soil simulant and in Toyoura sand in a wide range of gravity conditions: 1/6 g, 1/2 g, 3/4 g, 1 g, and 2 g. The data collected includes horizontal travel distance, vertical sinkage,

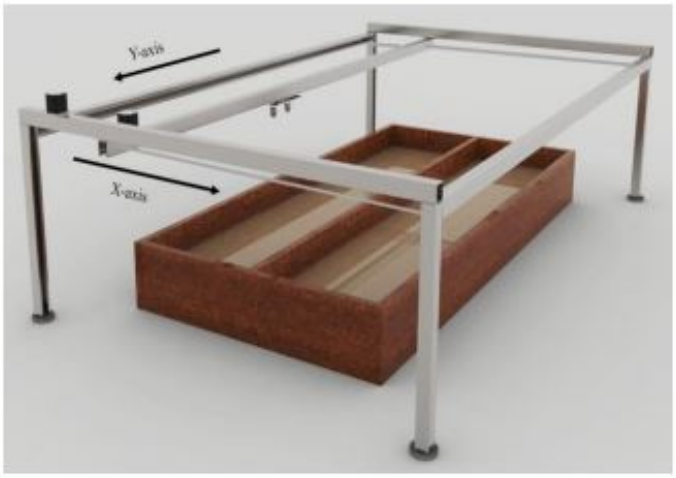

Figure 1.12: Low-gravity Offset and Motion Assistance and Simulation System (LOMASS) [46].

and wheel torque. The data is contrasted to a dataset collected in 1 g that is corresponding but with varying vertical load on the wheel (i.e. 1/6 W, 1/2 W, etc.). The difference between the experimental conditions in the two datasets is the effect of gravity on the soil particles themselves. Kobayashi's key observation is that wheel travel is impaired when both the wheel and soil are in reduced gravity, rather than improving as it does when just the load on the wheel is reduced [34]. Kobayashi's experiment provided evidence that adjusting the wheel loading on ground doesn't capture the mobility performance in partial gravity as seen in the comparison of the two data-sets in Figure 1.14).

Such a result provides further motivation to study rover-soil interactions in reduced gravity, in order to develop a fuller understanding of why this is the case. Reduced-gravity flights studying excavation [10] and bearing capacity [16] have similarly produced non-trivial, and non-intuitive results that enhance our understanding of terramechanics in reduced gravity. Studying the impact of gravity variation on the relation between shear stress and shear strength of a particular soil is of a great importance in improving the terramechanics models.

Figure 1.13: Gravity offloaded excavation experiments at NASA Glenn Research Centers (GRC) Simulated Lunar OPErations (SLOPE) lab. A cable pulls up on the robot, tensioned by weights acting through a lever arm. The offload assembly hangs from a hoist that is pulled along a rail by a separate winch-driven cable, as marked [55].

There has been little research studying the effect of partial gravity on soil simulant characteristics, thus, many of the soil parameters and soil behaviours in low gravity conditions are not clearly defined. Reiss investigated the effect of partial gravity on two lunar regolith simulants (JSC-1A and NU-LHT-2M) finding a linear relationship between flow rate and gravity condition [48]. On the microgravity of the space shuttle, triaxial compression tests were conducted [58] to investigate the correlation between stress and strain of granular material at low effective confining stresses. There hasn't been enough experimental data in reduced gravity to accurately conclude and outline the soil behaviour and properties under these conditions. Murdoch et al. studied the effect of gravity variation on granular flow of Taylor-Couette shear cell [39]. The shear cell has been used to investigate the effect of shear stresses on granular materials. They concluded that radial flow is affected by gravity variations where gravity influences the frictional interactions and plastic deformation of granular material.

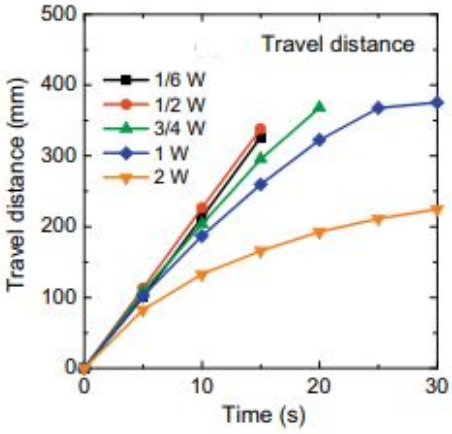

(a) Travel vs Time in Earth gravity

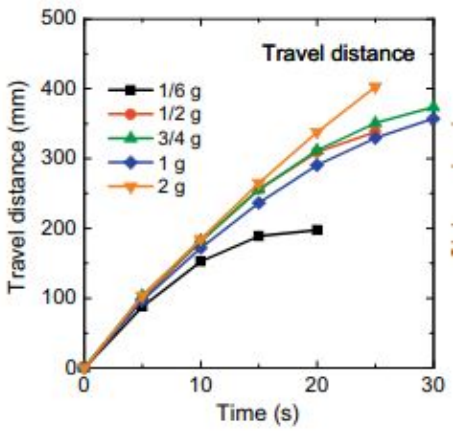

(b) Travel vs Time in partial gravity

Figure 1.14: Wheel's normal loading is adjusted on ground to correspond to the gravity variation [34] (a) A lighter wheel can travel a longer distance in Earth gravity (b) A lighter wheel travels shorter in partial gravity.

Costes et al. evaluated soil strength and packing using cone penetrameter of granular soil simulants under partial gravity conditions. It is indicated that the average resistance to penetration decreases with reduction in gravity [19].

Due to the importance of soil conditions, as described in Section 1.1.2, at least some degree of soil preparation has been included in prior reduced gravity terramechanics experiments. Kobayashi et al. loosened and leveled the soil using a rake and then compacted the soil using a rigid plate and wooden mallet; this was done before each test (i.e. before each parabola) aboard the aircraft [34]. Boles et al. loosened soil with a concrete vibrator and leveled and compacted it with a plate and hand-held motorized tamper; it is implied that this was only completed once prior to the flight itself [10] (i.e. not repeated for each parabola). Bui et al. mention that their soil was initially compacted with a vibrator [16]; no resetting of soil conditions between tests was reported. Thus, despite recognition of the importance of soil preparation, it is not always consistently applied prior to each test. This is simply due to the constraints imposed by reduced gravity flights themselves. When it has been applied prior to each

test, as by Kobayashi et al., it has been done manually which is both time consuming and exposes the aircraft cabin to dust. Furthermore, the repeatability of in-flight soil preparation and sensitivity of soil preparation to the flight maneuvers themselves have never been studied.

1.2 Terramechanics Models

Classical wheel-terrain interaction models used in the literature are unable to sufficiently predict the effects of reduced gravity on rover performance. This section describes how they rely on assumptions that do not apply to planetary exploration. It then presents a brief summary of these existing literature on modeling rover wheels in reduced gravity flights, and finally discusses modern approaches to wheel-soil modeling.

1.2.1 Attempts at Reconciling Reduced-g Experiments with Theory

The founding modeling paradigm of terramechanics relies on quasi-static pressure sinkage relationships to estimate compaction resistance [7] and/or empirical parameters, e.g. to estimate the location of maximum pressure beneath a wheel [72]. For rigid wheels on dry granular soil - a typical case for planetary rovers - the quasi-static assumption is contradicted by the data; Wong observed flowing granular soil, and pressure distributions more complex than predicted by quasi-static compaction [70].

Empirical parameters in terramechanics models can pose difficulties when extrapolating to new conditions, such as extraterrestrial regolith and gravity. For example, to account for results of wheel traction experiments in reduced-g flights by Kobayashi [34] within the pressure-sinkage paradigm, a pressure-sinkage coefficient proportional to g has been hypothesized by Wong [16]. However, pressure-sinkage coefficients can

be directly extracted from data of yet another set of reduced-g flight experiments by Bui, and are in fact constant across measurements at 1 g, 1/2 g, or 1/6 g [16] (see Figure 1.15).

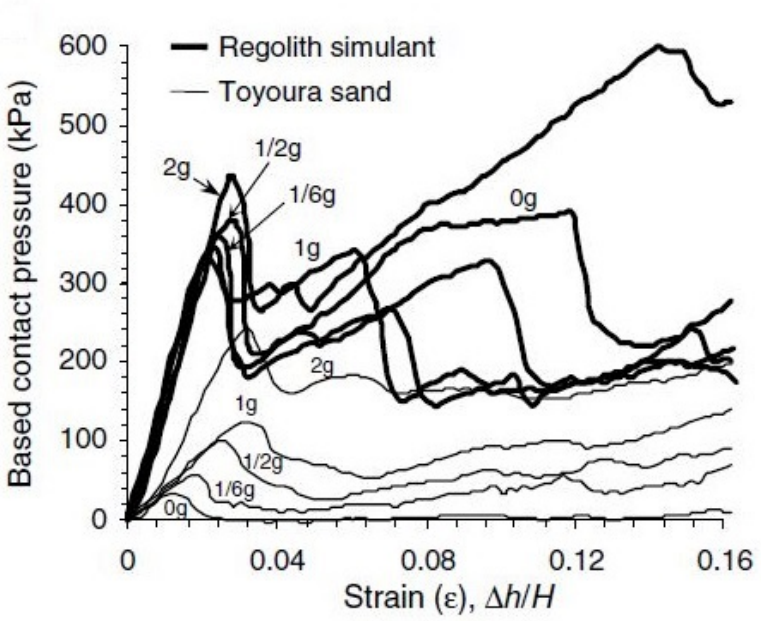

Figure 1.15: Effect of gravity on the applied force beneath the base of footing in experiments: The slope of the pressure vs sinkage (i.e strain) relation is constant between 0 g to 1 g for both soils tested [16].

This inability to reconcile classical terramechanics theory with all available experimental data suggests a need to rethink model assumptions and develop new models for planetary rover-soil interactions. Several researchers today highlight the insufficient predictive power of classical terramechanics models for planetary rovers [37], [21], [31], [50]. New efforts in understanding and modeling the effects of gravity on rover-soil interactions will require an underpinning from an expanded set of experimental data.

1.2.2 Modern Approaches to Wheel-soil Modeling

A prominent direction of current terrain interaction research is the discrete element method (DEM), which simulates contact mechanics for millions of individual granular particles. This state-of-the-art approach demonstrates promise in modeling planetary rover interactions, but is so computationally intensive as to be infeasible to implement on a rover for online control in the foreseeable future [33].

Kovecses has developed various models and techniques for analyzing performance and simulating wheels on soft, granular terrain. A novel technique was developed using an elasto-plasticity theory-based description of the wheel-soil interaction [5]. This provides a computationally efficient representation that is fully compatible with dynamic models of rovers. It overcomes several shortcomings of the classical terramechanics-based formulations. The theory considers elastic-plastic behaviour of the soil. The diagram shown in Figure 1.16 depicts this model with the elastic (stiffness c_f and Newtonian viscosity η) and plastic (compression μ_v and yielding constant μ_p) parts which, in addition to Bekker's and Wong's approach [7], [71] takes into account the sinkage velocity $\dot{z}$. The corresponding equations for the pressure-sinkage relationship of this model, equation (1.12), is comparable with Bekker's model in equation (1.2).

$$p_{dyn} = \left[(\frac{\mu_v}{c_f + \mu_v})^2 \eta \dot{z} + \frac{c_f \mu_p}{c_f + \mu_v} \right] \left[1 - e^{\frac{c_f + \mu_p}{\eta v} z} \right] + \frac{c_f \mu_v}{c_f + \mu_v} z \tag{1.12}$$

Visualization of wheel-soil interactions provides means to validate modern modeling approaches and/or identify areas for further development.

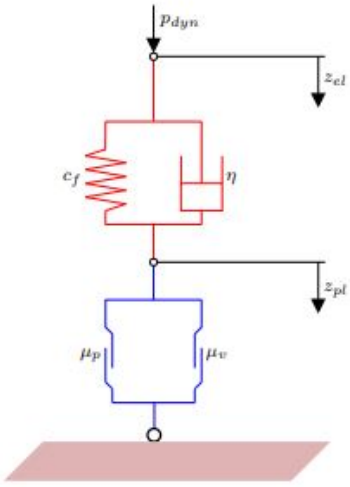

Figure 1.16: Soil model representing the elastic (red) and plastic (blue) behaviour of the soil [11].

1.3 Contributions and Scope

This thesis presents the development and in-flight evaluation of an automated testing system for planetary rover terramechanics experimentation aboard reduced-gravity flights. The three key contributions of this study are: (1) Development of a novel rapid automated soil preparation system (2) Collection of enhanced terramechanics datasets capturing important effects of reduced gravity on DP vs slip (3) A novel visualization dataset exhibiting behaviour of the wheel-terrain interaction in partial gravity and Earth gravity.

These contributions represent advances relative to the state-of-the-art in the single wheel terramechanics testing literature, especially relative to the state-of-the-art in reduced gravity wheel-soil testing. The experiments can serve as the basis for new terramechanics models, but the development of such models is considered outside the scope of this thesis and is left for future work.

1.4 Document Organization

The collection of enhanced terramechanics datasets during parabolic flights requires specialized unique experimental apparatus. An advanced automated robotic gantry system is designed and manufactured to satisfy on-flight constraints, regulations, and structural safety requirements imposed by high accelerations. The structural modeling and analysis of the experimental apparatus is one of the most significant activities in preparation for the parabolic flight campaign. An overview of the design, structural analysis and verification of the flight system is described in Appendix A.

The rapid automated soil preparation subsystem provides the capability to perform consistently repeatable soil preparation, which is a critical element of reduced-gravity flights. The design and verification of the subsystem are described in detail in Chapter 2.

The key parameters, system setup, and techniques used to collect and analyze the enhanced terramechanics and visualization dataset are elaborated in Chapter 3. This chapter explains the uniqueness of the system setup and the importance of the parameters being studied in this campaign. The experimental results and analysis of the datasets performed in the laboratory and partial gravity are presented in Chapter 4. ExoMars wheel performance-data collected in Martian gravity targets potentially high-value data points for the actual Mars mission. The visualization analysis provides enhanced context to aid in the understanding of how the reduced gravity affects the rover wheel performance providing guidelines on how soil flows in the reduced-gravity conditions differently than on Earth. Chapter 5 summarizes the outcomes and results of this research. The contribution of this dissertation in addition to directions for future work are also summarized in Chapter 5.

Chapter 2

Automated robotic gantry & Rapid automated soil preparation subsystem

This chapter presents the design of the experimental apparatus in general, and automated soil preparation in particular, for reduced gravity wheel-soil interaction experiments.

2.1 Automated Test Apparatus

The primary purpose of the experimental apparatus is to study wheel performance. In particular, the experiments focus on a prototype wheel for the European Space Agency (ESA) ExoMars mission. The ExoMars wheel has a unique flexible wheel design consisting of high-strength stainless steel sheet metal with two sets of operational springs (titanium leaf-shaped springs) for impact energy absorption. The ExoMars compliant wheel prototype is 285 mm in diameter, 120.8 mm in width with 12 grousers (Figure 2.1). The wheel has been tested under challenging quasi-static impact loads, continuous stress for life expectancy and impact due to radial loads. However, due to the high cost and unavailability in the public domain, it has not been otherwise widely evaluated and characterized. Predicting the performance of the wheel heavily relies on empirical data, so there is great value in conducting experiments, especially

in reduced gravity as will be encountered on Mars. Therefore a specialized robotic test apparatus is developed to meet the constraints imposed by reduced-g parabolic flights.

The rover wheel is driven (via synchronized control of a horizontal linear actuator and a wheel motor) in an instrumented sandbox that measures 6-axis force/torque along with wheel sinkage. The wheel is pressed up against a transparent window in the sandbox, and a high-speed camera observes wheel-soil interactions through this window (via a mirror reflection for the sake of system compactness). These experiments are referred to as the 'Terramechanics' experiments. The main experiment subsystem is shown in Figure 2.2, with key elements identified that are required to carry out the functions that were described above. Detail of the terramechanics experiments will be further discussed in Chapter 3.

Three key states of the system, including the configuration for soil preparation and terramechanics experiments, are illustrated in Figure 2.3. Additionally, a photograph of the complete system enclosed in its vinyl inner enclosure is shown in Figure 2.4. The layout of the aircraft cabin and placement of the installed robotic gantry is shown in Figure 2.5. For details on structural design and mounting to the aircraft refer to Appendix A.

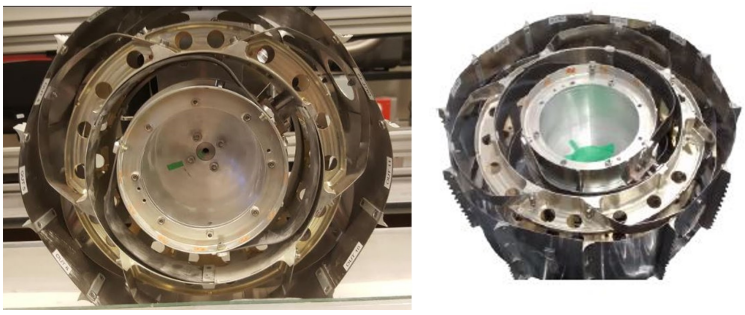

Figure 2.1: A prototype of the innovative ExoMars flexible wheel

In order to ensure repeatable soil conditions, soil preparation procedures including loosening and then compacting and leveling the soil are conducted between each wheel

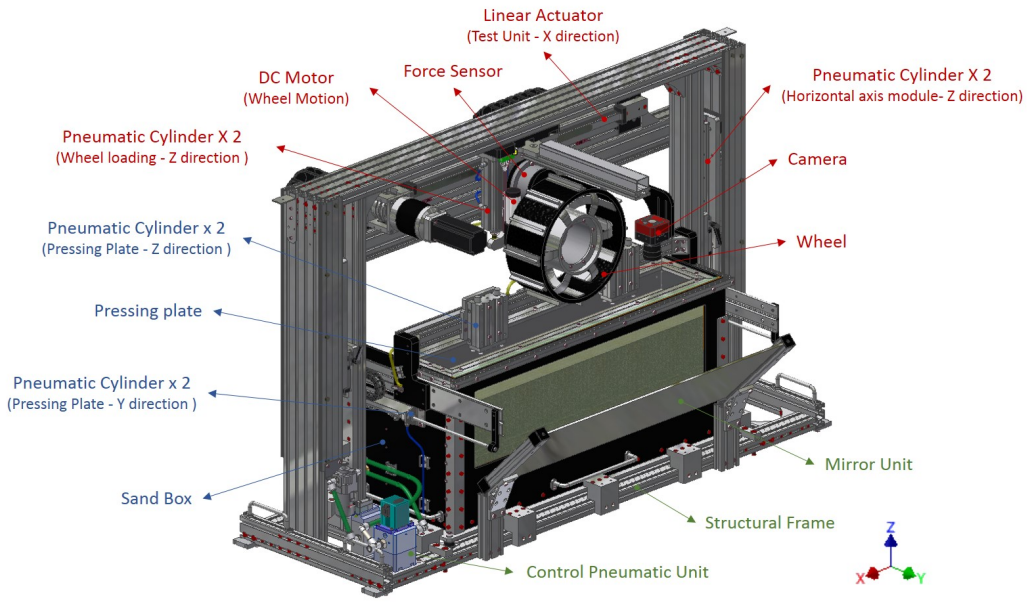

Figure 2.2: Design of automated test apparatus. The apparatus as shown is configured for terramechanics experiments, with key functional elements identified.

experiment. To achieve this despite tight in-flight time constraints, a rapid automated procedure using pneumatics has been developed. The design, and verification of this sub-system is the focus of Sections 2.3 through 2.4. For a subset of the planned experiments, referred to as the 'soil properties' experiments, a cone penetrometer is used to measure soil properties to validate the soil preparation technique. An image of the experimental setup for 'soil properties' testing with cone penetrometer is shown in Figure 2.6.

Pneumatics are used in the experiment for linear actuation, sandbox vibration, and blowing for sand loosening. The air is supplied from SCUBA tanks, via NRC's scuba tank mounting unit (that includes a regulator and dump valve). The air fills a 7-gallon tank that acts as a reservoir for occasional rapid (up to 30 CFM, or 4.5 liters/sec) discharge as may be required by the pneumatic vibrator. Regulators and valves control the distribution of the air flow throughout the system. The supply side of the pneumatic system is depicted in Figure 2.7.

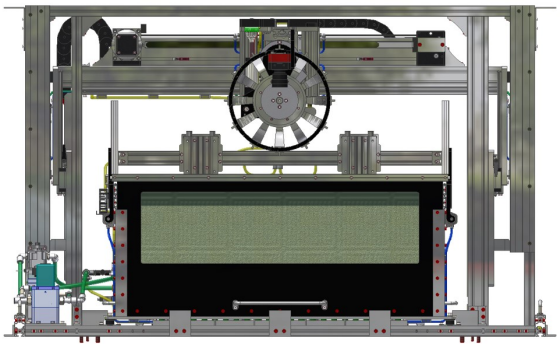

(a) Horizontal axis and wheel unit up, system position for soil preparation

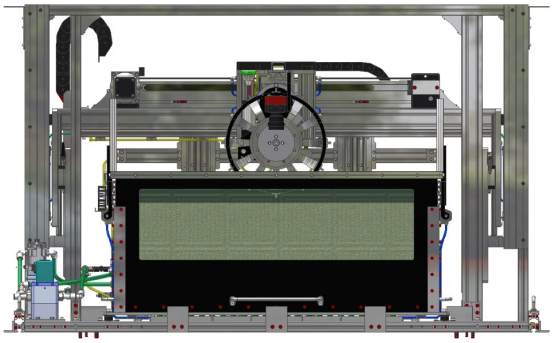

(b) Horizontal axis is down, before wheel-soil interaction, wheel is not touching the soil

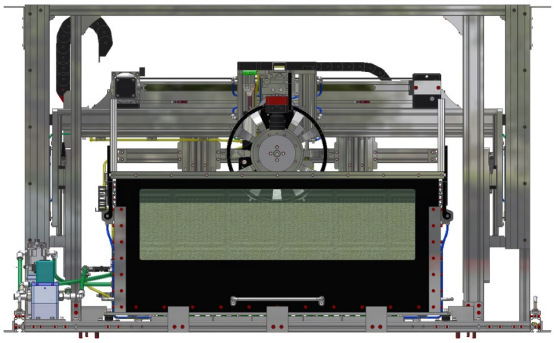

(c) All units down and performing operation

Figure 2.3: Operating states of the automated test apparatus. All actuations of the wheel unit and horizontal axis unit are performed with pneumatic cylinders (Schematics presented in Figure 2.8)

The schematic of the overall pneumatic system is shown in Figure 2.8. The valves and actuators are labeled according to their labeling in the functional diagram in Figure 2.2, for reference.

The experimental apparatus and its connection to the aircraft seat track are required to survive a suite of loading conditions, to avoid posing any additional hazard during a potential emergency landing; these loading conditions include 9 g in the fore direction, 6 g down, and 3 g in the aft, up, and both lateral directions. Analyses of structure and threaded fastener joints are conducted in accordance with NASA [2] and European Space Agency (ESA) [1] standards. Design, verification, and sample of analysis of the flight model is presented in Appendix A.

Figure 2.4: Flight-ready terramechanics experimental apparatus in the laboratory

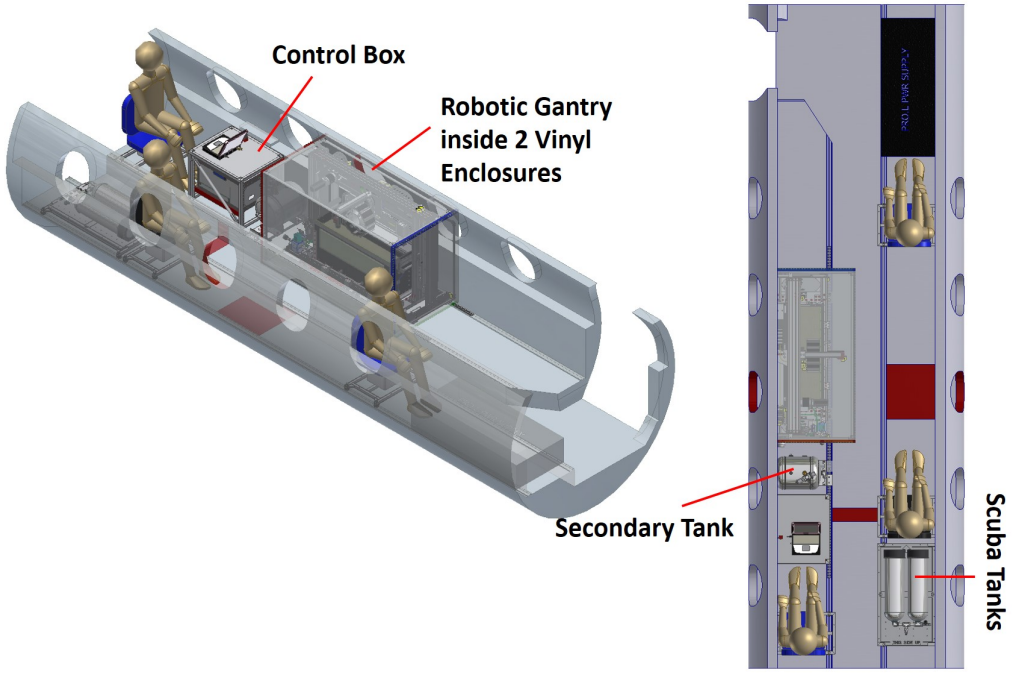

(a) Design of the cabin layout for reduced gravity flights

(b) Inside Falcon 20 cabin

Figure 2.5: Detailed instrument installation inside the cabin (a) Shows the positioning of the tanks with respect to the robotic system (b) shows the automated terramechanics testing system inside a 2-stage vinyl enclosure (center-left) during reduced-gravity flights

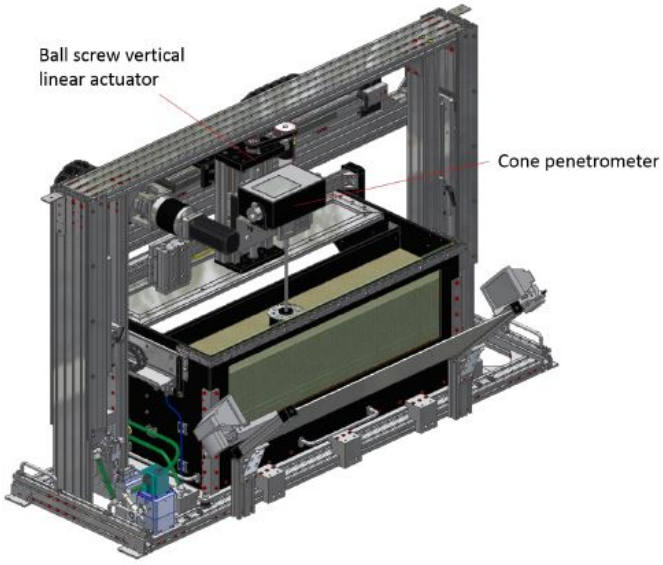

Figure 2.6: Experimental apparatus with cone penetrometer test unit installed.

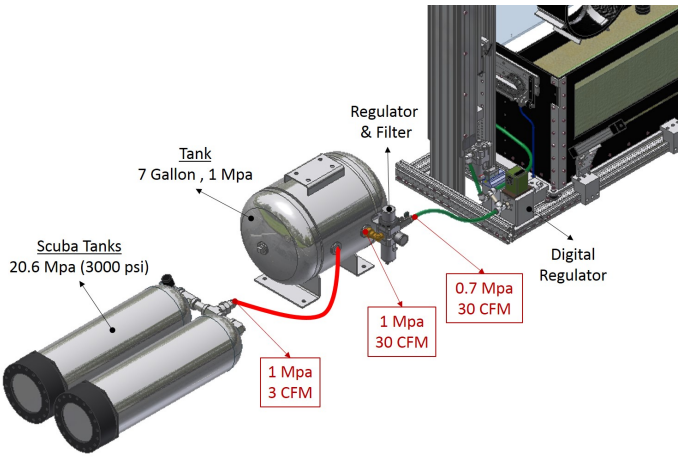

Figure 2.7: Pressure vessel system (air supply)

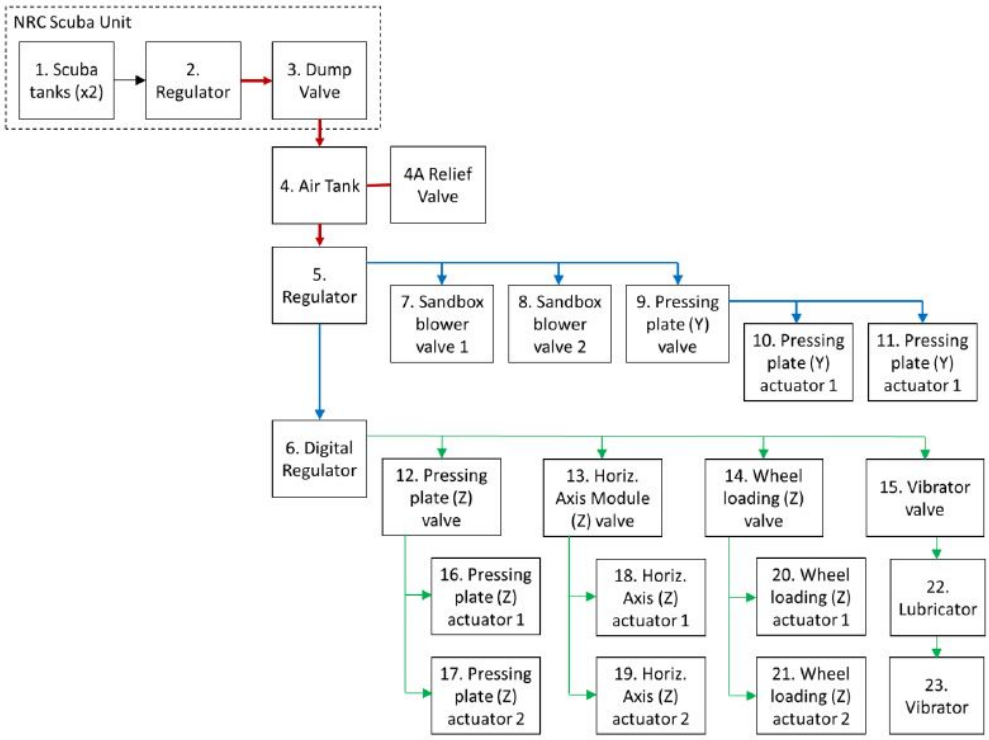

Figure 2.8: Pressure vessel system schematic

2.2 Martian Simulant (ES-2)

ES-2 was selected as the soil for automated reduced-gravity testing. It is relevant to Martian roving missions, being representative of soils found in many areas of Mars (e.g. between sand dunes). It is characterized as a very fine sand, with particle sizes between 30 and 125 microns [13].

In soil mechanics, the macroscopic properties that characterize the shear strength of the soil are cohesion and angle of internal friction. Soil cohesion in dry soils results from electrostatic bonds between the particles. Cohesion is typically measured as the shear strength when the compressive stresses are equal to zero. The angle of friction is a way to measure the ability of soil to withstand shear stress. The friction angle is an angle between the normal force and resultant force at the time of soil failure in response to a shearing stress. The void ratio of the soil is the ratio of the volume of voids (empty spaces between the soil particles) to the volume of soil solids. In terramechanics models, these parameters are used to evaluate the vehicle traction performance by providing estimation on the ability of a terrain to support the traverse of a given vehicle. The relevant ES-2 soil parameters [69] are presented in Table 2.1.

TABLE 2.1: ES-2 SOIL PARAMETERS

Parameter	Value
Internal friction angle	37 ± 5 (^{o})
Cohesion	0.75 ± -0.75 (KPa)
Void ratio	0.78-0.88
Dry bulk density	1450 ± 25 (kg/m^3)

Brunskill et. al characterized the Martian simulant ES-2, where the results for the ES-2 direct shear tests show that the instantaneous and effective friction angles are similar in all densities. This would suggest the material is expected to have low cohesion [14]. It is known in soil mechanics that soil characteristics such as internal friction angle and cohesion depend on the density of the soil. Thus, ESA recommends

a density of 1450±25 kg/m^3 that emulates a strength which is representative of the soil strength corresponding most to common occurrence on Mars [69].

It is important to note that low-density regolith is the most challenging to traverse for rovers. The challenge of the NASA rover Spirit trapped on Mars was compounded by the combination of loose regolith, inefficient estimation and inadequate prediction of the models. Accordingly, ES-2 simulant is prepared to satisfy the ESA's recommended density, with an interest in targeting the lower end of the density range.

2.3 Rapid Automated Soil Preparation Subsystem

This section describes the design, development, and operation of a novel rover-soil testing system that includes rapid automated soil preparation. Providing a consistent and reliable testbed for wheel-soil interaction experimentation in reduced gravity flights requires the development of automated soil preparation techniques (to achieve repeatable soil parameters). Differences in density/compaction of soil result in soil with different soil characteristics (soil parameters such as shear stress, effective friction angle, cohesion, etc.) and produce variation and inconsistency in the experiment's terramechanics results. Constraints imposed by testing aboard an aircraft performing parabolic flights make soil preparation challenging. In previous research, such preparation was conducted manually [34]. Additional requirements and constraints reinforce the necessity of an automated system. Dust mitigation and tight time constraints are two of these other factors that motivate automated rapid soil preparation in an enclosed volume.

Soil preparation for terramechanics experimentation consists of loosening, compacting, and leveling soil to achieve repeatable soil parameters.

During soil preparation, the wheel unit retracts from the soil using two vertical pneumatic cylinders, also the horizontal axis unit is lifted by another set of vertical pneumatic cylinders (see Figure 2.3). Once both units are up and the top of the sandbox is cleared, the lid (i.e. pressing plate) moves forward and fits within the walls of the sandbox. Forward motion of the plate is done by two slider units guided by two horizontal pneumatic cylinders. Loosening involves shooting jets of compressed air through the soil via flexible valves at the base of the bin . Compaction and leveling are achieved simultaneously by vibrating the sandbox and lowering the pressing plate to a desired depth. Air jets and vibration are rapid techniques for loosening and compacting soil, respectively.

The quality of the soil preparation achieved is validated by measuring the resulting soil properties using a high quality cone-potentiometer (Rimik CP40ii). Consistency of soil preparation between different areas of the test-bed, and between subsequent runs of the equipment, is discussed in Section 2.4.

2.3.1 Requirements Imposed by Reduced-gravity Flights

The elements of a reduced-gravity flight trajectory are illustrated in Figure 2.9. The key elements are the preparation phase and the reduced-g parabola. After experiment and instrumentation preparation, the aircraft descends and then executes a 2-g pull up after which it transitions into approximately 20- 25 seconds of reduced-gravity (20 sec. in the case of lunar gravity, and 25 sec. in the case of Martian gravity). Following the parabola, the aircraft pulls out in another 2-g maneuver and then returns to preparation phase altitude. Several parabolas can be executed successively in a line if the preparation phase is short or not required. The 2 key functions of a reduced-gravity terramechanics testing system correspond to the 2 key elements of the reduced-g flight trajectory, test execution and data collection (performed in reduced-g parabola) and soil preparation (performed in preparation phases between reduced-g parabolas). The primary motivation for soil preparation being rapid is the constraint on the available flight time and required number of parabolas for the study.

The ES-2 soil simulant imposes another constraint. The fine particles of ES-2 pose a health hazard and its circulation in the airplane's air system has to be prevented. Dust generation cannot entirely be avoided during terramechanics testing and soil preparation, and exhausting in flight is not feasible. Thus, the experimental apparatus must be enclosed. The enclosure adds additional impetus to automating the entire testing system.

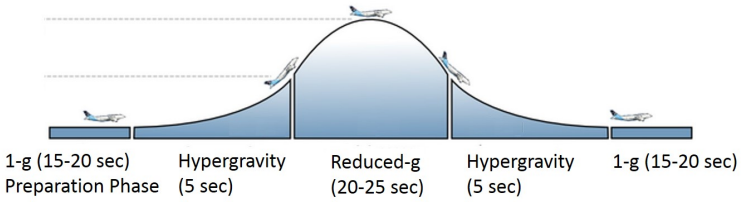

Figure 2.9: Parabolic shaped trajectory achieving reduced gravity [17]

2.3.2 Design Features of Rapid Automated Soil Preparation System

A key contribution of this work is the development of a rapid automated soil preparation system. This system must achieve soil loosening, leveling, and compaction, all within a short time while respecting the other high-level requirements and constraints discussed in Section 2.3.1. The solution developed for this, which takes less than 15 seconds, involves blowing jets of compressed air (loosening) and vibration (leveling and compaction). The following subsections describe the design and development of each of these aspects in turn.

Loosening with Jets of Compressed air

Jets of compressed air accomplish loosening within an 80 kg mass of ES-2 soil in 150 ms. In addition to loosening the soil rapidly, care is also taken to loosen the soil uniformly so as to aid the subsequent leveling step. Compressed air is distributed to 4 manifolds mounted underneath the sandbox, as shown in Figure 2.10. Each custom manifold has 11 possible outlet ports at a spacing (pitch) of 30 mm. The system is designed to be re-configurable so that any combination of outlet ports can be set up for use, for example in case different soils require different configurations in the future. The 44 available output ports can be seen in the base of the sandbox in Figure 2.11. In its nominally designed configuration, each manifold has 2 open outlets (shown circled in the Figure) through which it emits jets of compressed air.

The 44 holes at the base of the sandbox each hold a flexible one-way valve through which the air can be blown into the sandbox. Each of the 44 manifold outlet ports is sealed with a screw plug. The open outlet ports have holes drilled into the screw plugs, through which the compressed air exits to the valve. Figure 2.12 shows the 11 possible outlet ports of a single manifold, with screw plugs, drilled holes, and flexible valves identified. The number, spacing, and hole diameter of the open outlet ports were the subject of extensive research within the scope of this project.

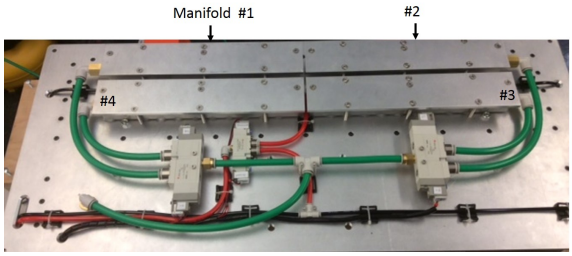

Figure 2.10: Bottom view of sandbox showing the 4 manifolds used for blowing jets of compressed air into the soil.

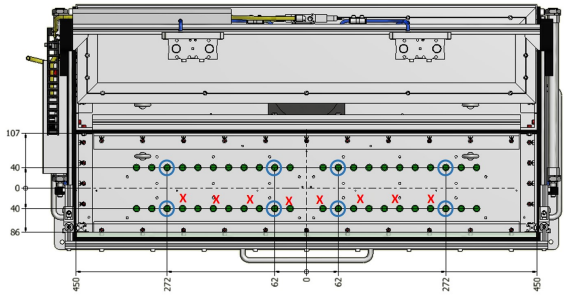

Figure 2.11: Top view looking into the sandbox showing the 44 available outlet ports (green dots) of the manifolds mounted below. The ports circled in blue are the open ports in the nominally designed configuration. Red crosses indicate cone penetrometer measurement locations (see Section 2.4). Dimensions in mm. The sandbox lid is shown in the open position.

Let D represent the inner diameter of the manifold and L represent the spacing between the first and last open outlet port, as shown in Figure 2.12. Also, let $D_{o,i}$ represent the outlet hole diameter of any particular outlet port i. Recall that uniformity of outlet flow is an important goal to aid with subsequent leveling. Uniformity is

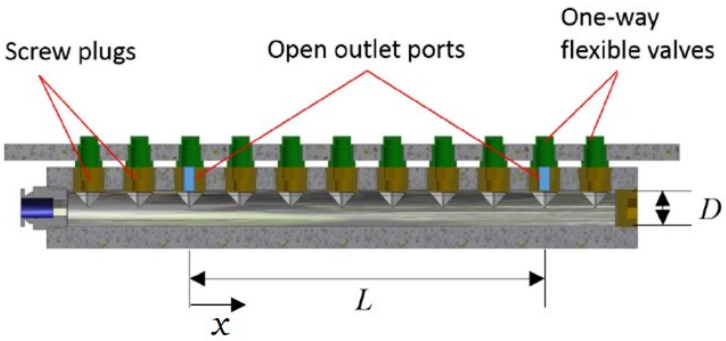

Figure 2.12: Section view of manifold identifying key elements and dimensions

quantified by a lack of pressure differential (i.e. pressure drop) between outlet ports. Theoretical work by Wang et al. [65] identifies thresholds for particular parameters as guidelines for achieving uniform outlet flow from manifolds. Key parameters of interest include M and E, both defined below:

$$M = \sum_i ((D_{o,i})^2/D^2) \tag{2.1}$$

$$E = L/D \tag{2.2}$$

$$X = x/L \tag{2.3}$$

Further, X is a dimensionless position along the manifold.

The development of theoretical models of flow in manifolds [65], is a continuation of Wang's analytical model based on mass and momentum conservation [64]. In an isolated system where no external forces are acting on the system the momentum of a system remains constant; this is known as the conservation of momentum principle. Momentum is a constant multiple of velocity with the same vector direction.

Two key parameters determining the efficiency of the manifold system are flow distribution and pressure drop in the manifold. Wang determines the influence of geometrical structures and parameters in manifold performance to predict pressure drop and flow distribution. The two conservation principles are coupled with velocity and pressure terms to derive equations which reduce to dimensionless parameters describing the flow distribution. v_c is dimensionless volume flow rate and $(p_1 - p_0)/(\zeta/2)(\mathrm{F}/\mathrm{n}F_c)^2$ in Figure 2.13a represents a pressure drop in the manifold.

Figure 2.13a illustrates the sensitivity of the pressure drop to the parameter M; lower M results in lower pressure drop. In this figure X is the dimensionless axial co-ordinate defined by Equation (2.3). Figure 2.13b shows that uniform flow distribution across the manifold is realized when M is smaller. To have a uniform displacement in the soil it is desired to have both flow and pressure drop across the manifold consistent.

Figure 2.14a illustrates the sensitivity of the pressure drop to the parameter E; $E \leq 10$ results in lower and more linear pressure drop. Figure 2.14b shows that uniform flow distribution across the manifold is realized when parameter E is less than 100. To have a uniform displacement in the soil it is key to keep both flow and pressure drop across the manifold as consistent as possible.

Following [65] and the description above, it is easy to conclude that $M < 1$ and $E < 10$ are useful guidelines to demarcate a regime where pressure drop across a manifold is negligible (see Figures 2.13 and 2.14).

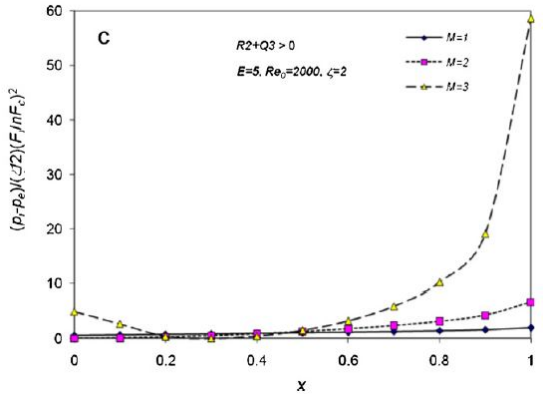

(a) Effects of parameter M on pressure drop

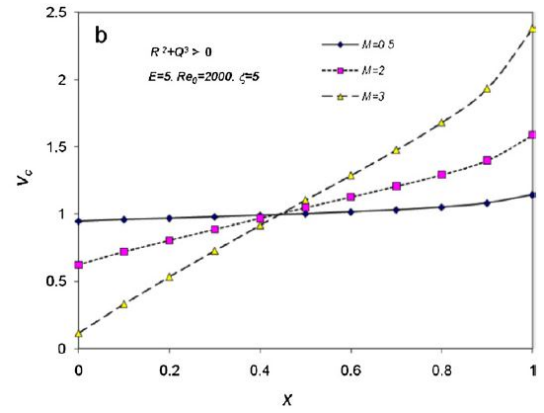

(b) Effects of parameter M on flow rate

Figure 2.13: Effect of parameter M (ratio of summation of open outlet port diameter to manifold inner diameter) on the flow distribution across manifold [65]

The manifolds used in this work have $D = 18$ mm and nominal threaded outlet ports of 20 mm diameter. It is thus immediately clear that having multiple fully open outlet ports would lead to $M > 2$, which is undesirable. Therefore, screw plugs are used in each outlet port, with drilled holes used to achieve smaller outlet port diameters. Each screw plug is installed using a 10 mm hex socket (10 mm refers to the diameter of the hexagon's inscribed circle), so for practical purposes the hole diameter cannot exceed this diameter and still be installed. In fact, observations show that the drilled hole diameter should not exceed approximately 90% of the hex

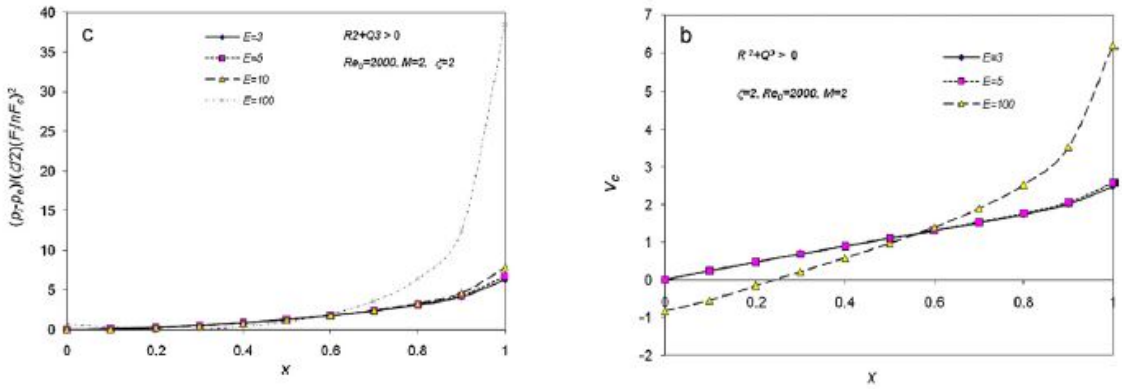

(a) Effects of parameter E on pressure drop (b) Effects of parameter E on flow rate

Figure 2.14: Effect of E (ratio of manifold length to inner diameter) on the flow distribution across manifold [65]

sockets inscribed diameter or else significant pressure loss is incurred. This can likely be explained by turbulence that develops in hexagonal orifices [66].

The theoretical and practical guidelines identified above served as a starting point for empirical trials used to further refine the system design parameters. Tests were performed first in a box of just under half length equipped with a single manifold

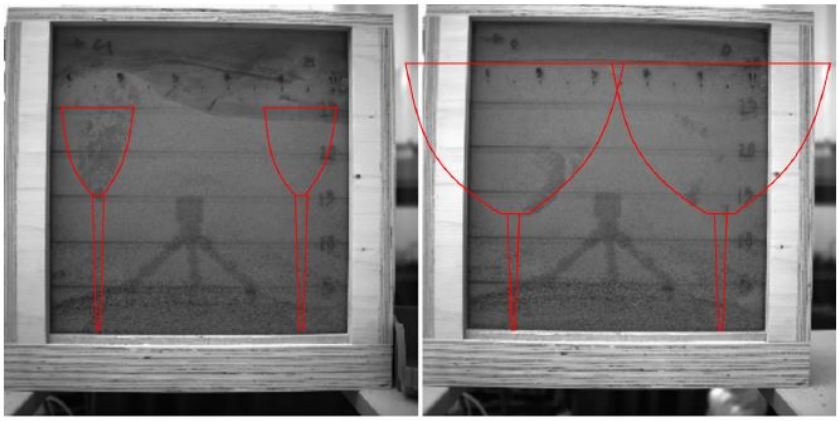

Figure 2.15: Increasing soil depth from 25 cm (left) to 31 cm (right) substantially increases the proportion of soil in the top half of the soil volume that is successfully displaced by blowing. The image shows screenshots from highspeed video of preliminary blowing tests, with red features illustrating areas of motion observed from watching the full video.

and a plexiglass side-wall, and later finalized in the full sandbox. An interesting observation worth noting from these tests is that additional soil depth broadens the region of soil loosened at the top of the soil volume, provided adequate inlet pressure is supplied (0.65 MPa in our system). Soil displacement in between open outlet ports improves with increased soil depth. Figure 2.15 compares tests with 25 cm soil depth to tests with 31 cm soil depth. For the 25 cm test, the regions of soil at the center did not move, whereas increasing the height of the sand resulted in a more uniform displacement across the whole surface. This could perhaps be due to the pressure exerted from the weight of the extra sand causing the airflow to diverge and cover the mid-section. The analyses and empirical tests described above resulted in the outlet port selections highlighted in Figure 2.11. For each manifold, outlet ports 3 and 10 (counted from the inlet port side) are open, with hole diameters of 9 mm and 7 mm respectively. This corresponds to $M = 0.4$ and $E = 11.7$. Empirical observation of using 9 mm diameter for both open ports indicated higher flow at the second open port. To compensate for this effect, the diameter of this second port was reduced to 7mm.

The sandbox lid can be opened and closed (in the negative and positive Y directions, respectively) and also actuated in the Z direction into and out of the sandbox. During loosening, the lid is closed and then moved down (-Z) by 5.5 cm into the sandbox until it is approximately 1 cm above the nominal soil height. Flow into the two manifolds at the front of the sandbox (i.e. closer to the glass wall, more positive Y; Manifolds 1 and 2) is opened first for 50 ms. After 50 ms of settling time, flow into the rear two manifolds (Manifolds 3 and 4) is opened for 50 ms. The vibrator, described in more detail in the next subsection, is on during all of these 150 ms to help redistribute the soil evenly as it settles. It is kept on during a subsequent 1500 ms of settling/compaction time as well.

Leveling and Compaction with Vibrator

Leveling and compaction is achieved with a Martin NTS 50/04 non-impacting pneumatic vibrator, mounted on the base of the sandbox assembly directly behind the sandbox, as shown in Figure 2.16.

During the initial 1650 ms of soil preparation, described in the prior subsection, the vibrator is actuated at 24 Hz, resulting in approximately 1.2 kN of linear force in the Z direction. The vibrator is turned off and the soil rests for 5000 ms, followed by another 24 Hz vibration for 3000 ms. After another 3000 ms rest, if a higher compaction is desired the vibrator can be actuated for 2000 ms at a higher energy: 32 Hz, resulting in approximately 1.5 kN linear force. A summary of the full soil preparation procedure is presented in Table 2.2. Snapshots of this sequence are shown in Figure 2.17, where the sandbox is disturbed after on experiment and the soil preparation procedure levels and prepares the soil for the next experiment. Throughout the vibratory compaction steps of the above sequence, the sandbox lid is kept 6.5 cm above the soil surface. However, if required for other soil types and/or desired soil properties, the lid is capable of applying additional downward pressure on the soil in the Z direction during the compaction phase.

To enable displacement of the sandbox assembly during vibration, the assembly is mounted to the frame via 4 Chloroprene rubber damper mounts, as indicated in Figure 2.16. Because the rubber mounts would not withstand the required structural load cases (described in Appendix A.3.5), aluminum catcher blocks are mounted rigidly to the frame with 2 to 3 mm of clearance to the sandbox assembly base. There are two blocks each on the fore and aft oriented ends of the assembly and three on both lateral sides. The motion during vibration does not cause any collisions between the base and catchers, but the sandbox assembly base is fully caged by the frame and catchers even if the mounts fail.

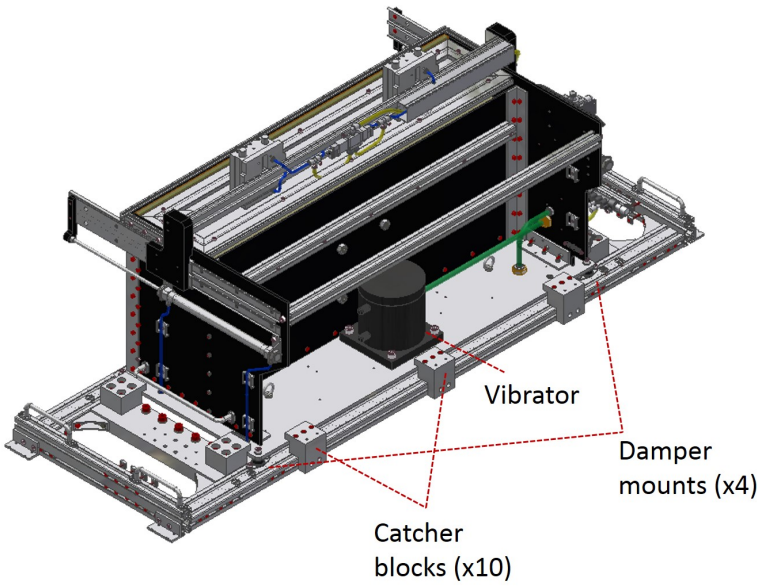

Figure 2.16: Rear isometric view of the sandbox assembly, showing the vibrator, as well as the mounts and catchers designed to keep the sandox assembly in place. The sandbox lid is shown in the closed position

To enable use of pneumatics aboard the aircraft, compressed air is supplied to the system from a pair of SCUBA tanks. However, as the flow from the tanks (1.4 litres/sec) is insufficient to drive the vibrator at the required energy (4.5 litres/sec required), a secondary tank is also used which has the requisite outflow rate and is then recharged over time from the SCUBA tanks (SCUBA tanks and secondary reservoir are marked in Figures 2.7 and 2.5a).

		Step	Duration (msec)	Flow through Manifolds	Vibration Frequency (Hz)	Plate
Nominal	Compacted	1	50	1 & 2	24	Down
		2	50	n/a	24	Down
		3	50	3 & 4	24	Down
		4	1500	n/a	24	Down
		5	5000	n/a	n/a	Down
		6	3000	n/a	24	Moving Up
		7	3000	n/a	n/a	Up
		8	2000	n/a	32	Up

TABLE 2.2: Rapid soil preparation sequence

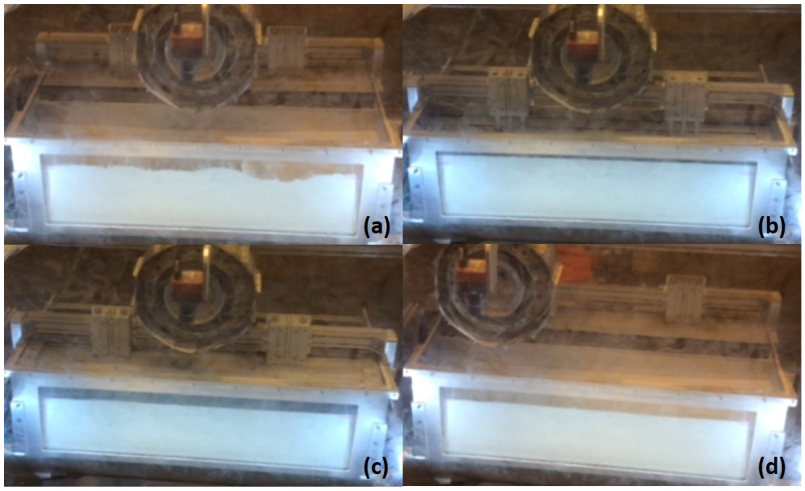

Figure 2.17: Soil condition in the sandbox before soil preparation is shown in (a) and after the preparation is performed is shown in (d). Even when soil is significantly disturbed, preparation consistently returns it to a level condition. Snapshots of steps in Table 2.2 is presented here (b) step 1-3 with the air blowing into the soil (c) step 4-6 vibration with the plate moving up (d) the preparation is completed and the pressing plate is moved back and the wheel is positioned for terramechanics experiment

2.4 Soil Preparation Repeatability

The 15-second procedure detailed in the prior section and summarized in Table 2.2 successfully resets the soil between terramechanics experiments, even when the soil has been significantly disturbed. Figure 2.17 shows soil in the sandbox before and after soil preparation. The photo before preparation shows the condition of soil following a wheel test; there are obvious ruts visible where the wheel sank into the soil. After preparation, the soil is returned to a level state. The height of the soil after preparation is consistently 31 cm$\pm$0.5 cm (i.e. within $\pm$2%) comparing both across the length of the sandbox and between one preparation to the next.

One of the key elements of preparation is the duration and frequency of vibration, thus the effect of variation in vibration on the soil preparation is investigated on the ground to understand how the changes would influence the terramechanics outputs (section 2.4.1). The duration of the high frequency vibration is determined to ensure

no distinguishable change in the soil height, adhering to the recommended density. The repeatability of the soil preparation, both across the sandbox and between tests, is further assessed in greater detail using a cone penetrometer (section 2.4.2) . In addition, repeatability of the terramechanics data (section 2.4.3) and the effect of hypergravity on the preparation (section 2.4.4) are studied to verify the quality of the performance of the subsystem.

2.4.1 Soil Preparation Effects on on-ground Terramechanics data

In this section two sets of terramechanics experiments are compared for two different soil preparations: one with an extra sequence of vibration at higher frequency (referred to as 'compacted') and a less compacted (referred to as 'nominal') preparation. The nominal preparation was achieved as noted in Table 2.2 through steps 1-7, while the compacted preparation includes steps 1-8. Wheel sinkage and drawbar pull (net traction) are collected at various wheel loading and slip values. Details of terramechanics experimental inputs and outputs are discussed later in Chapter 3. For now the key aspects being considered are the effect of soil preparation on the output parameters and their repeatability.

It is important to note that eliminating sequence 8 from the soil preparation sequence (2 sec less vibration) visually has no effect on the soil height level. Even though this step is performed to level the soil providing a uniform top layer, it changes the traction of the rover wheel. Extra vibration may potentially redistribute the density distribution in the soil.

This preliminary testing investigates how much variability remains in the output metrics when repeat tests are conducted with the same soil preparation implemented, as well as how much difference in these outputs may be expected if soil preparation is not the same between tests.

Three datasets are collected for each of the test cases (at each slip value and wheel loading) to estimate the variation in the output parameters (i.e Sinkage and DP), after which standard deviation from the datasets are calculated (see the error bars in Figure 2.18 and Figure 2.19).

Figure 2.18 and Figure 2.19 depict the profiles of average sinkage and Drawbar Pull as a function of the slip rate, respectively, with all the data collected for the same type of soil preparation (compacted). These figures demonstrate that the sinkage and DP data-variability increases at higher slip, and at the higher wheel loading. As seen in these figures, the highest variations occur when slip is 70% or when wheel loading is either 300 N or 335 N.

Next, the differences introduced by different soil preparation are explored. Figure 2.20 shows that at 300 N wheel loading, the difference between the measured sinkage at different soil preparations is consistently about 15%-27%, whereas at 225 N it is not greater than 11% in 9 out of 10 test cases. Thus, sinkage appears to be more sensitive to different soil preparations at higher wheel loading.

Figure 2.21a illustrates that DP trends are similar despite different preparations, at both wheel loadings. DP appears to be more sensitive to different soil preparations at lower wheel loading, at least at lower slip. Even then, the difference between measured DP after different preparation is no more than 15% in 4 out of 5 test cases. Taking into account inherent variability of both sinkage and DP data as well as these metrics' sensitivity to variations in soil preparation, on balance, testing at lower wheel loading produces less uncertainty in the data.

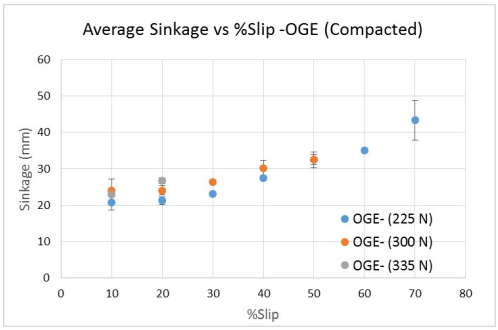

(a) Average sinkage vs slip, OGE

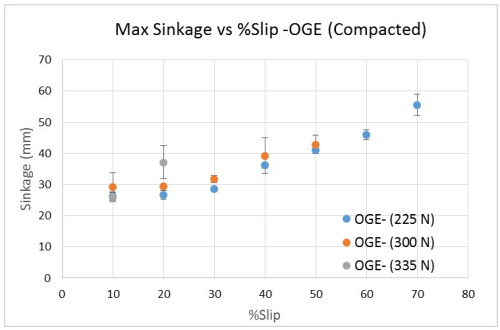

(b) Max sinkage vs slip, OGE

Figure 2.18: OGE compacted sinkage data (a)Average of sinkage at 164 & 225 N wheel loading, slip 10-70% (b)Max of sinkage at 225, 300 & 335 N wheel loading, slip 10-70%

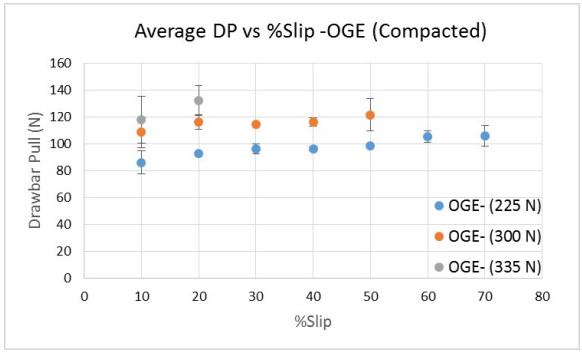

Figure 2.19: DP vs slip, OGE at wheel loading 225, 300 & 335 N

2.4.2 Soil Preparation Repeatability Results on-ground

The repeatability of the soil preparation, both across the sandbox and between tests, is further assessed in greater detail using a cone penetrometer. As will be shown, repeatability in the center section of the sandbox is demonstrated reliably. Cone index (CI) measurements were taken during Apollo as well as Lunakhod missions [29], and have ever since served as an important metric for evaluating extraterrestrial soils and their simulants, for the purposes of terramechanics experiments [41], [20]. CI is the pressure measured on the cone (in kPa or MPa) and is a function of the

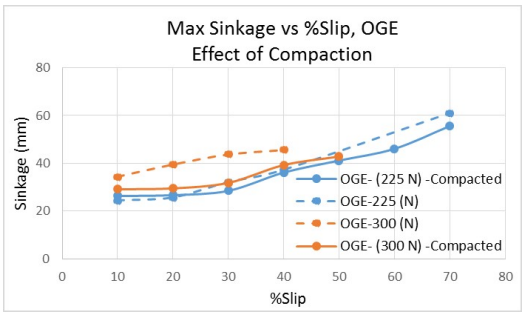

(a) Max sinkage vs %slip, compacted and nominal soil preparation

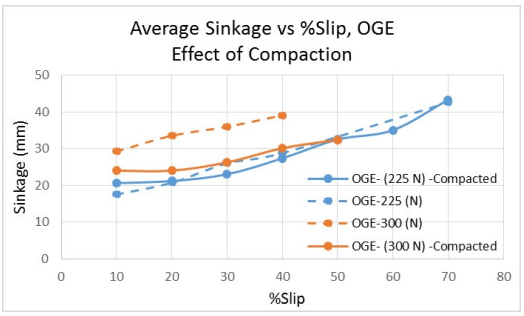

(b) Average sinkage vs %slip, compacted and nominal soil preparation

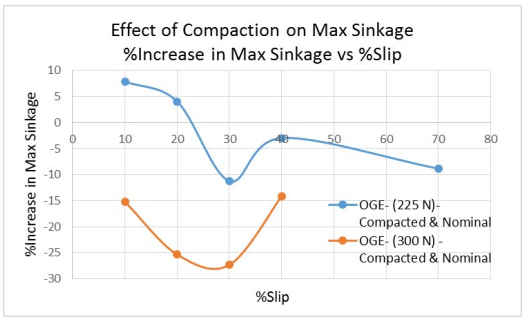

(c) % Change in max sinkage vs % slip

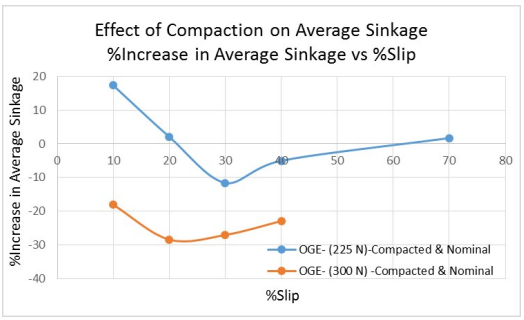

(d) % Change in average sinkage vs % slip

Figure 2.20: Higher compaction decreases the sinkage at higher wheel loading while at lower level of wheel loading the effect is mostly negligible (a) illustrates the effect of compaction on max sinkage (b) illustrates the effect of compaction on average sinkage (c) & (d) illustrate the %change in the sinkage values depending on compaction

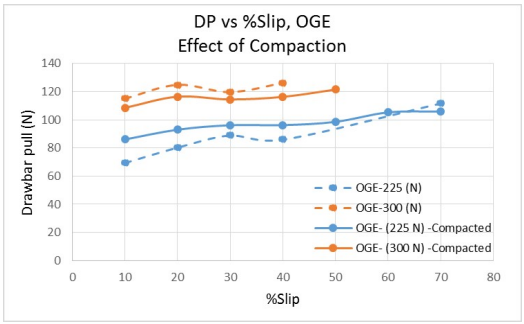

(a) DP vs % slip, compacted and nominal soil preparation

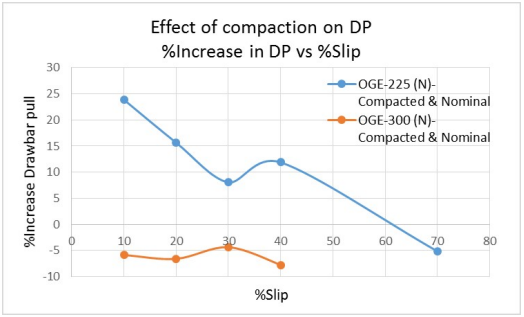

(b) % Increase in DP vs % slip, effect of compaction

Figure 2.21: Increase in compaction affects DP at lower wheel loading more than at the higher wheel loading (a) shows the effect of compaction on DP at different levels of wheel loading (b) illustrates the %increase in DP after compaction

depth of penetration. A useful metric derived from such measurements is the cone index gradient, G (in kPa/mm).

For cone penetrometer testing, the experimental apparatus is equipped with a test unit that is integrated into the system's automation (see Figure 2.6). The unit is displaced horizontally along the sandbox using the same linear actuator used for wheel testing (see Section 2.1) to obtain measurements at various locations. It has vertical actuation for penetration and retraction along the Z-axis. Due to volume constraints on the system, the vertical actuation is limited to 10 cm and achieves a little over 7 cm of penetration depth reliably. The cone penetrometer itself, a Rimik CP40II, interfaces with the control laptop via a serial port, and collects cone index measurements at 1 cm depth intervals.

ES-2 is in fact a very challenging soil to prepare, as the very fine particle sizes enable it to maintain a wide range of possible bulk densities, spanning at least from 1.2 g/cm3 to 1.6 g/cm^3. Furthermore, at its nominal bulk density (60% relative density) of 1.45 g/cm^3, the cone index gradient, G, is no greater than approximately 2 kPa/mm. This is at the very low end of G for typical soils (see, for example [41] and [44]), which means that any errors in cone index measurements cause relatively larger percent errors (in other words, CI readings in ES-2 unfortunately have a low signal-to-noise ratio). The upside of testing with a very challenging soil first is that success can be interpreted as a vote of confidence in the likely generalizability of the technique.

To measure consistency across the sandbox, 8 cone penetrometer readings are taken at the locations indicated in Figure 2.11. The measurements are spaced 70 mm apart horizontally, from -245 mm to +245 mm to span the full extent of the linear actuator's motion. Combined measurements from 5 soil preparations are presented in Figure 2.22. CI measurements are plotted from depths of 2 cm to 7 cm (readings at 1 cm depth were always 0 for all cases as the penetration resistance was still too low

to register a detection). The measurements are divided into two groups: those from the central 4 locations (locations 3-6 when counting from the left; denoted with black circles in Figure 2.22) and those from the 4 outermost locations (1, 2, 7, 8 counting from the left; denoted with red crosses). Nominally each group would contain 120 data points (5 tests x 4 penetrations x 6 depth intervals), however one penetration per group was lost due to sensor faults, resulting in 114 data points per group.

95% confidence bounds for the expected observations are also plotted in Figure 2.22. These are computed from the 5 sets of measurements taken at location 6; this location, at +105 mm, was selected as the reference point because it is closest to the location of in-flight measurements described in Section 2.4.4. Measurements that fall within these confidence bounds indicate good consistency with the reference data. Note that due to the low signal-to-noise for such measurements, even a few data point taken at location 6 fall outside the bounds. However, there is a clear distinction between data from the central group of locations and data from the outermost locations. Of the data from the central group, 81% (92 of 114) fall within the confidence bounds; further, the data that do fall outside the bounds are evenly split above and below the bounds. On the other hand, only 44% (50 of 114) of data from the outer group fall within the confidence bounds and all data that fall outside are below the bounds. This indicates that the CI measurements in the central group are reasonably consistent but unfortunately those in the outer group are routinely lower than those in the central group. The central 280 mm region of the sandbox where the cone penetrometer readings are most consistent, from -140 mm to +140 mm, is the primary region utilized for terramechanics testing. For example, a 20% slip test sees the wheel translate between $\pm$ 160 mm, for 40% slip it is $\pm$ 120 mm, and for 70% slip it is $\pm$ 60 mm. Future work will endeavor to extend the region of most consistent soil preparation further to the edges of the sandbox.

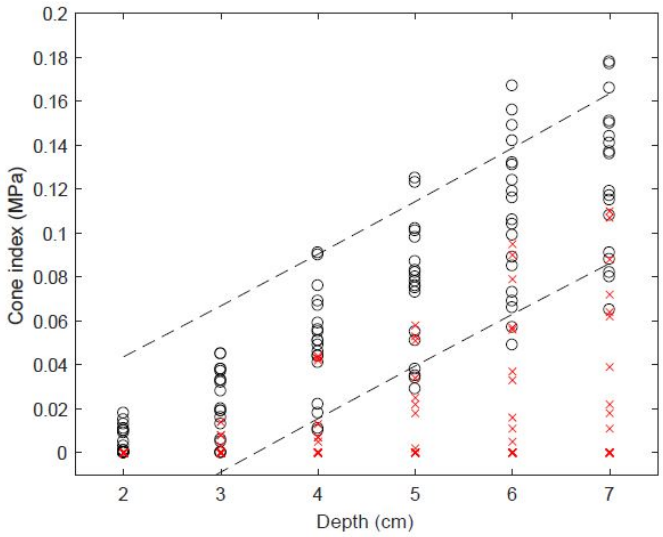

Figure 2.22: Cone penetrometer measurements show better consistency with the reference data for readings in the central 4 locations (black circles) than the outermost 4 locations (red crosses). Dashed lines indicate 95% observational confidence bounds computed from readings at a reference location.

2.4.3 Repeatability of in-flight Terramechanics Data

Examining the repeatability of terramechanics data from wheel-soil interaction experiments in another way of assessing the consistency of the rapid automated soil preparation technique. One particular reduced-gravity terramechanics experiment was conducted in triplicate to examine this repeatability. The experiment that was examined in this way involved the prototype ExoMars rover wheel being driven with 20% slip under 164 N of applied vertical load in Martian gravity (i.e. during the reduced gravity portion of a Martian-g parabola). Drawbar pull and sinkage data from the 3 experiments are shown in Figure 2.23 and Figure 2.24, respectively. Both data streams exhibit strong periodic features associated with the grousers (cleats) on the rim of the wheel. The data were shifted along the time axis to align these periodic effects, as the orientation of the grousers was not consistent between the starts of the 3 tests. There is 20 seconds of full overlap between all 3 tests (out of the 25

seconds of data per test), and the figures demonstrate the low variability and strong repeatability between the triplicate tests.

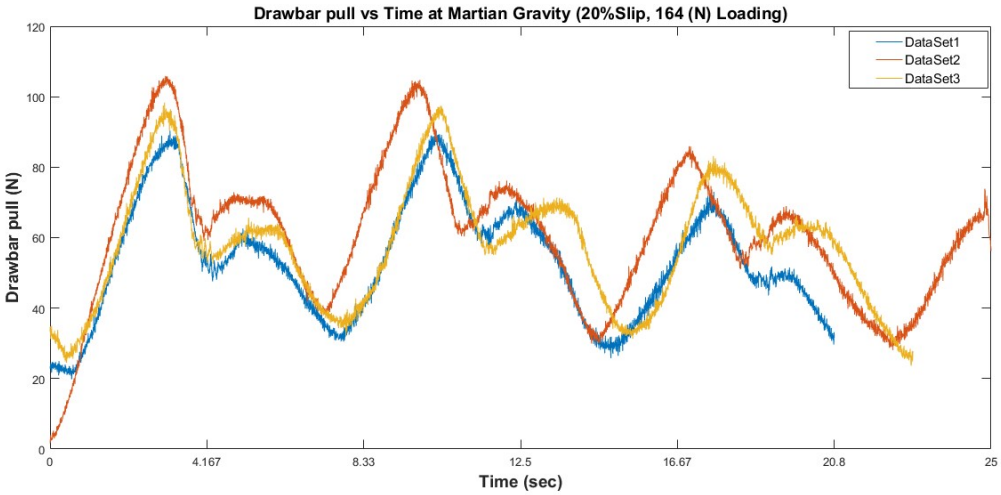

Figure 2.23: Drawbar pull data from 3 repetitions of the same terramechanics test in Martian reduced-gravity parabolas, demonstrating the low variation and strong repeatability of the results

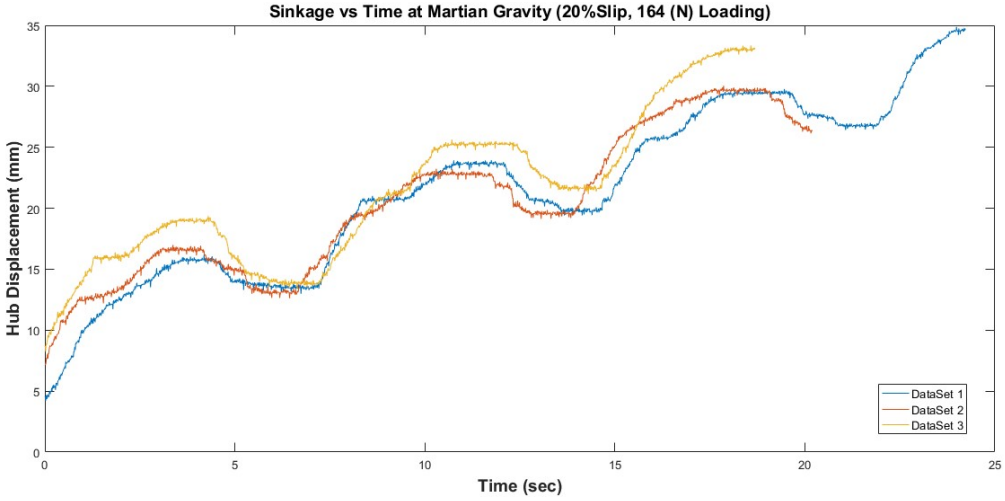

Figure 2.24: Sinkage data from 3 repetitions of the same terramechanics test in Martian reduced-gravity parabolas, demonstrating the low variation and strong repeatability of the results

2.4.4 Effects of Flight Trajectory on in-flight Soil Preparation

Possible effects of flight trajectories on soil preparation were investigated for both the preparation phase as well as the 2g-1/6g-2g parabolas. During the preparation phase, the only noteworthy observation regarding flight trajectory is the necessity to keep gravitational acceleration equal to 1 g and aligned along the apparatus -Z axis. This replicates on-ground conditions for preparations conducted on level ground. To achieve this, the aircraft must be in steady flight with its fuselage horizontal. For the Falcon 20 aircraft, this requires a gradual steady descent. At the airspeeds required to prepare for the parabolas, level (i.e. constant altitude) flight requires the Falcon 20 to be pitched at a non-zero angle of attack. Therefore, to maintain alignment of g along -Z, constant altitude cannot be maintained. Preliminary soil preparations conducted during level flight had a distinct slope of the soil surface relative to the apparatus alignment, necessitating the alteration of trajectory to a gradual steady descent for all subsequent soil preparations.

An open question regarding terramechanics experiments in reduced gravity flights had been whether there is any effect from the 2 g maneuvers at the start and end of the parabolas; the question stems from the fact that loading history can have an effect on soil properties [15]. Experiments conducted for this work show that any effects the parabolas themselves may have on soil preparation are well within the noise of the preparation precision itself. To test this, two sets of soil preparations were conducted aboard the aircraft. The first set was conducted on the ground in the hanger. The soil preparation procedure was executed, followed directly by cone penetrometer measurements; this cycle was completed 7 times. The second dataset was collected in flight for 2 parabolas. Soil preparation was conducted in each pre-parabola preparation phase (at 1 g along -Z, as described above), and cone penetrometer measurements were then taken only after the completion of a full 1/6

g parabola, at the start of the next preparation phase. No soil interactions were conducted during the parabola itself, enabling the subsequent measurement to capture only the effects of the gravity loading profile of the parabola on the soil. Figure 2.25 shows the 7 pre-flight as well as the 2 in-flight post-parabola measurements. As can be seen, the post-parabola soil properties fall well within the 95% observational confidence bounds calculated from the on ground data.

All the above measurements were taken at the same location in the sandbox: +125 mm (to the right of the center of the sandbox). This is within the consistently prepared region used as the primary testing region, as described earlier in this chapter. It is worth noting that the original intent was to collect cone penetrometer data symmetrically at both -125 mm and +125 mm. Unfortunately, the automated system experienced a fault at the first of these two locations after both parabolas, due to slight lag in the pneumatically driven Z axis motion under the influence of varying gravity conditions. These automation faults have been since resolved, but as there was no opportunity to later repeat cone penetrometer experiments, the in-flight cone penetrometer data is limited to the 2 penetrations shown in Figure 2.25.

In summary, rapid automated enclosed soil preparation was achieved in less than 15 sec. The experimental results of cone-penetrometer and teramechanics for both on ground and in-flight campaigns presented evidence of a repeatable and consistent testbed. In addition, the influence of hypergravity on the preparation is not found to be significant.

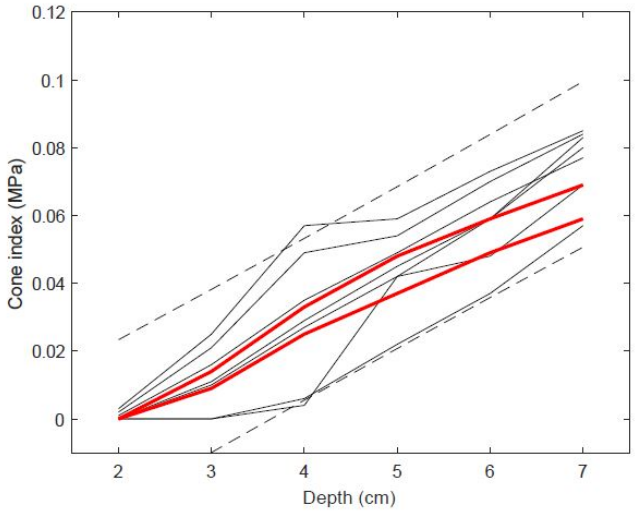

Figure 2.25: Cone penetrometer readings aboard aircraft. Black lines show measurements after successive soil preparations during on ground pre-flight preparations; dashed lines show 95% observational confidence bounds from these data. Red lines show measurements in flight after 2g-1/6g-2g parabolas

Chapter 3

Experimental Setup, Configuration, Parameters

In this Chapter two principle concepts of this research are discussed: terramechanics experiments and soil flow/visualization techniques.

3.1 Terramechanics Experimentation

This section discusses the terramechanics experiment setup, its control, and its limitations. It also presents key constraints imposed by reduced-gravity flight, and the apparatus setup for such flight.

3.1.1 Overview of Experimentation & Setup

As described in Section 2.1, the main experimental apparatus consists of a sandbox beneath a robotic gantry that drives a wheel through the soil in the testbed. The gantry consists of a linear actuator that advances the wheel, a motor that turns the wheel, and pneumatic actuators that apply a downward force on the wheel. By these mechanisms, the wheel's slip and wheel load are controlled. The rover wheel is driven (via synchronized control of a horizontal linear actuator and a wheel motor) on an instrumented assembly that measures 6-axis force/torque along with wheel

sinkage. The wheel is pressed up against a transparent window in the sandbox, and a high-speed camera observes wheel-soil interactions through this window (via a reflection for the sake of system compactness). These experiments are referred to as the Terramechanics experiments. The terramechanic data, telemetry-like data (i.e. motor current and RPM) and high-speed images are collected at Lunar, Martian and Earth gravities. The datasets of partial gravity experiments (PGE) are compared with the on-ground experiments (OGE) to understand the influence of partial gravity on wheel-soil interactions, enhancing the understanding of rover mobility on the terrains of Mars and the Moon.

The robotic gantry is designed to satisfy the constraints imposed by flying the apparatus on board an aircraft. These constraints include limits on apparatus mass and dimensions. Thus the sandbox depth, width and length must be carefully selected. In order to study the terramechanics of the ExoMars rover wheel, the testbed design also considered the requirements imparted by ESA, such as the depth level of the soil, ultimately set at 31 cm. Wheel performance is related to the stress fields in the soil, and is affected by unconformities in the material, such as at the boundaries of the soil with the testbed walls. There has been research done by ESA contracted-researchers to find the testbed's soil depth at which the boundaries don't have a significant effect on the ExoMars rover wheel performance. These studies concluded that soil depth greater than 30 cm does not affect the performance significantly while, on the contrary, soil depth lower than 25cm introduces discrepancies in performance.

The volume of the sandbox is measured to be 0.054 m ^{3}, thus, to achieve the density of 1450$\pm$ 25 kg/m^3, 77.65 kg of ES-2 is used. Density cannot be assumed to stay uniform throughout the soil mass after repeated soil preparation, as soil near the bottom was observed to get relatively denser (evident whenever the soil was removed from the sandbox, e.g. for transport). However, as discussed in Section 2.4.2, the central region of the sandbox (-140 mm to +140 mm) is at least shown to

achieve the same soil properties consistently. These soil properties represent a density slightly lower than the overall average of 1450 kg/m^3. Comparing this value to those characterized by Brunskill for ES-2, it can be noted that the density may be near the lower bound of the recommended range for terramechanics experiment with ES-2, and thus presents a challenging mobility scenario for the rover wheel.

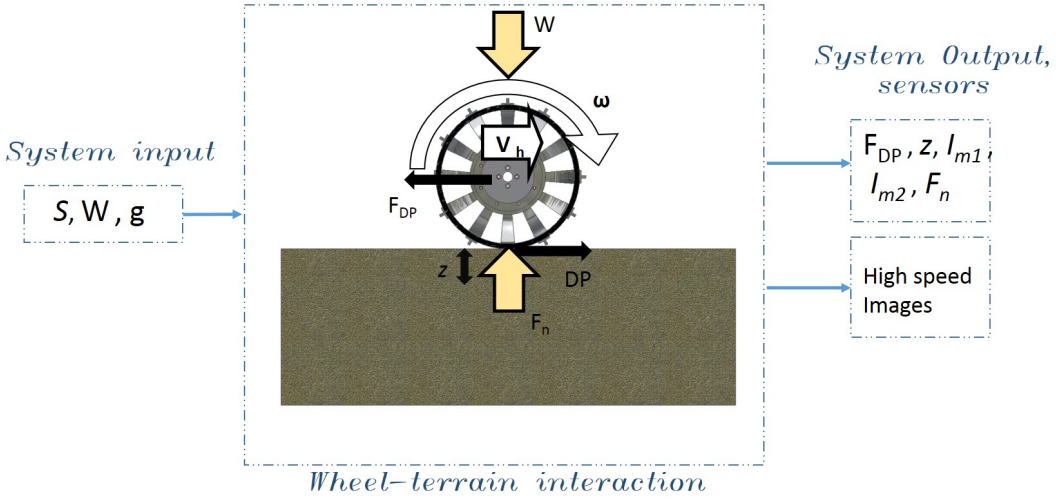

Figure 3.1: Terramechanic model

The varying input parameters into the system are, shown in Figure 3.1, slip (S), wheel loading (W) and the effective gravitational acceleration (g). The outputs of the system includes the measured drawbar pull reaction force (F_{DP}), normal force (F_N), estimated torque for each motor ($I_{mi} * K_{mi}$), and measured vertical hub displacement (z). I_{mi} represents motor current for the motor i, and K_{mi} is the torque constant (e.g. 0.029 Nm/A for the wheel motor).

The camera moves horizontally with the wheel assembly, so during post-processing the horizontal motion is subtracted in order to transform detected motion from the camera frame to a stationary coordinate frame.

From the experimental campaign results, the performance of the wheel can be analyzed providing an understanding of relationships between parameters such as wheel

loading, drawbar pull, driving torque, wheel sinkage, and slip. These parameters and their relationships are described in detail in the section 3.1.3.

One of the important objectives of the OGE is to find interesting cases and boundaries in which the wheel-soil interaction demonstrates notable behaviors. These boundaries of interest are used as a guide to prioritize the test cases for PGE. There are limitations on the system, such as minimum and maximum wheel loading and motor current limitations which impose constraints on the potential test cases. The force/torque sensor data, when operating at 300 N wheel loading and 20% slip, indicates that the normal force on the wheel is close to the maximum rated wheel loading, immediately imposing a maximum allowable load. Further, to ensure precise and consistent controlled slip throughout the wheel traverse, the velocity control mode is used. In case the motor draws more than the rated current, velocity control is automatically transitioned to current control resulting in inaccurate slip control. At 240 N wheel loading and 50% slip the motor current reached its limitation, thus imposing another constraint on the experiments. At 225 N wheel loading, velocity control was successfully maintained at all slip rates, so this was ultimately selected as the maximum wheel loading for the experiments. A lower nominal loading of 164 N was selected as the baseline for testing.

Terramechanics Setup for Flight Campaign

Reduced gravity wheel-soil experiments are divided between Martian and Lunar gravity parabolas (seven lunar-g parabolas, and ten Martian-g parabolas). Testing the ExoMars wheel in Martian gravity directly supports the upcoming ExoMars mission. Experiments at lunar gravity present a clear contrast to 1-g, providing valuable boundary data for developing planetary and reduced-g terramechanics models. In PGE three sets of 20% slip tests are executed for Martian and two sets of 20% slip tests are executed for Lunar-g to analyze repeatability, while all other conditions are

tested once. By keeping the rotational velocity constant and changing the translational velocity during each parabola certain slip values are targeted. The ES-2 soil is prepared according to the 'nominal' preparation shown in Table 2.2 described in Section 2.4. The higher energy vibration in step 8 is avoided to reduce stress on the apparatus and mitigate the risk of mechanical equipment failures in flight.

In reduced gravity, the weight of the wheel unit is lower than on earth. This reduction in weight is compensated using a digital regulator to adjust the pnuematic force applied and thus maintain the same loading to correspond to 1-g experiments. Therefore the only difference between the PGE and OGE would be change in the effective stress in the soil due to the variation in gravity. If any different tendencies are found between OGE and PGE, it can be concluded that the differences are only attributable to the stress conditions in the soil.

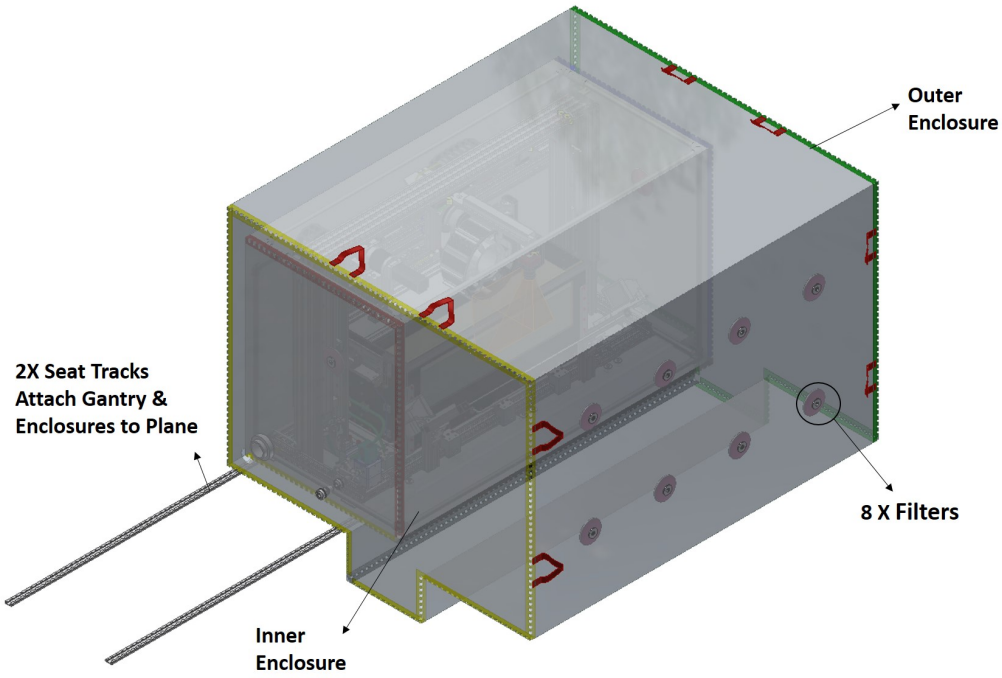

Figure 3.2: Design of the outer enclosure to fit the cabin for dust mitigation

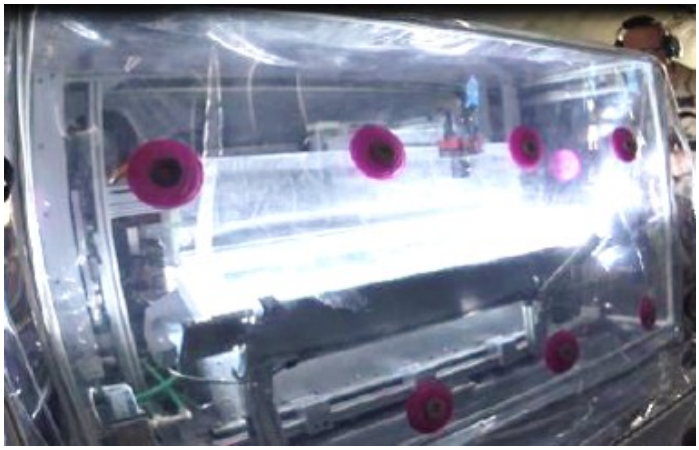

Figure 3.3: Image taken during the flight from the outside of the enclosures. Two vinyl enclosures preventing dust mitigation with P100 filters as pressure regulator.

To prevent dust contamination the experimental subsystem is installed inside a 2-stage 0.020" vinyl enclosure (Figure 3.2). Both enclosures were closed with zippers that are then covered with tape for a complete seal. To equilibrate internal and external pressure, there are multiple holes placed in the enclosures with P100 filters mounted to them (Figure 3.3).

3.1.2 Control

The operation of the automated robotic gantry system is executed with a combination of sequential programs running on a Trio controller and controller interfaces running on a Windows machine. The graphical user interface (GUI) is implemented to send motion and data collection commands after passing the experimental parameters. The Trio Controller, via digital drive links (EtherCAT), sends/receives commands to/from the two motor drivers. The GUI communicates with a motion controller interface through telnet (TCP protocol). To communicate with the F/T sensor, an API (Application Programming Interface) is used providing an interface with the NI-DAQmx driver. The NI-DAQmx driver is wrapped in ATI-DAQ C libraries to

facilitate data manipulation. Figure 3.4 illustrates the layers of control and real-time communication between the modules.

A sub-program on the robot controller executes based on the commanded application or sequence of applications, such as terramechanics, soil preparation, cone penetration, emergency. Once a sequence is commanded, a corresponding state machine in the script is immediately executed to realize the desired motions or sequence. Throughout the execution of the motion, relevant data are collected and saved for analysis.

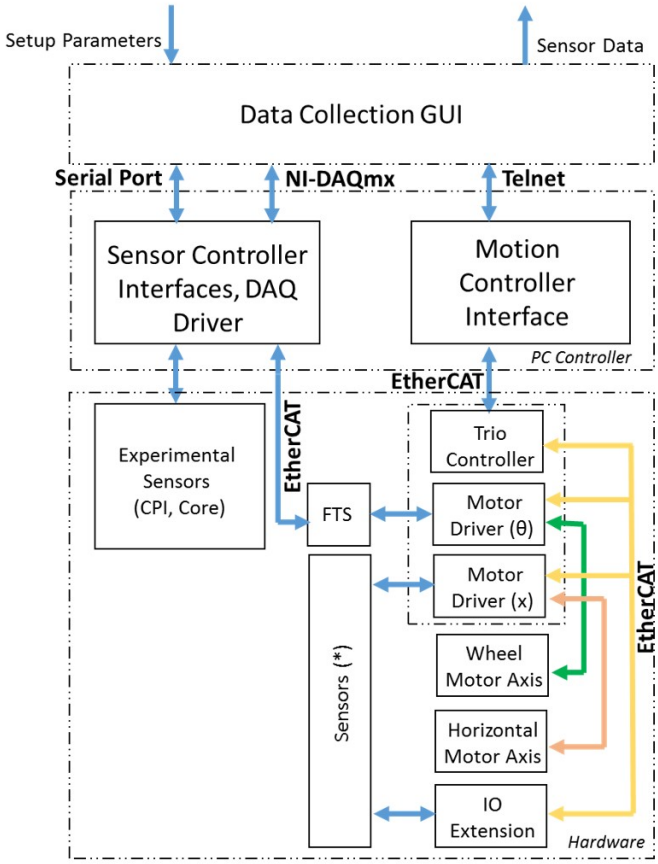

Figure 3.4: Control layers of Automated Terramechanic Testbed. Top layer GUI sends experimentation description and receives data from the real-time background control interfaces; the communications with the hardware handle with real-time processes
* Sensors used for data collection, and automation (Digital/Analogue IO)

3.1.3 Experimental Parameters

Section 3.1.1, and Figure 3.1 in particular, introduced the main input and output parameters of the experimental apparatus: slip and wheel loading; drawbar pull and sinkage (or vertical hub displacement), respectively. These parameters are elaborated here.

A key objective in enhancing the mobility of rovers operating on soft terrain is to reduce the slip at the wheel-terrain interface while improving the traction. The development of thrust leads to shearing action on the terrain surface producing slip. The value of slip is defined as

$$S = \frac{r\omega\text{-}V}{r\omega} \tag{3.1}$$

Where ω and V are the angular and horizontal components of the wheel velocity. r is the original (undeformed) wheel radius; for a flexible wheel (such as ExoMars) if there is a significant deflection along the traverse, there is uncertainty in finding the appropriate radius and calculating the precise slip at any given moment. However, despite the deflection the circumference of the rim does not change (recall it is steel sheet metal) and over a long enough rotation (by angle $\Delta\Omega$, say), the total length of rim rotating post has to approach $r\Delta\Omega$ or the wheel would come apart. Thus, equation 3.1, even allowing for wheel deformation, gives the correct slip on average.

Since changes in the wheel loading affect the ability to develop drawbar pull, and thus impact the rover mobility, in this experimental campaign the performance of the ExoMars wheel is evaluated by varying both the wheel loading (either 164 N or 225 N) and slip value (from 10% to 70%). The wheel loading is adjusted by altering the air pressure in the two pneumatic cylinders that are part of the wheel unit. The air pressure to the cylinders is controlled using an Equlibar QPV1, a high-resolution

electronic pressure regulator, providing a regulated output pressure proportional to the commanded voltage input signal. The wheel loading, W, is the sum of the wheel unit weight and applied forces on the wheel.

The drawbar pull (DP) is a crucial parameter in comparing the performance of the ExoMars rover wheel, as it indicates the ability of the rover to pull/push itself in the direction of the motion. Under steady-state operating conditions, the DP is the difference between the thrust force (T) and the sum of resisting forces (ΣR) acting on the rover as expressed in equation (3.2). DP in fact is the net external force that a vehicle can generate, which can be related to slope climbing ability. The drawbar pull is used to predict a vehicle's slope-climbing performance [23]. Therefore DP is chosen here as the metric for evaluating the performance of the wheel and predicting the maximum slope that the rover can climb at each slip rate (see Figure 3.5b and equation (3.3)). DP/W is approximately constant for different loads, W, within practical operating range [23]. The component of wheel load perpendicular to the slope is reduced to $Wcos(\theta)$, with a corresponding reduction in DP relative to flat ground. This remaining DP_θ ($=DP_0 cos\theta$) must then balance the component of load acting parallel to the slop (i.e. $Wsin(\theta)$. As it can be seen from Figure 3.6, the DP at a given slip value is used to obtain the maximum slope that the rover can potentially climb without exceeding that particular slip value.

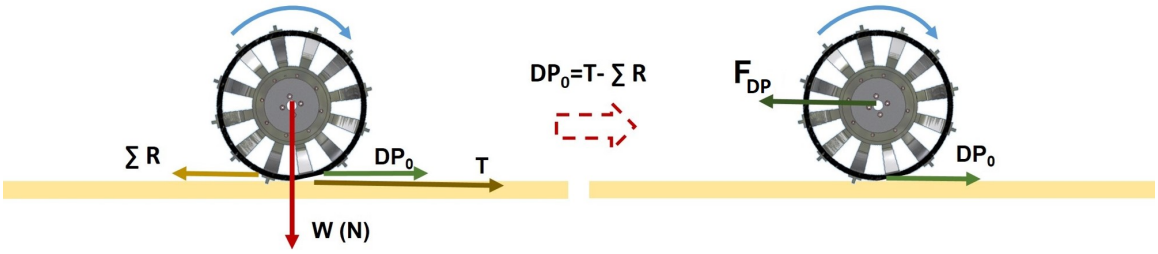

(a) DP generated on flat terrain

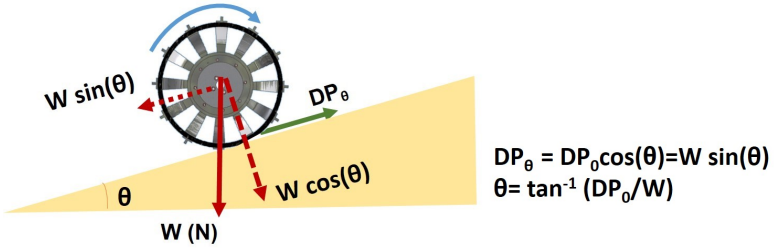

(b) DP generated on an inclination

Figure 3.5: DP generated at each slip rate can be used to estimate maximum climbing angle at that particular slip (a) DP generated is balanced by a reaction force, sensed by force torque sensor (F_{DP}) (b) DP generated on inclination is balanced by gravitational resistance (i.e $Wsin(\theta)$)

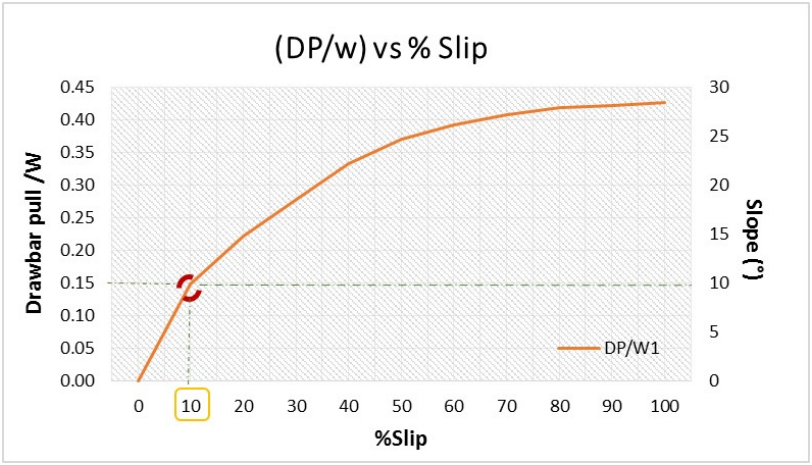

Figure 3.6: General trend of DP and slip at a specific loading

$$DP = T - \sum R \tag{3.2}$$

$$\theta = tan^{-1}(DP/W) \tag{3.3}$$

We know that development of thrust is related to slip, consequently DP is a function of slip. There are a few different methods to study the relationship between slip and DP for a single wheel depending on the objective of the analysis, which will briefly be discussed further in section 3.1.4. In this experiment, DP is measured by the F/T sensor connected to the wheel unit during slip-controlled traverses.

Measuring the rover sinkage provides data for predicting the performance of the driving wheel and also the response of the terrain to a specific loading. Sinkage is a function of slip rate. The wheel sinkage is related to the vertical hub displacement of the wheel. In this experiment, sinkage is estimated from the vertical hub displacement of the wheel as measured by a potentiometer attached to the wheel unit. The wheel hub displaces vertically due to sinkage but also due to wheel deflection. At this point wheel deflection is assumed to stay constant throughout any given test with constant wheel loading. In this thesis, the presented average value of sinkage is the average of all the sinkage reading for the duration of the traverse (average of dynamic sinkage). Maximum sinkage is the maximum sinkage reading taken by potentiometer during the traverse.

At equal soil strength, higher sinkage generates higher resistive forces. These resistive forces act against the thrust, and therefore result in a reduction of DP. However, at equal sinkage the soil with higher strength generates higher resistive forces and thus cause a reduction in DP. Any variation in resistive forces can be attributed to both sinkage and/or soil strength.

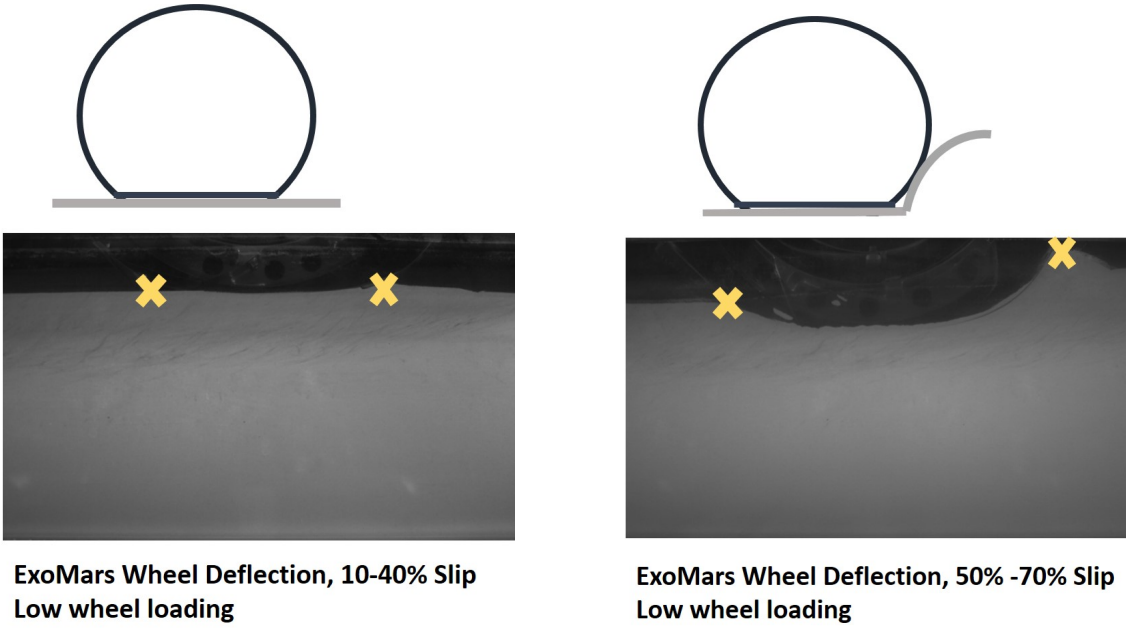

(a) Low slip, low wheel loading

(b) High slip, low wheel loading

Figure 3.7: Exomars wheel traveling on flat terrain

Figure 3.7 shows the interface of the ExoMars flexible wheel with ES-2 soil at low and high slip (the latter exhibiting dynamic sinkage). This sinkage is complex and generated depending on the slip, the wheel characteristics, terrain reaction forces, and the soil bearing capacity.

In addition to Drawbar pull and sinkage, motor currents, velocities and torques are also collected. The motor current is used to validate the motor performance and to confirm the F/T sensor data. The velocity from both motors was collected to verify the commanded slip. The angular velocity of the wheel was kept constant at 0.15 rad/sec (for a constant $r\omega$ value of 20-21mm/sec) in all operations.

3.1.4 Slip Control

Slip-control entails considering speed control mode of operation. In this experimental campaign, the wheel rotational velocity is kept constant during the motion indepen-

dent of all other experimental parameters while the horizontal velocity is adjusted based on the commanded slip.

One method of studying a single wheel performance under the steady-state condition is slip-control where the controller commands the speed of horizontal and rotational motion based on the defined slip. In this condition, the wheel generates DP which can be measured via the reaction force generated at the F/T sensor. As it is shown in Figure 3.8, in this method slip is an independent parameter and DP is the dependent parameter measured as a function of slip.

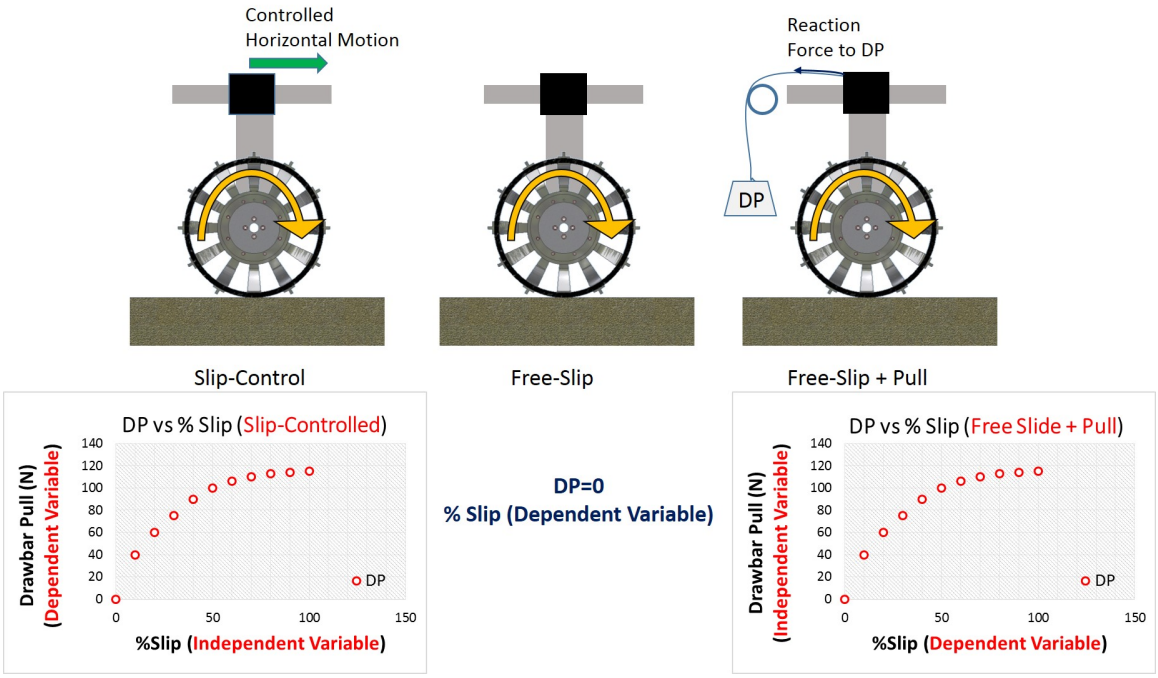

Figure 3.8: Three study DP vs. slip using a single wheel setup

Another method used for this type of investigation is free-slip control where a self-propelled wheel drives itself horizontally (as was done by Kobayashi [34]). In this case, the wheel generates zero DP and if enough thrust is generated in the wheel-terrain interface it will balance the resistance of soil against the wheel motion. This thrust introduces shearing at the wheel-terrain interface resulting in shear displacement in

the soil and causing the wheel to slip. The slip can be measured from the sensor reading of the horizontal traverse speed and the commanded angular speed.

The third method (also shown in Figure 3.8) can be called free-slip+pull where an opposing force is applied resisting the forward motion. In this case, the wheel must generate a DP equal to the applied force to maintain forward motion at some resulting slip. In this method, DP is an independent parameter and slip is dependant upon it. By adjusting the force opposing the motion the resulting slip is assessed.

To investigate the characteristics of the wheel, slip-control method is implemented here and the developed DP is studied. As mentioned before, slip is a function of wheel radius, angular and horizontal velocities, implemented based on equation (3.1). Therefore the deflection of the flexible wheel during the traverse impose some uncertainties in the actual instantaneous slip.

Controlling the slip of the wheel could be done by either changing the rotational speed and keeping the horizontal speed constant or altering the horizontal speed and keeping the rotational speed constant. For all experiments, the rotational speed is kept at the constant speed and the horizontal speed is adjusted based on the commanded slip. In all experiments, steady-state condition is reached promptly (within 1 second). Figure 3.9 demonstrates how quickly both driving motors reached the commanded velocity satisfying the slip condition.

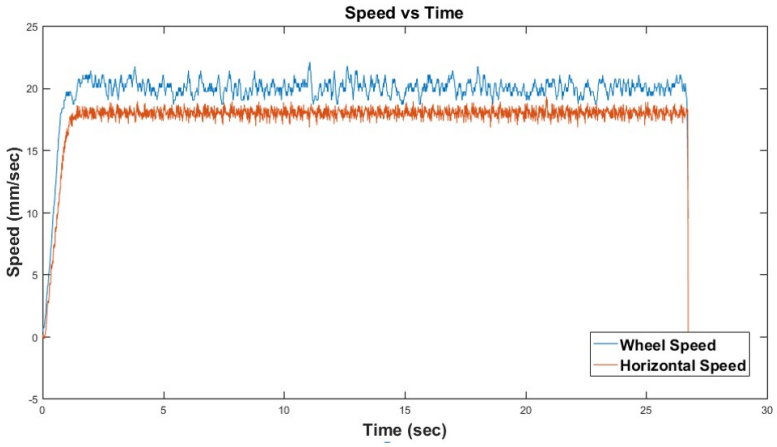

Figure 3.9: Steady state condition for slip reached within 1 sec.

3.2 Optical Flow

To analyze soil motion observed through the glass sidewall of the sandbox, optical flow is used. Optical flow is a dense motion estimation technique, where motion is calculated at each pixel of the image between consecutive images. The technique produces two displacement fields, for horizontal and vertical motion, in units of pixels. This technique aims at satisfying two constraints to estimate the displacement fields. The data conservation constraint is based on an assumption that the intensity of a given point of interest at time t will be conserved in the subsequent image at $t+1$. The spatial coherence constraint assumes neighboring pixels are likely to have similar motion. An objective function combining these two terms is then optimized.

There has been much research done in the literature to improve the model of the objective function and optimize the model approximation. In this section, the classical model with robust estimation, as well as another modern formulation of optical flow are described. Furthermore, the key implementations producing valuable and meaningful visualization are elaborated. The mathematical framework of optical flow that is summarized here is a formulation presented by Sun et al. [8] and [61] that were developed over the years for general flow estimation.

3.2.1 Overview of Optical Flow Processing Technique

An example of optical flow output is presented in Figure 3.10 estimating the displacement between two frames. The videos from the wheel-soil interaction are collected in black and white at 37 frames per second. The video is converted to a set of images where each consecutive image pair is processed. Optical flow evaluates horizontal and vertical displacements between each pair of images at each pixel, in units of pixels. The technique estimates the displacement fields by satisfying two constraint assumptions; data conservation and spacial smoothness.

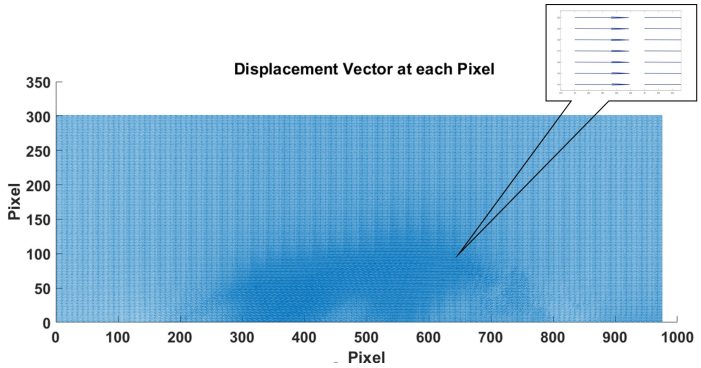

(a) The velocity field estimated between two frames. Larger displacement vectors detected at the wheel (note:y axis flipped)

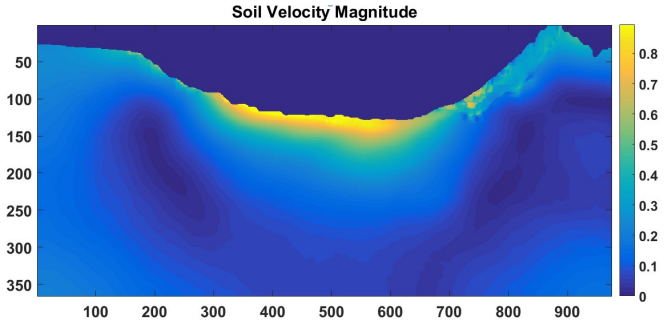

(b) Magnitude of the velocity field presented in Figure 3.10a. The dark blue is the wheel extracted from the image in the colormap. The visualization technique will be elaborated in Section 3.2.3

Figure 3.10: An example of optical flow output and post processing of the velocity field between two frames of wheel-soil interaction

Data conservation assumes that in spite of the regions of motion in an image, the appearance of those patterns stays roughly the same. This translates into the Equation:

$$I(x+u, y+v, t+1) = I(x, y, t) \tag{3.4}$$

The intensity of the image at location *x,y* at time t is assumed to be the same at time *t+1* in the next image given the motion *(u,v)* with the pixels just offset by u and v.

Spacial smoothness assumes neighboring pixels are likely to belong to the same surface, therefore, the neighboring pixels flow similarly.

$$u_s = u_n \tag{3.5}$$

$$v_s = v_n \tag{3.6}$$

where u_s is flow at pixel s and u_n is the flow in each of the 8 neighboring (horizontally, vertically and diagonally) pixels in a defined fixed window W_s. u and v represent horizontal and vertical flow fields, respectively.

The objective functions of the data term and spatial term are quadratic penalty formulations that optical flow attempts to minimize.

$$E_D(u, v) = (I(x+u, y+v, t+1) - I(x, y, t))^2 \tag{3.7}$$

$$E_S(u, v) = \sum_{n \in W_s} (u_s - u_n)^2 + \sum_{n \in W_s} (v_s - v_n)^2 \tag{3.8}$$

E_D and E_S are quadratic error functions for data term and spacial term respectively. Equation (3.7) can be approximated by a first order Taylor series expansion as:

$$I_x u + I_y v + I_t \tag{3.9}$$

where I_t is the temporal derivative of the image, I_x and I_y is the partial derivative in x and y-direction, respectively. Recall that u and v are the unknown flow vectors.

The objective error function to be minimized after Taylor approximation over a local region W_D is:

$$E_D(u, v) = \sum_{(x,y)\in W_D} (I_x u_s + I_y v_s + I_t)^2 \tag{3.10}$$

Affine flow is assumed in order to model the flow field around each pixel with a parametric function. The formulation *u(x,y;a)* presents a flow field within a region of an image that integrates the information of the parametric constraint to minimize the constraint over that neighborhood by optimizing parameter set a. The affine flow assumption contrasts against the spatial term in which the neighbourhood is assumed to move constantly. W_D may be a small local neighbor window or even the entire image.

The affine flow spatial constraint is

$$\mathbf{u}(x, y; a) = \begin{bmatrix} u(x, y) \\ v(x, y) \end{bmatrix} = \begin{bmatrix} a_1 + a_2 x + a_3 y \\ a_4 + a_5 x + a_6 y \end{bmatrix} \tag{3.11}$$

Therefore the objective function considering the affine flow is formulated as

$$E_D(a) = \sum_{(x,y)\in image} ((\bigtriangledown I)^T \mathbf{u}(a) + I_t)^2 \tag{3.12}$$

The complete objective function to optimize is

$$E(u, v) = E_D(u, v) + \lambda E_S(u, v) \tag{3.13}$$

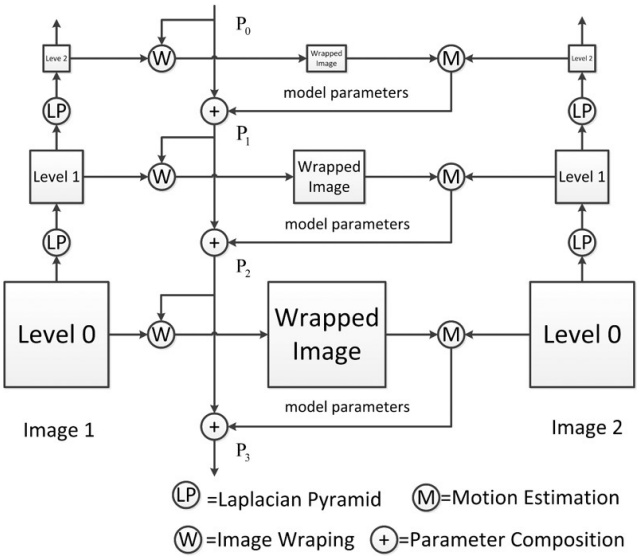

(a) Flow chart of a hierarchical motion estimation algorithm

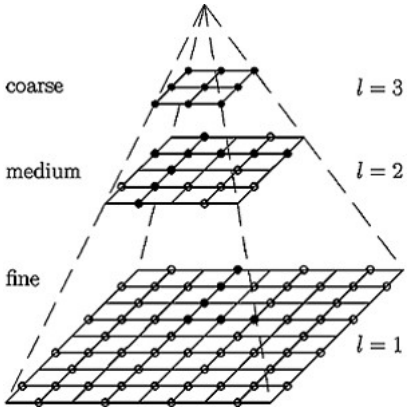

(b) Image Pyramid Construction

Figure 3.11: Motion estimation flow chart, (a) a level corresponds to a level in image pyramid where motion estimation executed at each level [67] (b) Three level pyramid [62]

λ in equation (3.13) represents a weighting factor indicating how much to believe the data. A higher λ means the spatial smoothness term dominates.

There are two techniques used when solving for the overall motion field; iterative refinement and coarse to fine estimation. Iterative refinement estimates velocity at each pixel by solving $\Delta I(u, v) + I_t = 0$, and then warps I_t towards $I_t + 1$ using the estimated flow field and repeat, until the solution converges.

The coarse to fine estimation (Figure 3.11b) technique enables larger than a pixel motion approximation. By reducing the resolution of the original image with respect to the magnitude of the motion, the large motion is contained in one pixel. In order to deal with the problem of distortion due to downscaling an image (aliasing problem), each image is first filtered and smoothed before sub-sampling (Figure 3.11a).

For every image, a Gaussian pyramid is constructed with the lowest spatial resolution at the first level computing the change in flow estimate and project the motion to

the next level in the pyramid. At each level of the pyramid, the quadratic error norm function is minimized to estimate the flow field. Then using the estimated flow field, the first image is wrapped towards the next image and up-samples. At this point, the algorithm performs the iterative method on the warped image and repeats until it reaches the full resolution of the image. This technique considers large motions while avoiding local minima. When estimating the affine flow the parameters from equation (3.11) are used to warp the first image towards the second image. Then the change in the parameters is estimated using the iterative method to pass on to the next level of the pyramid.

Once estimation of the motion is found, the additional two stages of minimization are used to find global optimal for non-convex function by constructing a convex approximation. Blake and Zisserman [9] developed an extended method of Graduated Non-Convexity by formulating a parameterized piecewise polynomial approximation. A locally convex function $\rho(x, \sigma)$ is defined from the objective function such that $\frac{\delta^2 \rho}{\delta^2 x}(x, \sigma) \geq 0$ and choose a σ that leads to better estimation which is less sensitive to outliers [8].

$$\rho(x, \sigma) = \log(1 + 0.5(\frac{x}{\sigma})^2) \tag{3.14}$$

3.2.2 Comparison of Classic Model & Adaptive Neighbourhood Formulation

Detection of accurate motions and the formulating a framework that has a general applicability is crucial, thus new optical flow algorithms have been developed in the past few years to address accuracy and robustness. One advanced method, discussed here, is extending optical flow to compute adaptive neighbourhoods of related pixels. It is not clear whether such advances are effective for all applications, therefore eval-

uating and comparing the level of accuracy and efficiency of the new algorithm's flow fields is noteworthy.

Even though the classical optical flow estimation has been modified, the original formulation that combines a data term and a spatial term is preserved. A quantitative analysis is performed evaluating the accuracy of the adaptive neighbourhood optical flow compared to the classical method for the application of soil motion estimation (see Section 3.2.3 and Figure 3.17 in particular). Optical flow optimizes the objective function which is a formulation that incorporates the data constancy assumption and expected flow variation model. The adaptive neighbourhood method derives a new objective function that includes a non-local spatial smoothness term. This method utilizes a weighted median filter accounting for the spatial distance and similarity in the intensity of the neighboring pixels. At each step of the pyramid after the warping, the spatial median filter performs and the output is used as an initial estimate of the next level of the pyramid.

This method has advantages for distinct motion boundaries, however, if the neighborhood is a corner or a thin surface the filtering leads to oversmoothing. Weighting the pixels based on the likelihood of correspondence with the surface can improve these cases, meaning introducing weight into the non-local terms.

$$\sum_{i,j}\sum_{i',j'} w_{i,j}^{i',j'}((|\hat{u}_{i,j}-\hat{u}_{i',j'}|)+(|\hat{v}_{i,j}-\hat{v}_{i',j'}|)), \tag{3.15}$$

$w_{i,j}^{i',j'}$ states the probability that pixel i', j' can be associated to the surface i,j. [74] proposed adaptive bilateral filter to regularize the flow computation to account for intensity/motion dissimilarity, and occlusion detection. Yoon et al. [75] implemented window-based weight varies according to intensity similarity, and geometric proximity. Sun et al. [60] demonstrated that the weighted non-local term improves the accuracy on both the training and the test sets.

$$w_{i,j}^{i',j'} \propto \exp\{\frac{|i-i'|^2+|j-j'|^2}{2\sigma_1^2} - \frac{|I(i,j)-I(i',j')|^2}{2\sigma_1^2 n_c}\}\frac{O(i',j')}{O(i,j)} \tag{3.16}$$

Occlusion variable *O(i, j)* is calculated using equation (3.17) [59][60]

$$O(i,j) = \exp\{\frac{div^2(i,j)}{2\sigma_d^2} - \frac{(I(i,j)-I(i+u_{i,j},j+v_{i,j})^2}{2\sigma_e^2}\} \tag{3.17}$$

The first segment of the exponential is to account for the distance of the pixel from the surface; the second segment accounts for the similarity of the pixel. The value of *O(i,j)* for non-occluded pixels is close to one and zero when is occluded. div is a divergence function for *div(i,j)<0* which is defined as equation (3.18) and otherwise is zero.

$$div(i,j) = \frac{\partial}{\partial x}u(i,j) + \frac{\partial}{\partial y}v(i,j) \tag{3.18}$$

Sun et al. [60] stated that applying this technique improved the results at the motion boundaries significantly and improved the average end-point error comparing an estimated optical flow vector $\mathbf{u_{estimated}}$ with a ground-truth optical flow vector by 10-20% (End-to-end point error is defined as the scalar length of difference vector as equation (3.19)) .

$$||\mathbf{u_{estimated}} - \mathbf{u_{ground\ truth}}|| \tag{3.19}$$

3.2.3 Using Optical Flow to Visualize Wheel-soil Interaction

In the experiments conducted for this thesis, soil motion below a wheel is visualized. This information can then be analyzed or even related to soil stress via a constitutive equation. The camera is attached to the horizontal axis and moving alongside the wheel capturing the high-resolution image frames of the wheel-soil interaction from the mirror reflection (see Figure 2.2). The optical flow estimated flow fields are in

the camera frame and by subtracting the camera motion from the horizontal flow the reference frame will be transformed to a frame that is static relative to the sandbox. To estimate the camera motion, the median horizontal component of the flow field is considered (majority of soil in frame is assumed static). One of the cross-validations used during the analysis is comparing the calculated camera motion with that measured by the horizontal axis encoder, to ensure agreement (see Section 4.2.5). In this Section, the key elements of post-processing are discussed which facilitate the visualization of the optical flow output flow fields.

Averaging Flow Fields

To discern a coherent pattern from the flow fields and reduce the transient noise, subsequent velocity fields are averaged. Compliant wheels induce smaller soil motion than rigid wheels; therefore signal averaging can lower the prevalence of transients in soil motion estimation, thus effectively boosting the signal to noise ratio. Figure 3.12 shows three single noisy frame pairs and a smoother flow, averaged over 37 consecutive frame pairs capturing 1 second of wheel-soil interaction. Every 203 successive frame pairs are averaged over the course of 812 frames (each averaged flow field represents approximately 5-second time-span). This signal averaging aims at capturing the influence of sinkage and effect of grouser motion on the shearing interface. The error magnitude is correlated to the signal magnitude indicating that the error will be larger where there is a considerable amount of flow (as will be shown later in Figure 3.18).

Normalizing Flow Fields

The optical flow estimates the displacement from an image to the next, therefore to convert to velocity field the displacement field is multiplied by the frame rate and spatial pixel size. A frame rate of 37 fps are set for all experiments, respectively. A pixel size of 0.4 mm is set for all the experiments discussed in this paper. As discussed

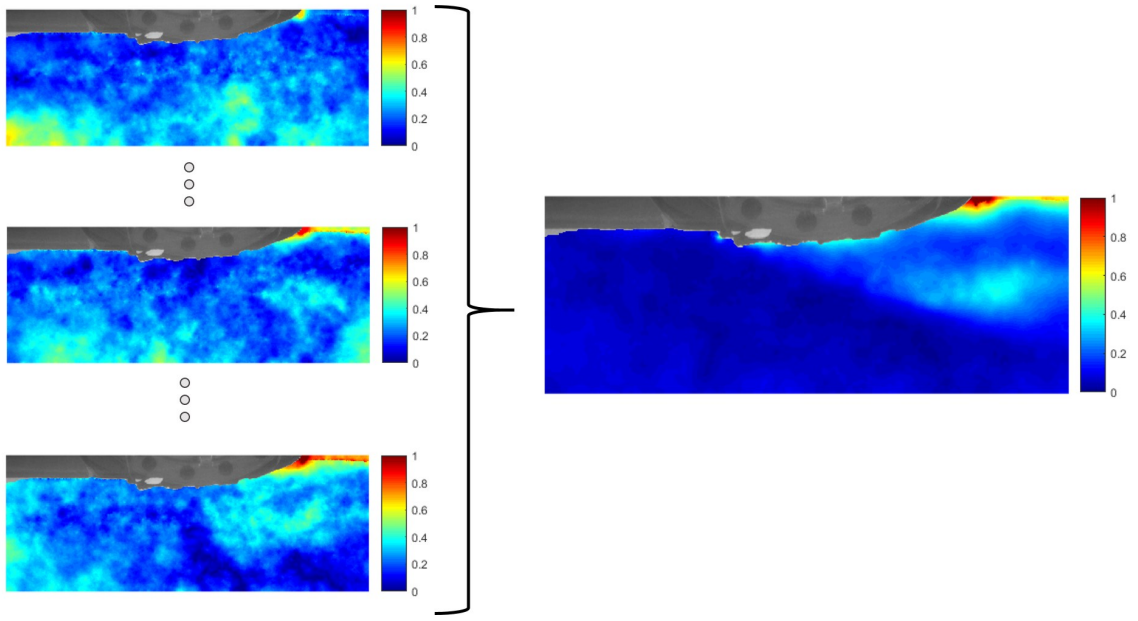

Figure 3.12: Image on the right depicts an average of flow fields for 1 sec of wheel-soil interaction (37 frame pairs) whereas images on the left is representing 0.03 sec of this interaction (single frame pair). Note that all images shown here have been post processed (i.e. normalized and clustered)

in Section 3.1.3, the rotational speed is kept at the constant speed of 0.15 rad/sec and the horizontal speed is adjusted based on the commanded slip. Rim speed is calculated from equation (3.20) where ω is angular speed, rω is the average rim speed of the rotating wheel, and V is horizontal velocity.

$$V_{rim} = r\omega - V \tag{3.20}$$

After smoothing the estimated flow field, it is then normalized with respect to rim speed based on slip ratio presented in Table 3.1.

Clustering Flow Fields

In this technique, as described by Skonieczny et al. [54], two stages of k-means clustering are performed. K-means is an unsupervised learning method to build models that enable us to learn the clustering of unlabeled data points. This technique is

% Slip	Rim-speed (mm/sec)	Rim-speed (pixel/sec)
10	2	0.69
20	4	1.37
30	7	2.06
40	9	2.75
50	11	3.43
60	13	4.12
70	15	4.18
80	18	5.49
90	20	6.18
100	22	6.87

TABLE 3.1: Rim-Speed Based on Slip

applied to classify the regions between static and moving soil and also to find the boundary between soil and non-soil. K-means is initialized by randomly selecting k data points as the centroids of the classes. Each data point is then assigned to the class of its nearest centroid. To update the centroid, all data points that fall into the cluster are considered to recompute a new centroid. The algorithm iterates, between assigning classes and updating centroids, until no clustering assignment changes.

To identify and separate the segment of the image that contains soil from the rest, pixel intensity is used. As suggested by Skonieczny et al. the background of the test is much darker than ES-2 simulant, which is relatively white. After the first clustering, binary dilation and erosion are performed to take care of any remaining discontinuity in the soil region remained after the clustering. (for more information, see [26]) In the image, dilation is performed to enlarge the boundaries of the pixel foreground regions, which closes small holes in those regions. On the other hand, erosion erodes away the boundaries of regions of foreground pixels thus thin stripes are removed.

The second stage of clustering can be used to separate the flow regions into relatively stationary soil and that with high magnitude flow. A series of dilation and erosion is performed again to correct any existing fragmentation. The boundary sep-

arating these two regions of high and low-velocity field is regarded as a shearing interface or shear failure in the soil.

Visualization

The estimated flow field, now in an inertial reference frame, is then translated into polar coordinates for visualization as magnitude and direction. The flow field visualization consists of two segments: the upper image shows the velocity magnitude while the lower shows soil flow direction (see Figure 3.15). For velocity magnitude, the colormap ranges from dark blue, representing static soil, to warmer colors (red is the maximum). Flow direction is denoted by the color wheel.

When velocity magnitude is close to zero, the direction associated with that low velocity can be easily swayed by the slightest noise. For this reason, only regions in the directional flow field that correspond to significant velocity magnitude are considered.

Ground Truth Testing

The accuracy of the optical flow estimation algorithm and the adaptive neighbourhood formulation are evaluated on a baseline. To compute the soil flow output error, layers of soil were flattened covering a plate (see Figure 3.13a). The plate is then rotated by precise angular displacement of 0.02944 ± 0.00003 rad and the two images were taken and analyzed as the baseline. Figure 3.13b is the ground truth displacement (left) and direction (right) estimation of the motion between the two images shown in Figure 3.13a. The largest displacement at the corners of the image is approximately 16 pixels, or 3.2 mm which is illustrated in red.

(a) Two images before and after an angular displacement of 0.02944 rad

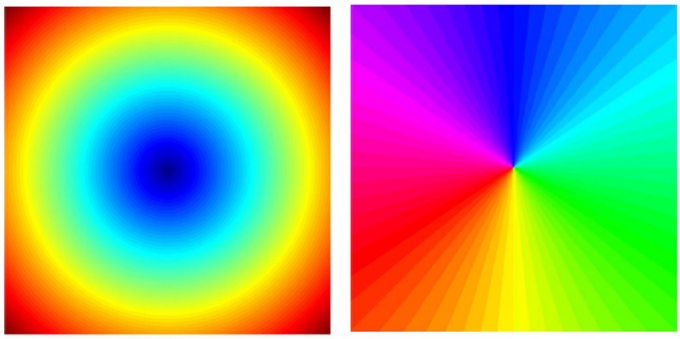

(b) Ground Truth displacement of 0.02944 rad

Figure 3.13: Ground truth test, (a) Soil-covered test plate, A round dark pin marks the center point of rotation for ground-truth testing (b) Ground truth displacement magnitude (left) and direction(right) of prescribed 0.02944 rad rotating plate

The replication of this ground-truth displacement using classic robust optical flow is investigated first. The regularization parameter, λ, smooths over the motion boundaries by penalizing the energy function for outliers, consequently the improvement of the estimated accuracy using this parameter is application dependent. Figure 3.14 illustrates the results of the parameters λ=0.1 and, λ=1 with classic optical flow. Increasing λ improves the result relative to the benchmark (i.e. compared to the Figure 3.13). In Figure 3.14b the motion boundaries are blurry and less distinct compared to Figure 3.14a. Moreover, in the direction field where the parameter λ is set to 0.1, the location of the centre point becomes imprecise. From above it can be observed that for classic optical flow an increase in λ parameter improves the results for this benchmark. However, λ=1 oversmooths the wheel-soil interaction output flow as seen

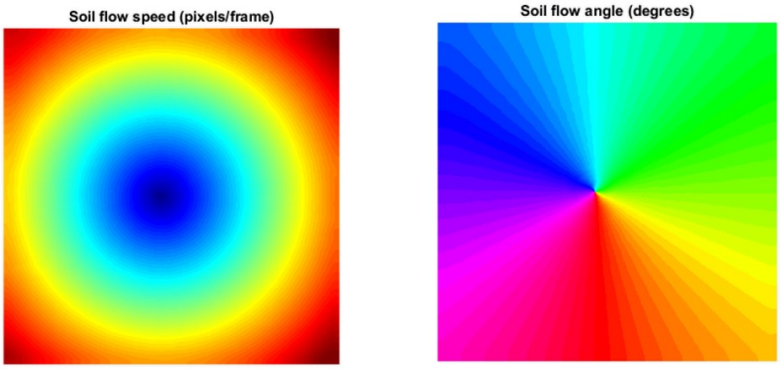

(a) Generic optical flow for ground truth, λ=1

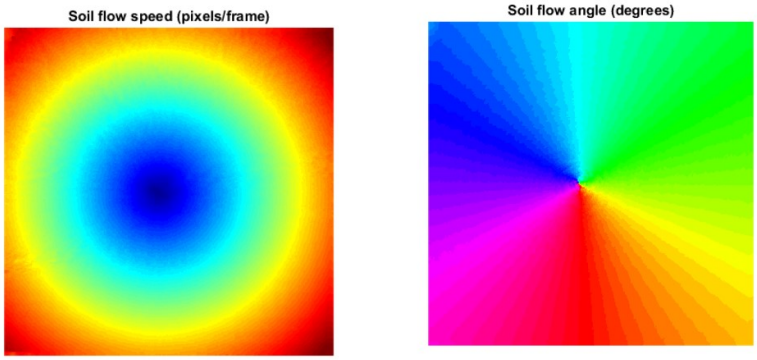

(b) Generic optical flow for ground truth, λ=0.1

Figure 3.14: The motion boundaries in the soil flow speed (left) are smoother for λ=1 and blurred for λ=0.1, The soil flow angle (right) has a more distinct centre for λ=1 and blurred for λ=0.1

in Figure 3.15, thus λ=0.1 is selected to preserve the motion boundaries from fading despite greater outliers.

The adaptive neighbourhood algorithm is fairly insensitive to regularization parameter variations (see Figure 3.16).

The mean square error is calculated at each pixel to quantitatively evaluate both algorithms. The actual velocity at each pixel is subtracted from the output flow field computed by the optical flow. Then the distribution of the error histograms are compared (see Figure 3.17). On average the adaptive neighbouring formulation presented an improvement over the classical optical flow.

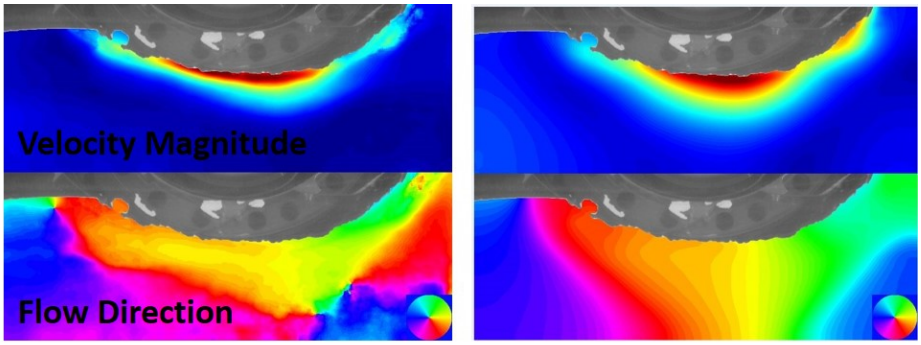

Figure 3.15: Effect of λ parameter in the wheel-soil interaction analysis. The image on the right is analyzed with λ=1 whereas image on the left is presenting the output of λ= 0.1. The effect of parameter λ is much more noticeable in the flow direction

Despite higher accuracy and robustness, the adaptive neighbourhood formulation introduced high computational cost and complexity in exchange of preserving motion details. Depending on the mask size and the performance of the algorithm, the advanced formulation will increase the computation at least by O(2*M*N*k) for every pair of images, where k is the mask size and MxN is the pixel size of the image. Even though the classic formulation is sensitive to parameter variation and demonstrated less robustness under noise, by choosing appropriate parameters a sufficient degree of motion detail can be conserved and captured.

In both algorithms the magnitude of errors observed to be higher near the edges where there are greater motion magnitudes (see Figure 3.18).

Pyramid level is another application-dependent parameter, defined based on the motion magnitude. The motion of very small features moving fast from frame to another disappear in the first level of the pyramid, requiring levels of sub-sampling to capture these displacements. The magnitude of soil motion in this application is not large and the regions of soil motion are not too small, thus pyramid levels higher than 3 results into outputs with the same accuracy. Note that in order to ignore the outliers, and yet remain sensitive to the error, Lorentzian is used as the robust error function. The optical flow parameters decided upon to analyze the terramechanics application is presented in Table 3.2.

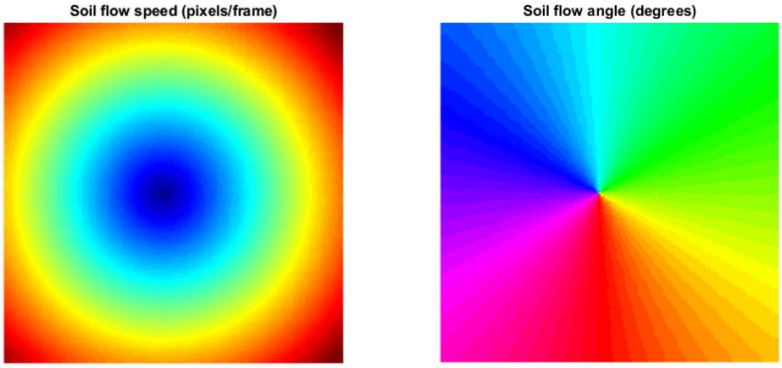

(a) Adaptive neighbourhood optical flow for ground truth, λ=1

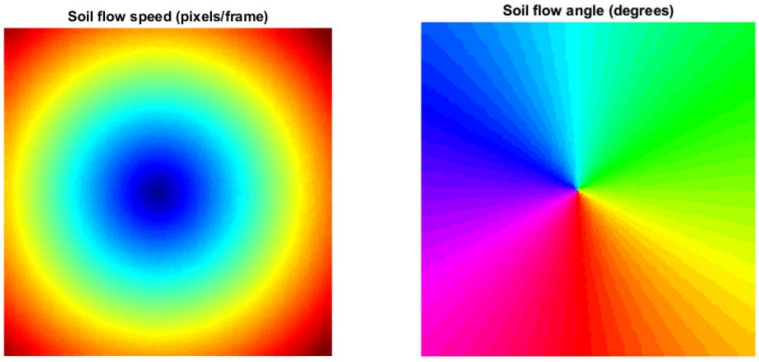

(b) Adaptive neighbourhood optical flow for ground truth, λ=0.1

Figure 3.16: Effect of change of λ on adaptive neighbourhood optical flow is insignificant on both soil flow speed and angle compared with Figure 3.14

TABLE 3.2: Optical flow parameters used for terramechanics analysis

λ	**Pyramid Levels**	**Spacing of Pyramid Levels**	**Max. # of Iterations**
0.1	3	2	10

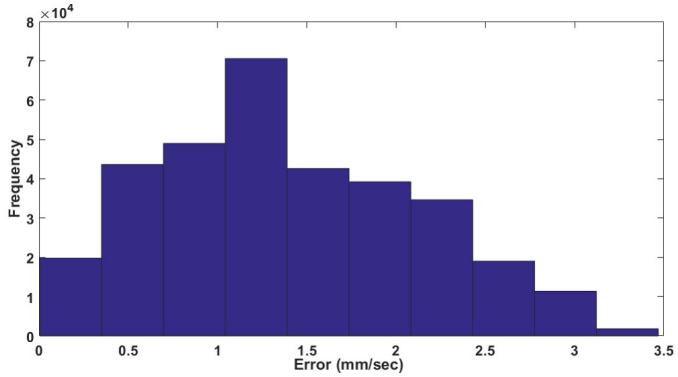

(a) Classical optical flow, distribution of motion error

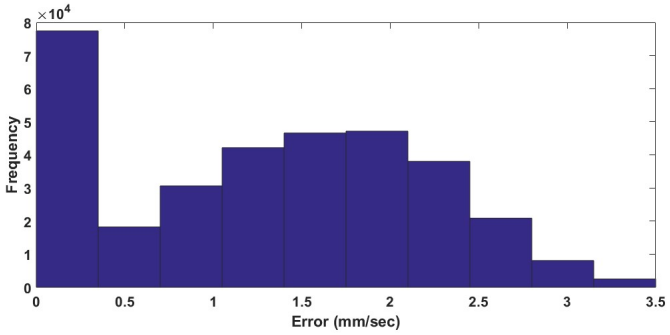

(b) Adaptive neighbourhood optical flow, distribution of motion error

Figure 3.17: Square mean error histograms between estimated and actual (ground truth) velocity fields for (a) classic and (b) adaptive neighbourhood optical flow.

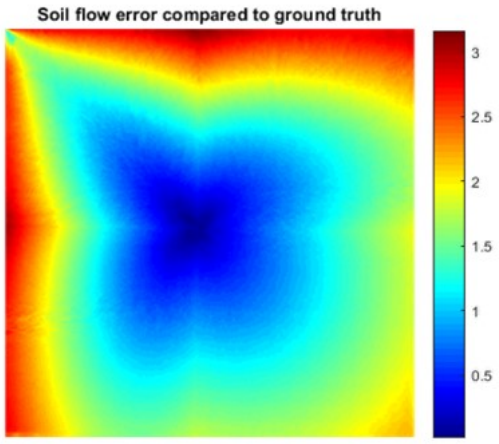

Figure 3.18: Magnitude error in pixels (classic optical flow), shows clear dependency of the error on motion magnitude.

Chapter 4

Experimental Campaign

4.1 Ground Based Experimental Campaign

This section concerns on-Earth terramechanics test results and optical flow analyses of ExoMars wheel-soil interactions. The experimental setup, input parameters and test cases for this campaign study are explained in Chapter 3. Later the results discussed in this section will be contrasted against the results in reduced gravity (see Section 4.2.4).

4.1.1 OGE Terramechanics Results

Terramechanics results are collected and analyzed for slip values from 10% to 70%, and for wheel loads of 164 N and 225 N. Due to the spacing of the ExoMars wheel's grousers and leafspring elements, the terramechanics data exhibit regular periodicity. Figure 4.1 shows the wheel load vs time for a nominal 164 N as well as 225 N loading. Sinkage and DP vs time also exhibit periodic effects, as can be seen in Figure 4.2 and Figure 4.3, respectively. Note that the periodic nature does not preclude general trends developing over time, such as increasing sinkage throughout the 70% slip experiment. However, this increasing sinkage occurs in a specific pattern of alternating rises and plateau segments (see Figure 4.4). It appears at higher slip, the periodic patterns of

sinkage (plateaus) become more distinct. At higher slip the periodic features of DP get slightly distorted.

Average sinkage and Max sinkage are summarized for all tests in Figure 4.5a and 4.5b, respectively, and are computed as described in Section 3.1.3. The figures demonstrate the direct relationship between sinkage and slip. It is also possible to extract finer detail on the results by computing the average sinkage for each rise and plateau segment of a test, as shown in Figure 4.6.

Drawbar pull, summarized for all tests in Figure 4.7 is the computed average of three periodic patterns extracted; containing three peaks from the DP data presented in Figure 4.3. Figure 4.7 also illustrates the effect of wheel loading on DP at each slip. Increasing the loading improves the generated DP by about 20-30% on-ground, uniformly across different slip rates.

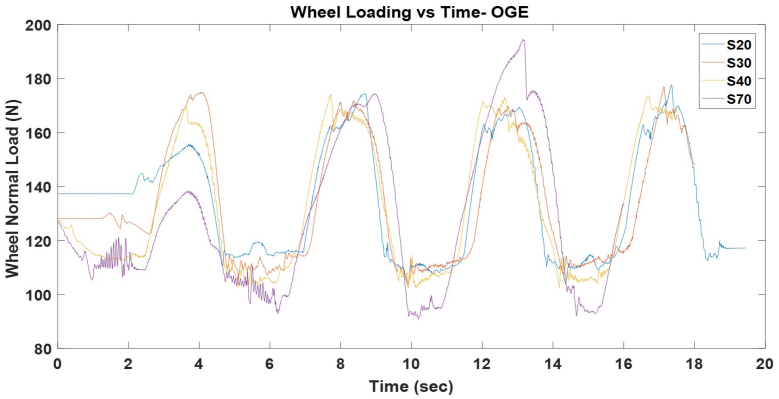

(a) Wheel Load vs Time, applied wheel load of 164 N, slip 20%-70%

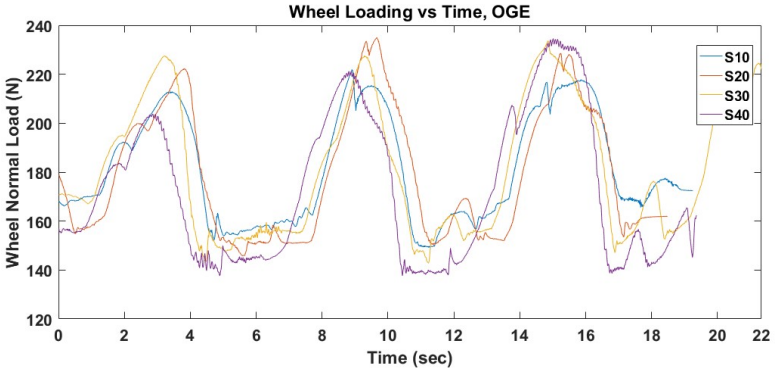

(b) Wheel Load vs Time, applied wheel load of 225 N, slip 10%-40%

Figure 4.1: Wheel loading pattern at 164 N & 225 N at different slip ratios, OGE

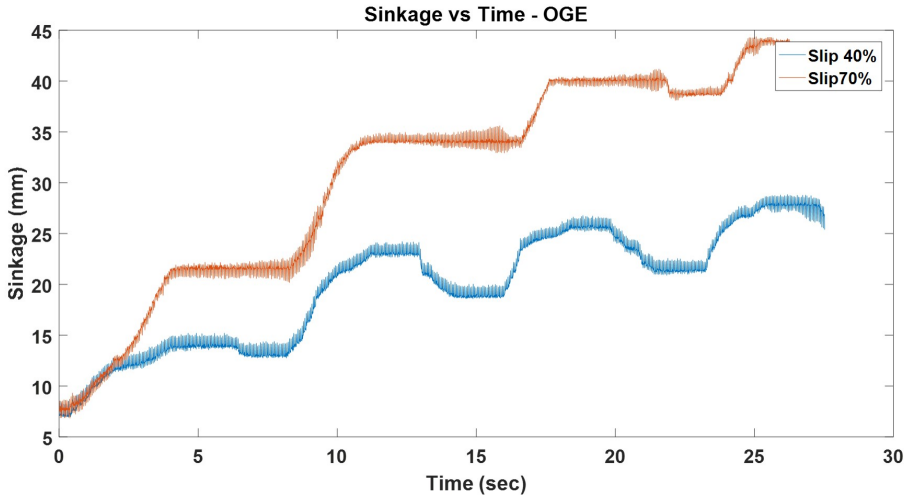

Figure 4.2: Sinkage vs Time, OGE, slip 40% & 70% showing the influence of slip on the periodic pattern

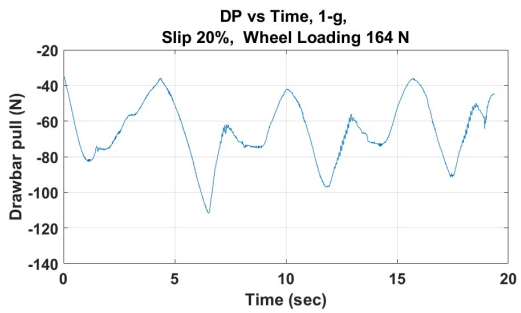

(a) DP vs time, at 20% slip, OGE

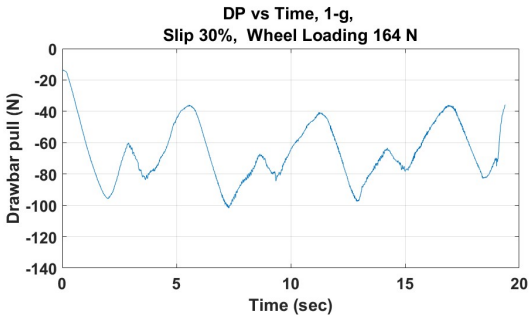

(b) DP vs time, at 30% slip, OGE

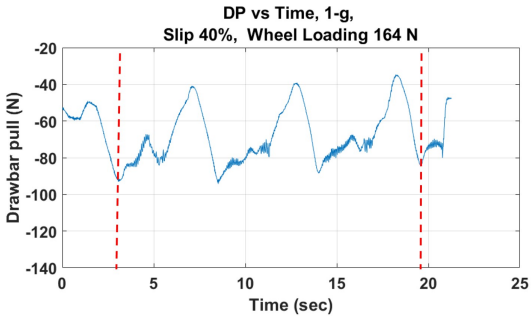

(c) DP vs time, at 40% slip, OGE

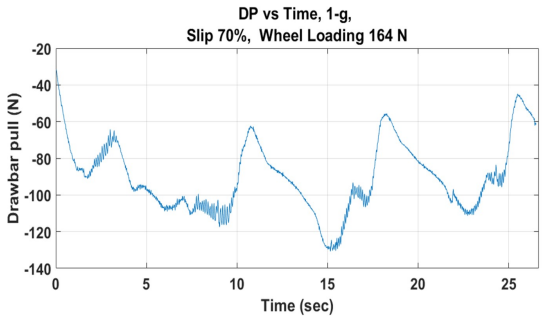

(d) DP vs time, at 70% slip, OGE

Figure 4.3: Pattern of DP at 10%-70% slip, OGE. The patterns become less periodic and less alike at greater slip ratios

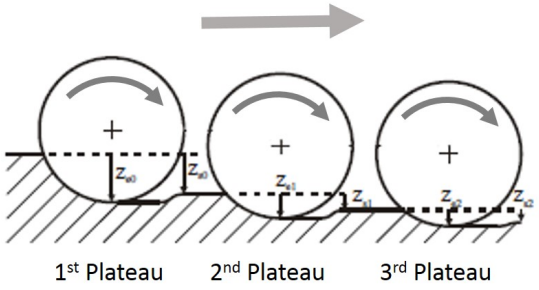

Figure 4.4: Sinkage under running gear [71]

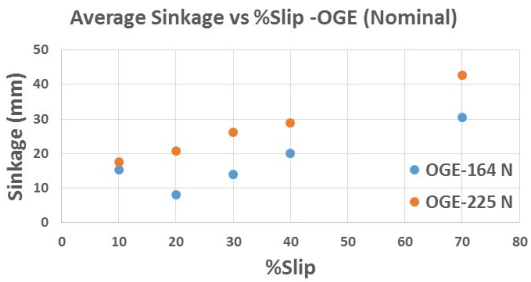

(a) Average Sinkage vs Slip, OGE

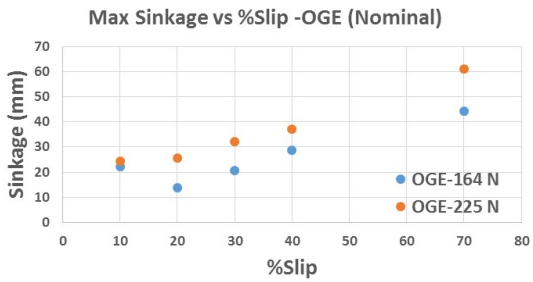

(b) Max Sinkage vs Slip, OGE

Figure 4.5: OGE nominal sinkage data (a)Average of sinkage at 164 & 225 N wheel loading, slip 10-70% (b)Max of sinkage at 164 & 225 N wheel loading, slip 10-70%

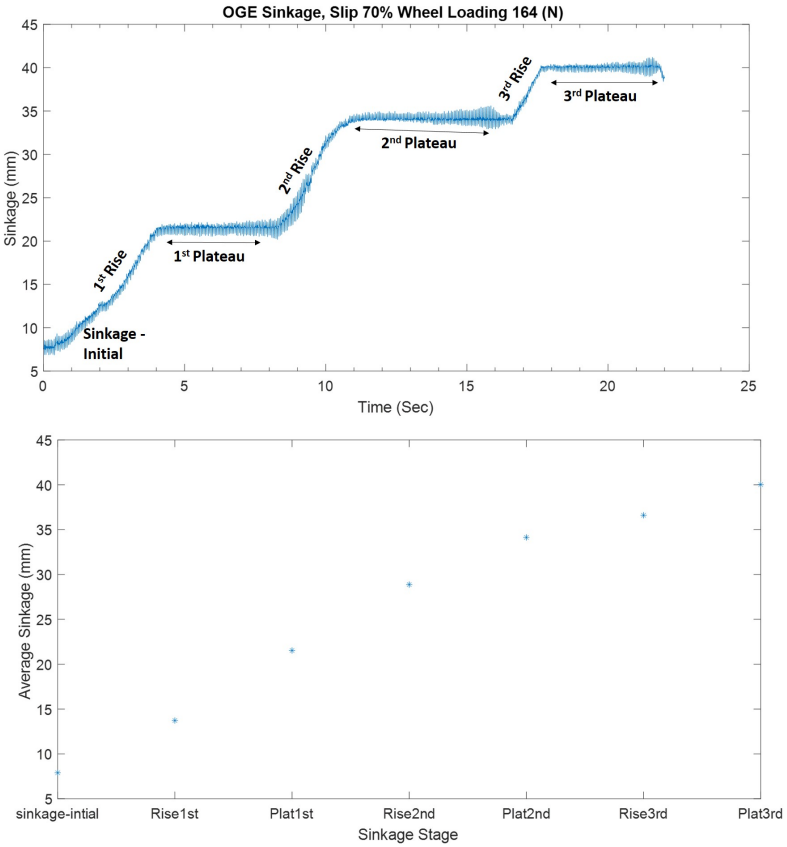

Figure 4.6: Sinkage vs Slip, at 70% Slip, OGE

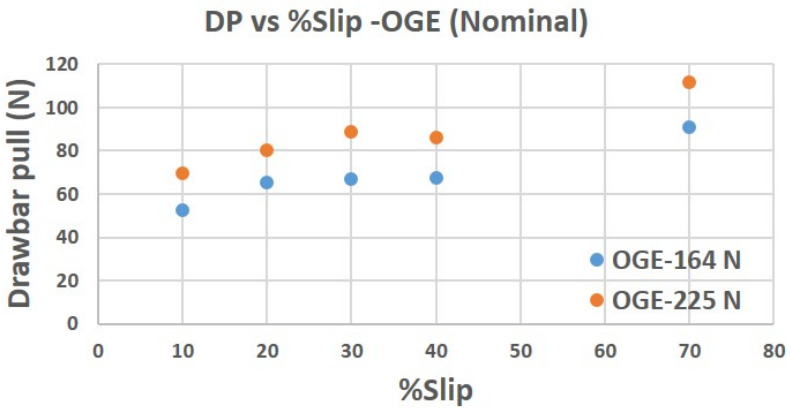

Figure 4.7: Dp vs Slip, OGE at 164, 225 & 300 N wheel loading

4.1.2 OGE Optical Flow Results

The objectives of visualizing on-ground experiments (1-g) are to analyze and understand the performance of ExoMars's flexible wheel as well as to identify the chief discrepancies with the partial gravity experimentation. This visualization technique facilitates a qualitative and quantitative study of the interaction influenced by gravitational changes. These analyses provide a better understanding for future design and improvement of flexible rover wheel by providing insight into the soil shearing regions, contour of the regions, the direction of soil flow and the effect of grousers at the contact points with soil.

The optical flow analysis presented here depicts the soil motion magnitude and direction of velocity fields as the wheel is rotating counterclockwise while driving right to left, as shown in the figure 4.8. For a guide to interpret the visualization results see section 3.2.3. In each of these figures, the 20 seconds worth of test data are divided into 5-second segments that are analyzed separately. Each column shows the average soil motion over a 5-second segment of the time-span, where the segmented time-span is to capture time-varying phenomena. The black rectangles enclosing the regions of soil are highlighting the region being compared. The dashed red lines are illustrating the maximum depth of motion observed for each visualization. Note that, the illumination (by floodlights at both ends of the mirror) sometimes introduces artifacts at the lower corners of the images (see Figure 4.9, and Figure 4.12).

Figure 4.9 through 4.11 show the optical flow analysis for tests at 20%, 40% and 70% slip. At slip values of 40% or below, the soil flow magnitude and direction does not change substantially with respect to time, whereas at 70% slip the soil flow is time-dependent. In Figures 4.9 and 4.10 (20% slip and 40% slip respectively), there is little variation in the soil flow results between time segments. On the other hand, at 70% slip (Figure 4.11), soil flow results significantly differ and the level of sinkage

increases. For the last 5 seconds of the traverse, the wheel compression is reduced and higher soil shearing is observed.

In Figures 4.9 and 4.10 most of the detectable flow is observed at the back-end and front-end of the wheel where the grousers enter and exit the simulant. In these conditions, the region directly beneath the wheel, where a significant velocity is detected, the soil flow direction indicates that the soil is being compressed. Conversely at 70% slip the soil motion happens more drastically and at a higher depth, where the significant amount of soil moves opposite the direction of the wheel traverse (yellow regions illustrate the motion to the right on the flow direction segment of the visualization) and a small region of soil is pressed at the front-end of the wheel.

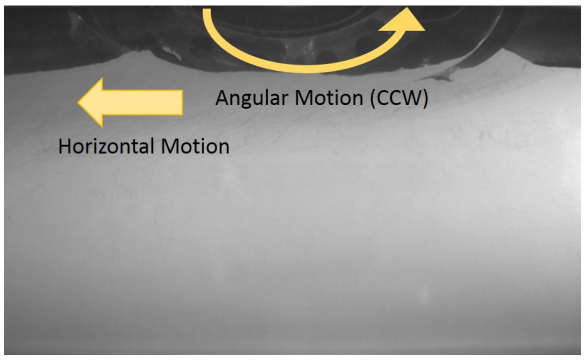

Figure 4.8: Wheel horizontal and angular rotation

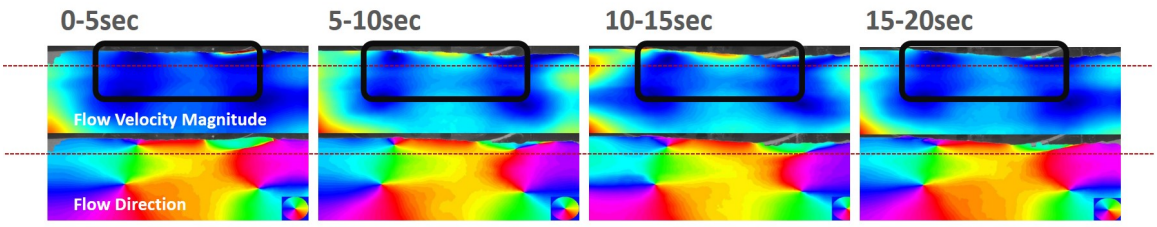

Figure 4.9: Slip 20% OGE, 164 N Wheel Loading

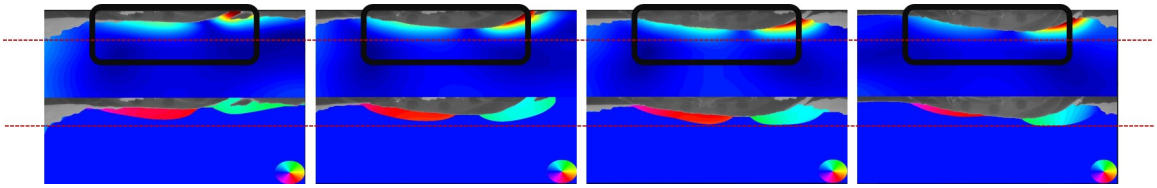

Figure 4.10: Slip 40% OGE, 164 N Wheel Loading

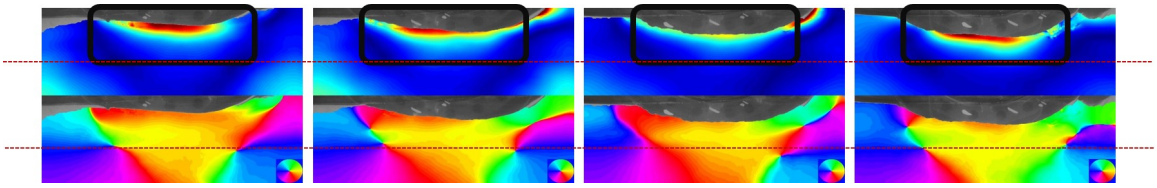

Figure 4.11: Slip 70% OGE, 164 N Wheel Loading

Figure 4.12 compares soil motion at the 30% slip condition at low and high wheel loading (164 N & 225 N, respectively) in OGE. There is no obvious significant difference in the depth, magnitude, and direction of the soil motion even though terramechanical results show a significant increase in sinkage at the higher loading.

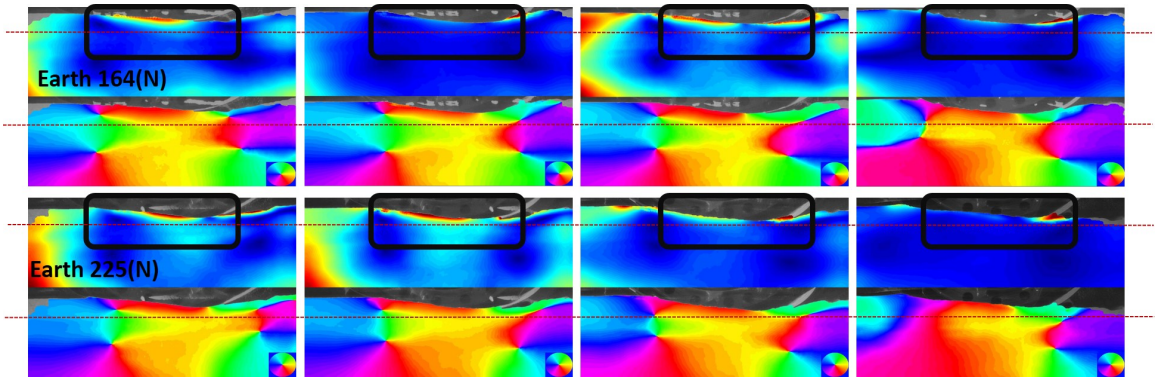

Figure 4.12: Slip 30% OGE, 164 & 225 N Wheel Loading

4.2 Partial Gravity Experimental Campaign

The key objective of this study is to investigate the mobility performance of the Exo-Mars wheel in partial gravity while it travels forward on leveled terrains. This section describes details of the partial gravity experiments and presents terramechanics and optical flow results.

4.2.1 Reduced-gravity Flights Test Cases & Conditions

The experimental setup described in Chapter 3 flew aboard Canada's National Research Council's (NRC) Falcon 20 aircraft. As shown in Figure 4.13, to simulate partial gravity, the aircraft produces ascent and decent flight maneuvers. During each parabola, a partial gravity environment is maintained for approximately 20-30 seconds between two 2-g maneuvers. During the flight, three components of acceleration, longitudinal (Ax), lateral (Ay), and vertical (Az) were measured with an IMU fixed inside the plane. These Figures show that accelerations in lateral and longitudinal directions are almost zero during partial gravity, indicating that it is unnecessary to take the effects of the gravity on other directions into consideration. In total, 10 Martian-g parabolas and 7 Lunar-g parabolas were flown with the wheel testing apparatus.

4.2.2 PGE Terramechanics Results

In this campaign, wheel slip is controlled by controlling the speed of the horizontal axis and wheel angular velocity. Wheel sinkage is a function of slip (i.e. dynamic slip-sinkage) and can also vary or develop over time. Therefore since sinkage and slip are interdependent, it is crucial to isolate the parameters and characterize the effect individually, specifically in the low gravity environment.

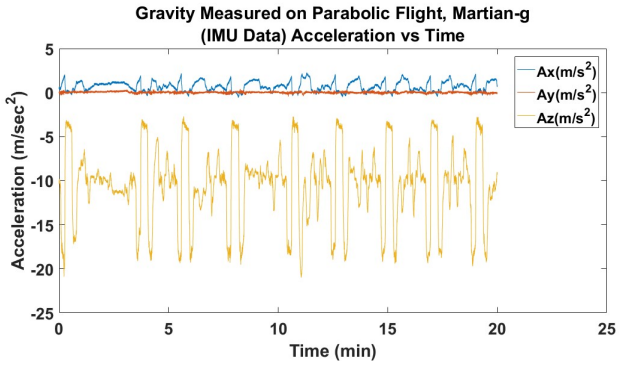

(a) Simulated Martian-g

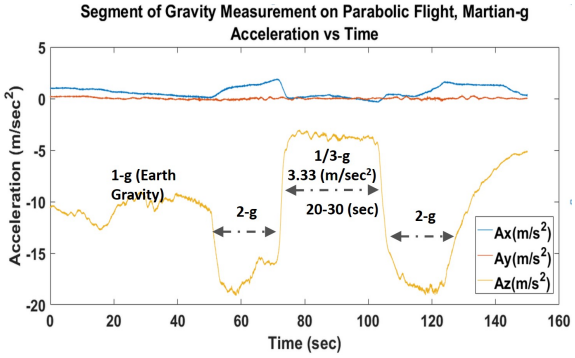

(b) A segment of simulated Martian-g

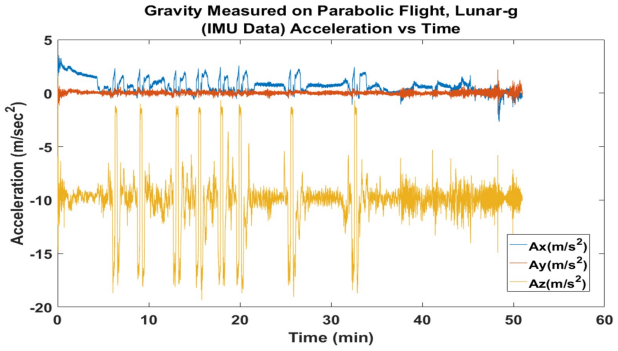

(c) Simulated Lunar-g

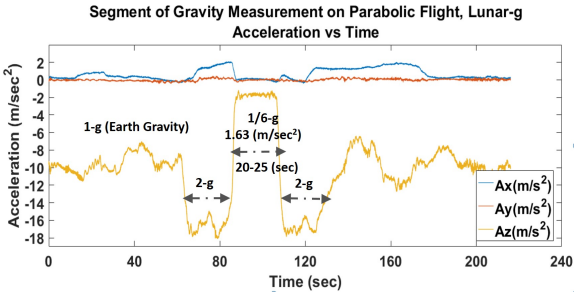

(d) A segment of simulated Lunar-g

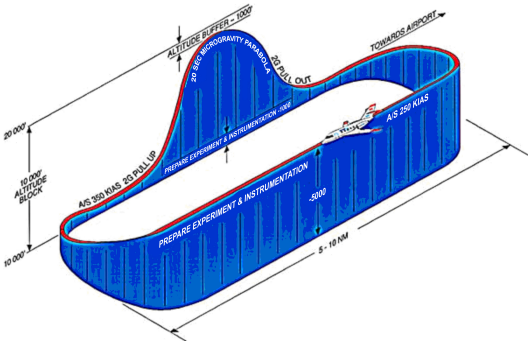

(e) A parabolic manoeuvre

Figure 4.13: Parabolic flights:(a) Martian-g flight with zoom-in (b) on one parabola; (c) Lunar-g flight with zoom-in (d) on one parabola (e) Partial gravity flight trajectory including a reduced-g parabola as well as an experiment and instrumentation preparation phase between parabolas

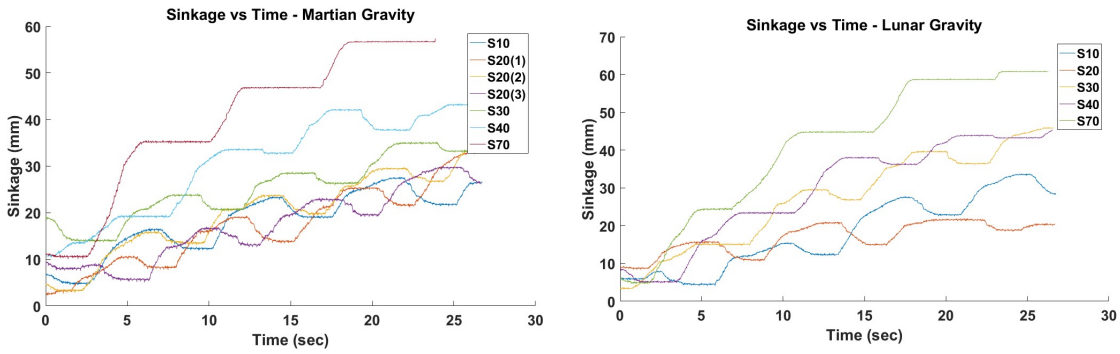

(a) Sinkage in Martian gravity

(b) Sinkage in Lunar gravity

Figure 4.14: Raw Sinkage data collected in partial gravity for slip 10%-70% (a) Sinkage vs time for Martian-g, (three sets of 20% slip is taken in Martian gravity) (b) Sinkage vs time for Lunar-g (two sets of 20% slip is taken in Lunar gravity)

Figure 4.14a & 4.14b present raw sinkage data in Martian and Lunar gravities with controlled slip, where the sinkage increases, sometimes reaching steady state condition. There is a limitation of 100 mm maximum sinkage sensor reading on the existing setup, which was never reached. The duration of simulated partial gravity is between 20 to 30 seconds, therefore data collected in PGE and OGE considered this duration for comparability and consistency. Data was sampled at a frequency of 718 Hz for all slip (except 70% slip, which is recorded at 642 Hz due to a limitation encountered in the controller's communication protocol).

Figure 4.15a and Figure 4.15b summarize the effect of slip on sinkage in Martian gravity. Figure 4.16a and Figure 4.16b summarize the effect of slip on sinkage in Lunar gravity. The higher the slip rate, the larger the magnitude of both average and maximum sinkage, with this trend observed in both Lunar and Martian gravity. The standard deviation of the average and maximum sinkage (three datasets), at 20% slip rate, is 1.5 mm and 2.4 mm respectively in Martian gravity. This relatively small deviation shows the effectiveness of soil preparation as well as the repeatability of the experiment. However, Lunar sinkage data presented relatively higher uncertainty; 2-3 times higher than Martian gravity, that can be attributed to the lower gravity

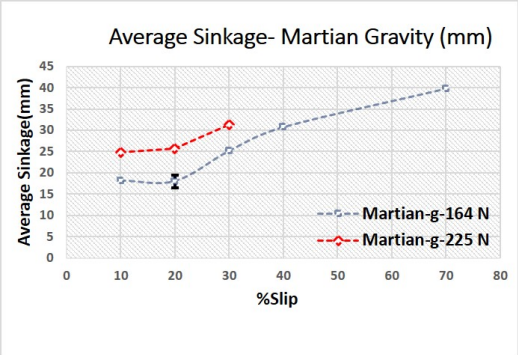

(a) Average Sinkage vs %Slip

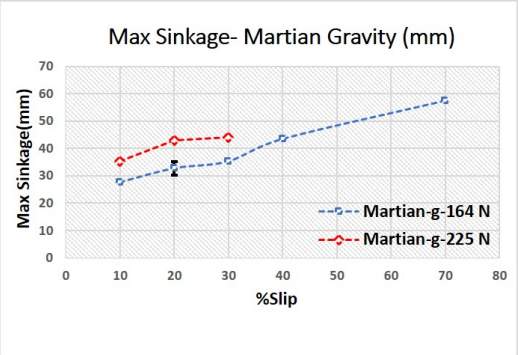

(b) Max Sinkage vs %Slip

Figure 4.15: Martian sinkage data (a)Average of sinkage at 164 & 225 N wheel loading, slip 10-70% (b)Max of sinkage at 164 & 225 N wheel loading, slip 10-70%

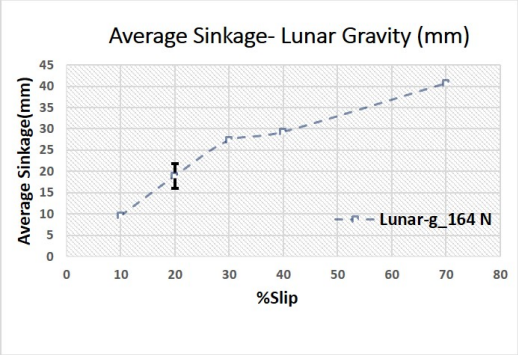

(a) Average Sinkage vs %slip

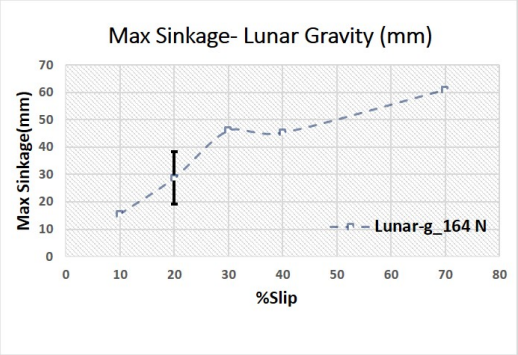

(b) Max Sinkage vs %slip

Figure 4.16: Lunar sinkage data (a)Average of sinkage at 164 N wheel loading, slip 10-70% (b)Max of sinkage at 164 N wheel loading, slip 10-70%

environment and its effect on the soil. Another source of greater error is the fact that out of three data collected only 2 of them are considered due to a timing fault that occurred in the 3rd. In Martian gravity altering the loading on the wheel from 164 N to 225 N increased the sinkage by 25-35 %. Figures 4.17a and 4.17b compare sinkage in both Martian and Lunar gravity. It was hypothesized that the wheel traveling in lower gravity (Lunar) would experience higher sinkage. However, the experimental data demonstrates that gravity is not the dominant factor on the sinkage parameter (with identical wheel loading) once in partial gravity, comparing Martian to Lunar.

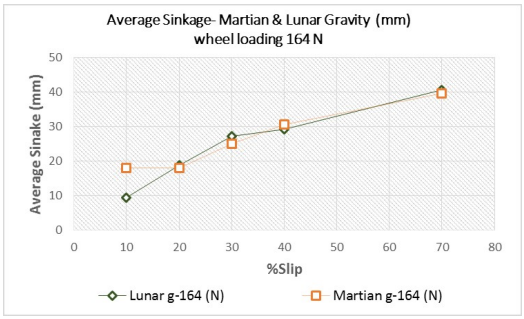

(a) Lunar & Martian Average Sinkage vs %slip at 164 N wheel loading

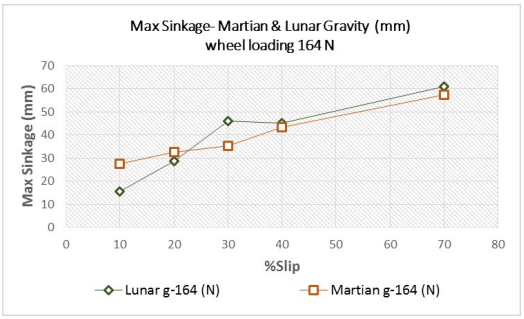

(b) Lunar & Martian Max Sinkage vs %slip at 164 N wheel loading

Figure 4.17: Comparing the gravity effect on Sinkage at each slip rate (a)Average of sinkage at 164 N wheel loading, slip 10-70% (b)Max of sinkage at 164 N wheel loading, slip 10-70%

Figure 4.18 and Figure 4.19 illustrate the behavior of DP as a function of time through 20-30 seconds of travel in Martian and Lunar gravity. The peaks are more distinct at lower slip rates (below 40% slip). The patterns are also more discernible and periodic in Martian gravity than in Lunar gravity. For each test case, three periods of the recurring pattern are extracted and the average is considered for assessment.

Figure 4.20 shows that in general the drawbar pull increases with slip ratio. This behavior can be explained as an increase in soil shear stress due to the increase of the slip ratio; a larger deformation in soil develops a larger thrust as shown in equation (3.2). DP can thus increase at higher slip, as long as thrust increases more than resistance does.

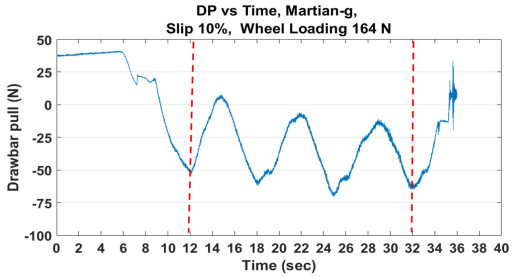

(a) DP vs time, slip 10% wheel loading 164 N

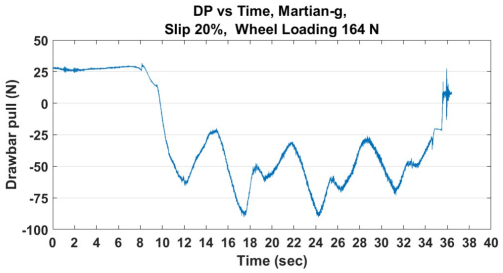

(b) DP vs time, slip 20% wheel loading 164 N

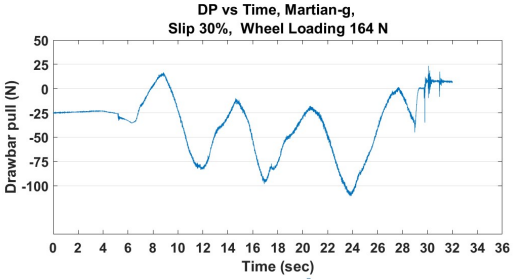

(c) DP vs time, slip 30% wheel loading 164 N

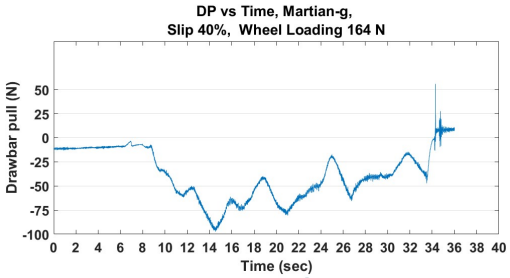

(d) DP vs time, slip 40% wheel loading 164 N

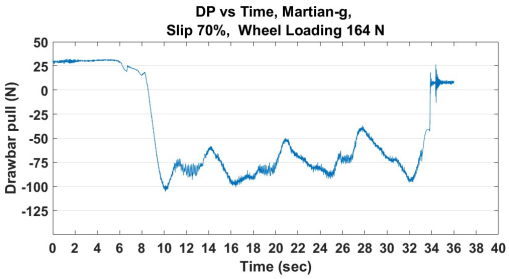

(e) DP vs time, slip 70% wheel loading 164 N

Figure 4.18: Drawbar pull over 20-30 seconds of Martian gravity at different slip ratio, with 3 periods of recurring pattern highlighted

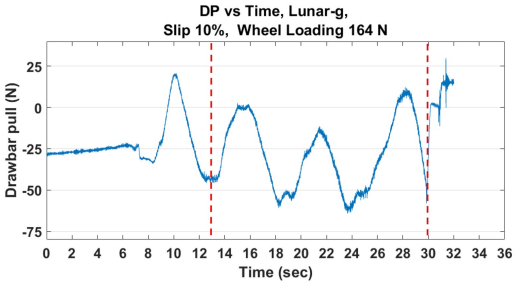

(a) DP vs time, slip 10% wheel loading 164 N

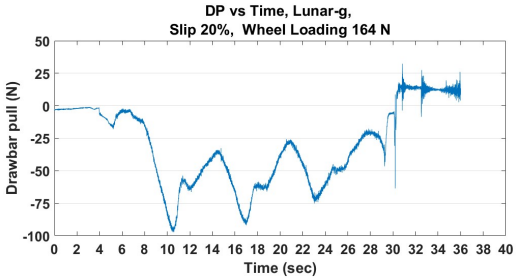

(b) DP vs time, slip 20% wheel loading 164 N

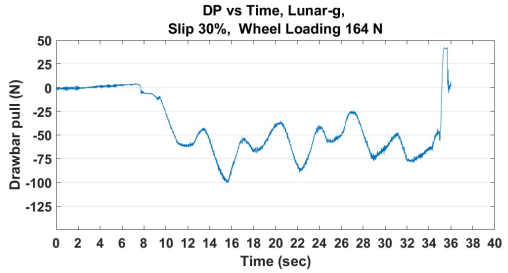

(c) DP vs time, slip 30% wheel loading 164 N

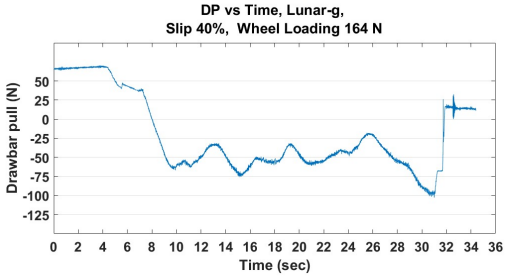

(d) DP vs time, slip 40% wheel loading 164 N

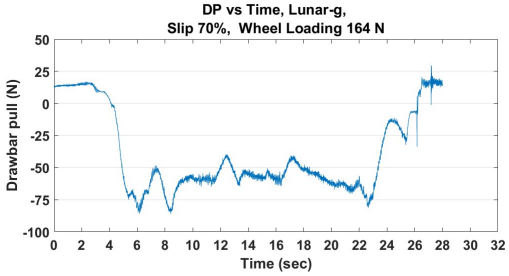

(e) DP vs time, slip 70% wheel loading 164 N

Figure 4.19: Drawbar pull over 20-30 seconds of Lunar gravity at different slip ratio, with 3 periods of recurring pattern highlighted

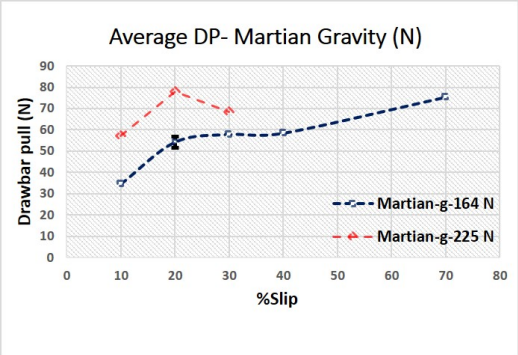

(a) Average DP vs %slip, Martian-g

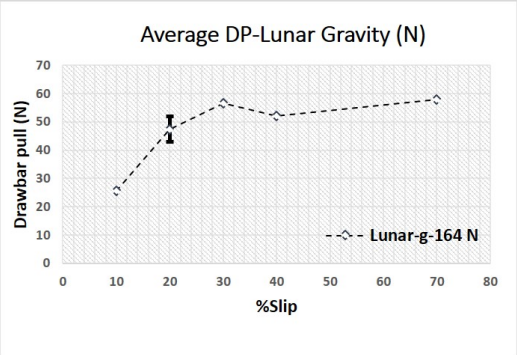

(b) Average DP vs %slip, Lunar-g

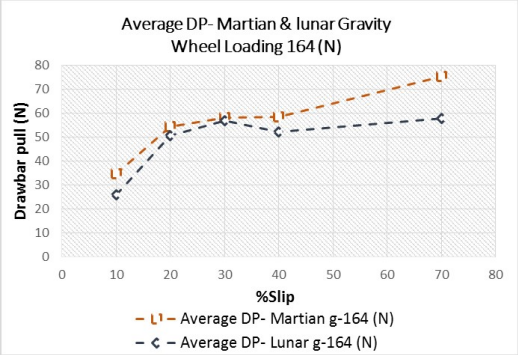

(c) Average DP vs %slip, at 164 N wheel loading

Figure 4.20: DP data (a) Average of DP at 164 & 225 N wheel loading, slip 10-70% (b) Average of DP at 164 N wheel loading, slip 10-70% (c)

The ExoMars wheel is subjected to drawbar pull testing in Martian gravity at 164 and 225 N wheel loading (Figure 4.20a). With increasing load, the thrust grew faster than rolling resistance resulted in an increase of 20-60% in the generated drawbar pull (depending on the slip rate).

There is a large increase in DP when slip changes from 10% to 20%. This observation is consistent for both Lunar and Martian gravity, and for both wheel loadings in Martian gravity. Since there was no major difference in sinkage hence the rolling resistance of the wheel, the higher developed drawbar pull is attributed to greater thrust development.

Between 20% and 40% slip there is generally little to no additional increase in DP (and for 225 N wheel loading in Martian-g there is a drop). In Martian gravity, there

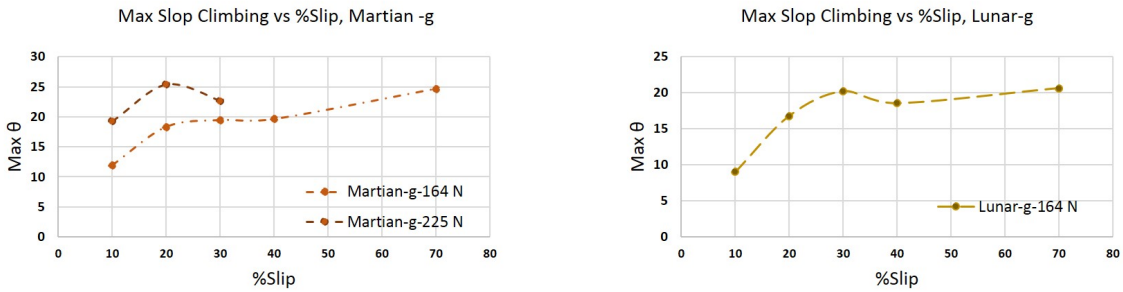

(a) Max slope vs %slip, Martian-g

(b) Max slope vs %slip, Lunar-g

Figure 4.21: Climbing slope of ExoMars wheel in Partial gravity (a) Ability of the rover to climb slopes at 164 & 225 N wheel loading, slip 10-70% in Martian-g (b) Ability of the rover to climb slopes at 164 N wheel loading, slip 10-70% in Lunar-g

is another substantial increase in DP between 40% and 70% slip. The DP measured in PGE at equal wheel loading (164 N) appears to be always at least slightly higher in Martian-g than Lunar-g, and is as much as 25% higher, at 70% slip.

When a rover wheel climbs a slope of angle θ, the wheel's drawbar pull has to overcome the traction load of $Wtan(\theta)$ in order to climb up, as shown in Figure 3.5b. The traction load increases along with slope angle. Thus, the slope climbing ability is directly defined by estimating slope angle θ, in which the drawbar pulls are equal to the traction load at each slip ratio.

Based on the DP versus slip trend, it is expected to have a possibility of the traverse at higher inclination since higher slip presented improved traction. This experiment also confirms the effect of gravity on traction and therefore lesser ability of the rover to climb the higher slope (Figure 4.21a and 4.21b). These data suggest that reducing the gravity introduce potential challenges for the rover climbing at the slope higher than 20°.

4.2.3 PGE Optical Flow Results

This section examines the effects of gravity, slip and wheel loading on soil motion in PGE.

Figure 4.22 through Figure 4.24 show the optical flow analysis for the tests at 20%, 40%, 70% slip in Martian gravity at 164 N wheel loading. Each figure depicts four 5-second averages of soil flow (out of approximately 25 seconds total traverse). The detail on how to interpret the figures is presented in Section 4.1.2. In the directional flow field, green, red, and yellow colormaps demonstrate upward, downward, and rearward (opposite to the horizontal motion of the rover wheel) soil motion, respectively.

At 20% slip, the soil flow magnitude changes substantially with respect to time. Figure 4.22 shows the gradual development of soil mobilization with time at low slip. In Figure 4.23 and Figure 4.24, there is a little variation in the soil flow results between the time segments. It appears at slip value above 20% the high magnitude of soil flow is developed from the start of the whee-soil interaction. The images are normalized based on the rim speed, with higher rim speed corresponding to higher slip. For example, the absolute (non-normalized) velocities are actually much higher for 70% slip compared to 40% or 20% slip.

There are two regions in the soil flow results in Martian gravity; a region where soil flows rearward which is developed directly beneath the wheel (the soil shearing occurs opposite the direction of the rover traverse) and a region where soil flows upward, at the rear-end of the wheel. There is a little variation in the direction of mobilized soil with respect to slip value. There is an indication that at lower slip there are more compressed regions in the soil, and that the observed compression is time-dependent. (see directional flow fields in Figure 4.22 through Figure 4.24).

Figure 4.25 suggests that the effect of wheel loading on the soil mobilization is not significant in Martian gravity. At 30% slip in Martian gravity, the increase of

normal load doesn't seem to influence the depth, magnitude, and direction of the soil motion, even though in the terramechanical results a significant increase in sinkage is observed for the higher loading.

Analysis of the wheel-terrain interaction in Lunar gravity shows similar trends to those of the Martian gravity experiments. As the wheel traverses forward in time the regions of mobilized soil become larger and the magnitude of velocity fields increase. In addition, an increase in the slip raises the extent of motion in the soil. (Figures 4.26-4.28)

The comparison between optical flow results in Martian and Lunar gravity indicates that there is a greater region of soil mobilized in Lunar gravity than Martian gravity. At lower gravity, not only the magnitude of the velocity field increases but also the direction of the flow is influenced. A contrast is observed between Lunar and Martian gravity's flow fields at slip above 40% wherein Lunar gravity the soil beneath the wheel flows backward at the greater extent while in Martian gravity the soil experienced compression at the contact patch. This dissimilarity is further distinguishable between Figure 4.24 and Figure 4.28. The results are in agreement with the motor current data in Lunar gravity where the current draw is much less at the same sinkage level.

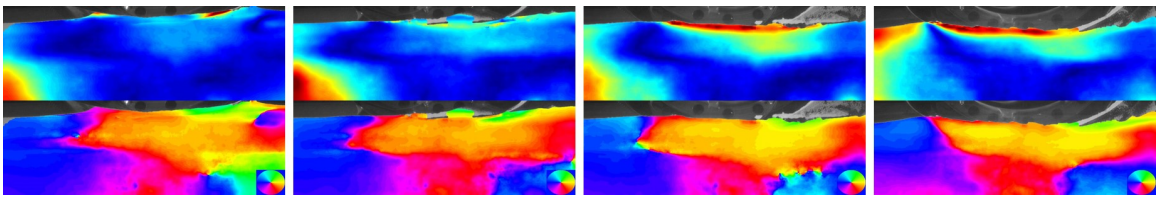

Figure 4.22: Slip 20% Martian, 164 N Wheel Loading

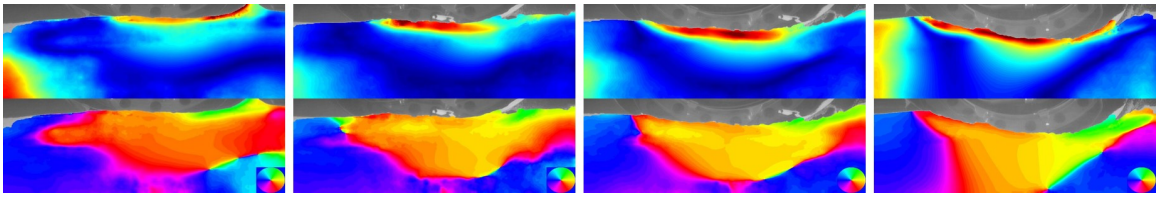

Figure 4.23: Slip 40% Martian, 164 N Wheel Loading

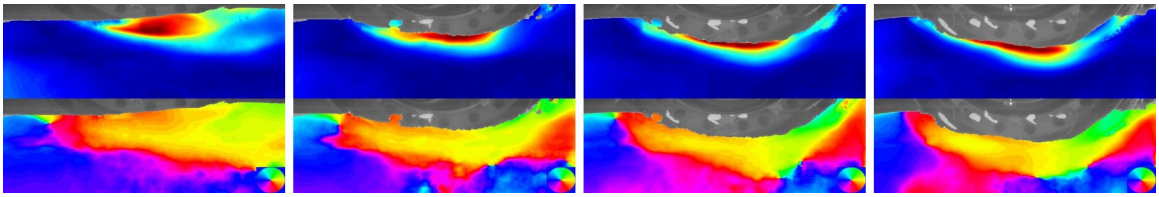

Figure 4.24: Slip 70% Martian, 164 N Wheel Loading

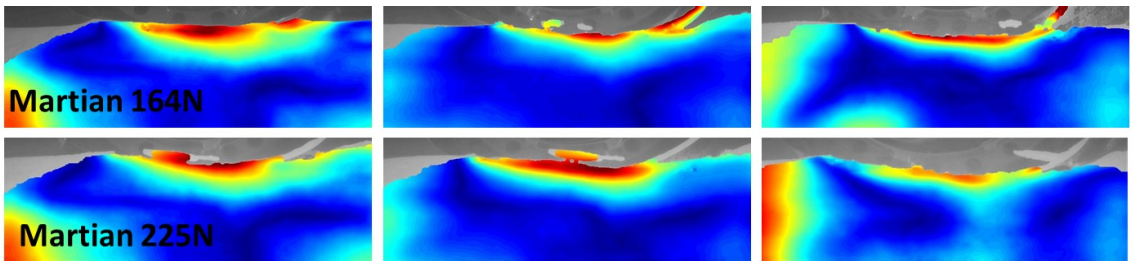

Figure 4.25: Influence of wheel loading on soil mobilization in Martian-g at 30%slip

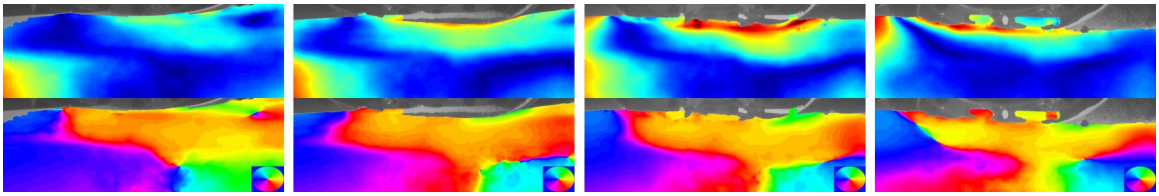

Figure 4.26: Slip 20% Lunar, 164 N Wheel Loading

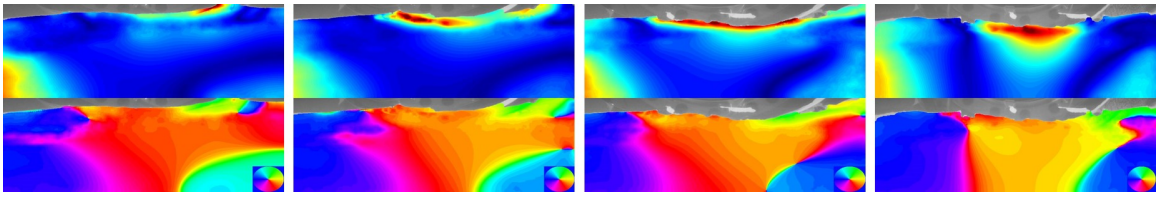

Figure 4.27: Slip 40% Lunar, 164 N Wheel Loading

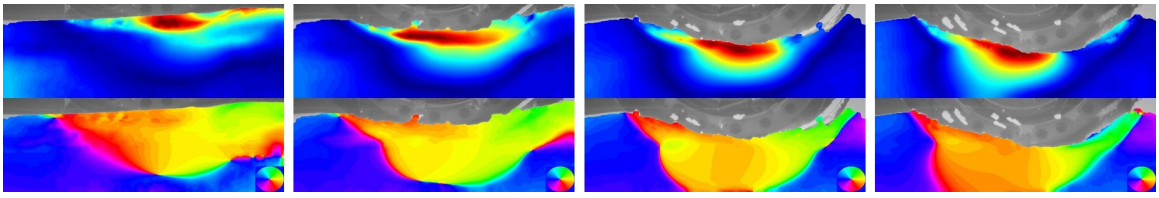

Figure 4.28: Slip 70% Lunar, 164 N Wheel Loading

The failure patterns of soil under the driving wheel are complex. It can be seen from Figures above that the flow patterns in the longitudinal and vertical direction depend on time, wheel slip, and gravitational level.

4.2.4 Comparison of PGE & OGE Terramechanics analysis

It is important to understand the effect of gravity on DP. Figure 4.29a shows that DP is 15%-35% lower (depending on slip value) in Martian gravity compared to OGE, at the same wheel loading. DP in Lunar gravity is 15%-50% lower than OGE, at the same wheel loading. This shows that testing at equal wheel loading is not enough to replicate traction that will be experienced by planetary rovers in partial gravity. DP at lower slip rates seems to follow the same trend in both Martian and Lunar gravities (except at 10% slip where there is 20% difference). However, at higher slip rates (slip percentage $>$ 40%) DP tends to increase and differs by 2% to 25% in Martian gravity compared to Lunar gravity.

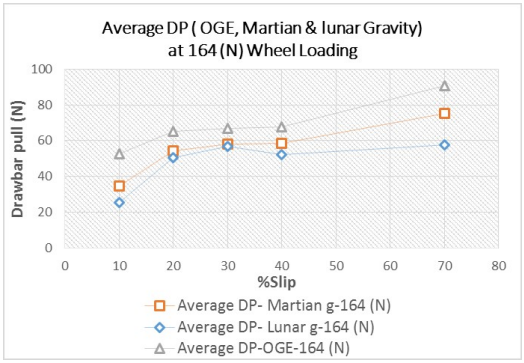

(a) DP Data, OGE & PGE at 164 (N) wheel loading

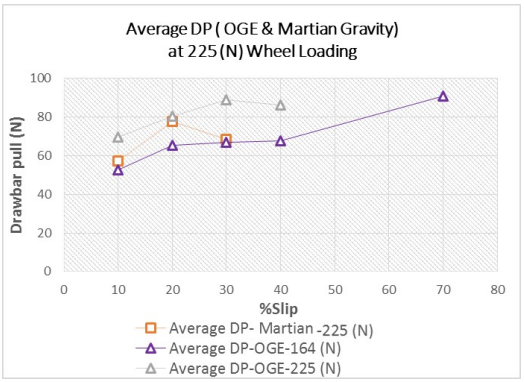

(b) DP Data, OGE & PGE at 225 (N) wheel loading

Figure 4.29: Drawbar pull data comparison of OGE & PGE, DP is consistently reduced in lower gravity, with equal wheel loading applied. (a) At 164 N wheel loading, Martian DP is lower than OGE, and Lunar is at times lower still. (b) At 225 N, Martian-g DP is generally below OGE.

Martian gravity is approximately 1/3 of Earth gravity, and lunar gravity is about 1/2 of Martian gravity (and thus 1/6 of Earth gravity). It is clear from Figure 4.29 that DP is neither independent of nor linearly proportional to gravity. Comparing the change in DP value from lunar to Martian with the change from Martian to Earth at slip ratios less than 40%, it doesn't appear to linearly correspond to the gravitational ratio of Lunar/Martian and Martian/Earth. However, this comparison maps the DP with respect to the gravitational ratio at higher slip ratio such as 70% (Figure 4.29a). These data provide evidence that once the gravity is lower than Earth's gravity the traction of the rover is impaired.

Experimental cases at low and high wheel loads (164 N for 'Low' and 225 N for 'High') were performed for both Martian gravity and OGE to observe the effect of higher wheel loading on the DP (see Figure 4.30). Increasing the wheel loading in Martian gravity by 37% increased the DP 14% to 60%, depending on the slip rate. While the same increase in wheel loading during OGE leads to a 20% to 30% increase in DP. Comparing DP results of the OGE cases where wheel loading is 37% less than the PGE leads to similar trends and closely approximates the PGE results.

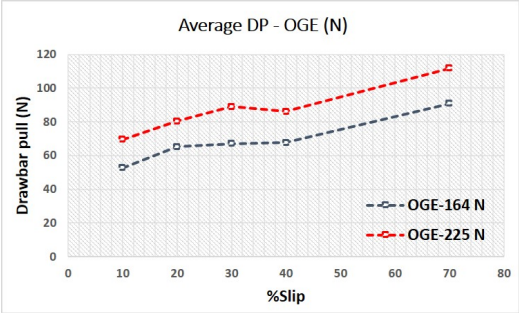

(a) DP vs %slip at different wheel loading, OGE

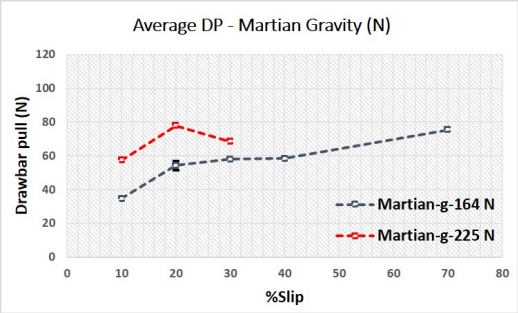

(b) DP vs %slip at different wheel loading, Martian-g

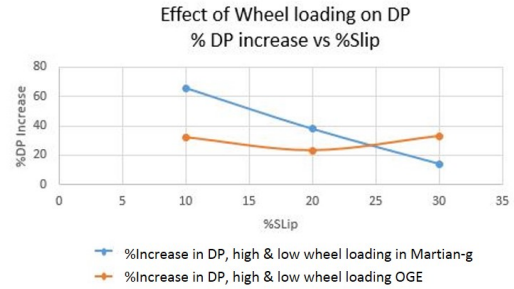

(c) % Increase in DP vs %slip, comparison of OGE & Martian-g

Figure 4.30: DP comparison of OGE & Martian gravity, (a) The effect of wheel loading on DP in 1-g (b) The effect of wheel loading on DP in Martian-g (c) The % increase in DP as a result of wheel loading in OGE and Martian-g

Consequently, these data point out that when studying and modeling partial gravity DP on Earth, wheel loading could perhaps be decreased by 30% to 40% for more comparable and accurate results.

As discussed in Section 3.1.3, Figure 4.31 shows the slope climbing ability at each slip as the mobility of the rover is reduced in partial gravity.

Figure 4.32a to Figure 4.32c illustrate the sinkage parameters vs slip profile on Martian and Lunar gravities at different wheel loading and draw a parallel with the results of OGE. Data collected in partial gravities indicates that ExoMars wheel's sinkage values (both average and maximum sinkage) follow the same trend with similar values at the same wheel loading in both Martian and Lunar gravity (Figure 4.32a & 4.32c). As the slip value is increased, maximum and average sinkage increase similarly in both gravities. However, at the same wheel loading in PGE the wheel

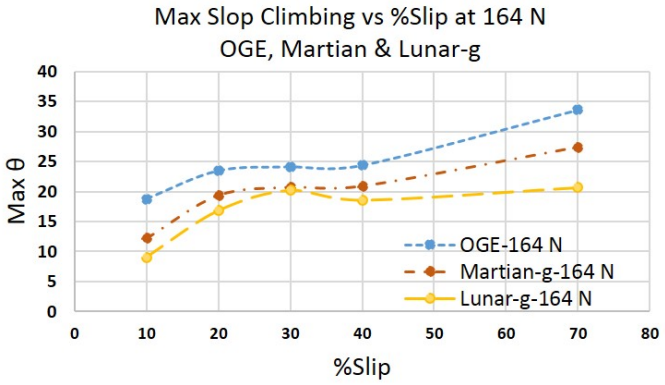

Figure 4.31: Ability of the rover to climb slopes at 164 N wheel loading, slip 10-70% in Partial gravity and OGE

experienced about 25% more sinkage in comparison with OGE. Another interesting observation is that increasing the wheel loading 37% in OGE, compared to PGE, results in analogous measured sinkages for all slip rates. For identical wheel loading, the sinkage is not the same on an extraterrestrial surface having lower gravity than Earth's surface, which illustrates the influence of gravity on the soil bearing capacity and shearing characteristics originated by the variation in soil parameters and internal stresses.

Higher sinkage values are observed in Martian gravity compared to OGE at both the higher and lower levels of wheel loading. However, the percent increase in the sinkage value is much higher in OGE compared to Martian gravity when increasing the wheel loading (Figure 4.33a through Figure 4.33c).

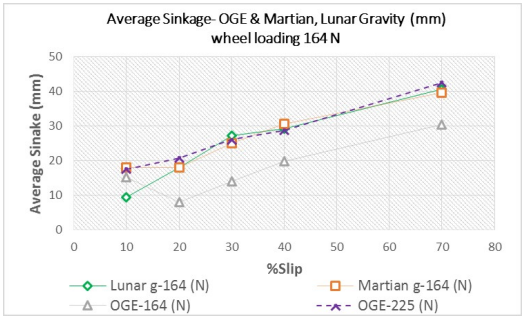

(a) Average sinkage, OGE & PGE at different wheel loading

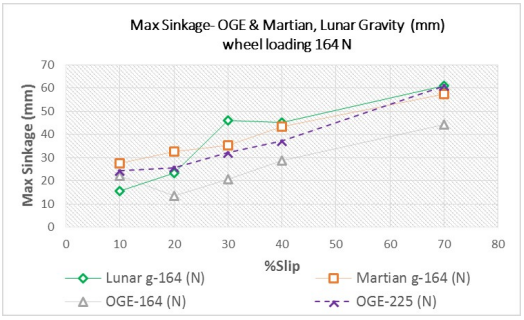

(b) Max sinkage, OGE & PGE at different wheel loading

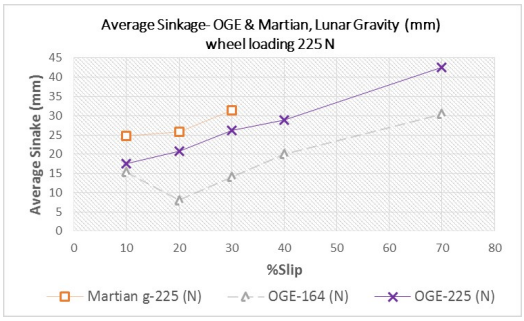

(c) Average sinkage, OGE & Martian gravity at 225 (N) wheel loading

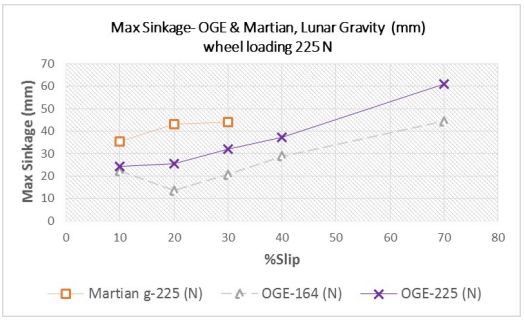

(d) Max sinkage, OGE & Martian gravity at 225 (N) wheel loading

Figure 4.32: Sinkage data comparison of OGE & PGE, (a) & (b) demonstrate the congruence of the partial gravity sinkage at lower wheel loading with the 1-g sinkage data at higher wheel loading, (c) & (d) show higher sinkage in Martian-g than OGE, at higher wheel loading

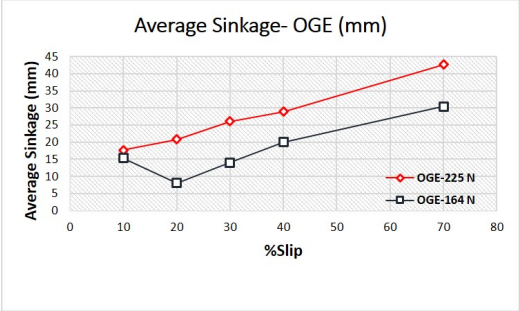

(a) Sinkage vs %slip at different wheel loading, OGE

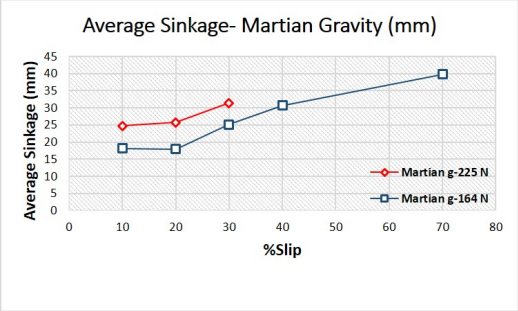

(b) Sinkage vs %slip at different wheel loading, Martian-g

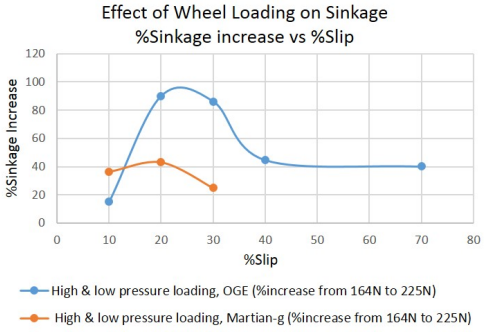

(c) % Increase in sinkage vs %slip, comparison of OGE & Martian-g

Figure 4.33: Sinkage data comparison of OGE & Martian gravity, (a) illustrate the effect of wheel loading on sinkage in 1-g (b) illustrate the effect of wheel loading on sinkage in Martian-g (c) demonstrate the % increase in sinkage as a result of wheel loading in OGE and Martian-g

These comparisons reveal different trends between OGE and PGE in terms of sinkage parameters, while a similar trend is seen between 1/6-g and 1/3-g. The data indicates that when testing on Earth, wheel loading could be increased by 30% to 40% for perhaps more comparable and accurate results, particularly for higher slip rates.

The average current draw from the wheel motor, shown in Figure 4.34 for different gravities and different slip ratios, follows similar trends to the DP data at the same conditions (compare to Figure 4.29a). This is consistent with a situation with low resistance acting on the wheel. In equation (3.2), if we set $R = 0$ then $DP = T$, and in this case we would expect the thrust (T, and hence also DP) to be proportional to wheel torque (and hence current). Recall from Chapter 1 that thrust is a function of soil strength and slip. Figure 4.34 presents lower thrust in the lower gravity at the same slip, particularly at %70 slip.

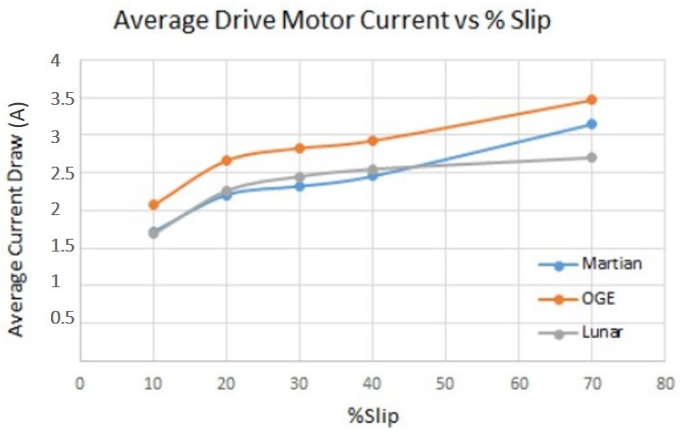

Figure 4.34: Average current draw from wheel motor vs %slip at 164 N wheel loading

4.2.5 Validation of the Visualization Output Data

The optical flow estimated flow fields are in the camera reference frame, and by subtracting the camera motion from the horizontal flow the reference frame will be transformed to a frame that is static relative to the sandbox. To estimate the camera

motion, the median horizontal component of the flow field is considered and referred to as U_{static}.

One of the cross-validations used during the analysis is comparing the estimated camera motion with that measured by the horizontal axis encoder, to ensure agreement. At a specific slip, the actual horizontal motion of the camera is calculated to compare with the estimation of the output flow field on each gravity condition (see Table 4.1). The estimated error is usually under 5% and never over 11.4% (Table 4.2).

TABLE 4.1: U_{static} (MOTION OF THE CAMERA) EXTRACTED FROM THE ANALYSIS, (IN UNITS OF FPS)

Slip	**70%**	**40%**	**20%**
Actual	2.2	4.06	5.6
Earth	2.15	4.25	5.8
Martian	1.95	3.66	5.4
Lunar	2.24	3.78	5.15

TABLE 4.2: PERCENT ERROR OF U_{static} EXTRACTED FROM THE ANALYSIS

Slip	**70%**	**40%**	**20%**
Earth	2.27%	4.68%	3.57%
Martian	11.36%	9.85%	3.57%
Lunar	1.82%	6.9%	8.04%

4.2.6 Comparison of PGE & OGE Optical Flow Analysis

As mentioned in the section 4.1.2, the rolling wheel is driving counterclockwise and the rover traverses from right to left of the image. In each figure (Figure 4.35 through Figure 4.37), each row shows data from either Earth, Martian, or Lunar gravity, while each column shows the average soil motion over a 5-second segment of the time-span. The time-span is segmented to capture time-varying phenomena. For example, wheel sinkage varies with time, especially at higher slip in partial gravity (inspect across

Figure 4.37); note that this corresponds to the sinkage vs time as already seen in Figure 4.14a and Figure 4.14b.

Inspecting down any of the columns in the figures shows the influence of gravity on soil motion. It is clear that at any time, and at any slip rate, there is more soil motion in partial gravity (Martian and/or Lunar) than in Earth gravity. Figure 4.35 through 4.37 present a contrast in the soil motion at different gravities and indicates an increase in depth and magnitude of the soil motion as the gravity reduces. Further, especially at 70% slip, there is notably more soil motion in Lunar gravity than in Martian gravity. It is interesting to compare these results to the DP plot in Figure 4.29a, which shows lower DP in partial gravity at all slips, and lower DP in Lunar gravity than Martian gravity at 70% slip.

Increase in the slip impacts the soil motion in Lunar and Martian gravities much greater than in OGE, as shown in Figure 4.35 and 4.36. On Earth an increase from 20% to 40% slip results in the development of a relatively small region of soil motion in the front and back-end of the wheel whereas in Martian and Lunar gravities there is a significant increase in the magnitude of the soil motion below the wheel-soil interface. This observation can only be explained by the effect of gravity on the soil behavior.

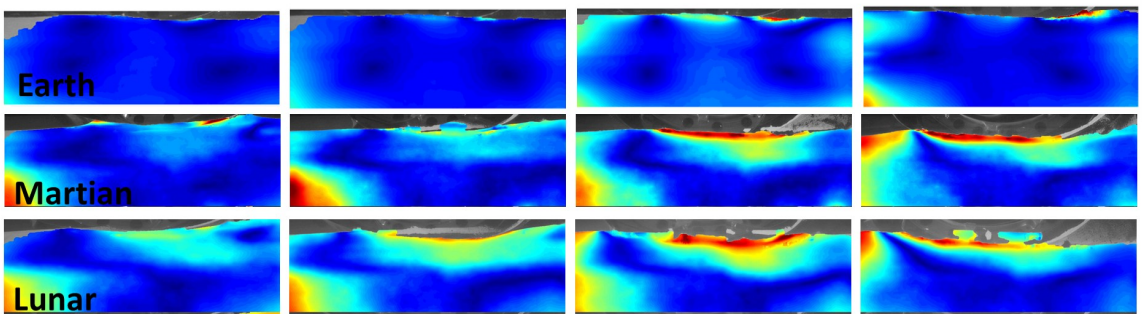

Figure 4.35: Comparison of wheel-terrain interaction on Earth, Martian & Lunar gravity at slip 20% wheel loading 164 N

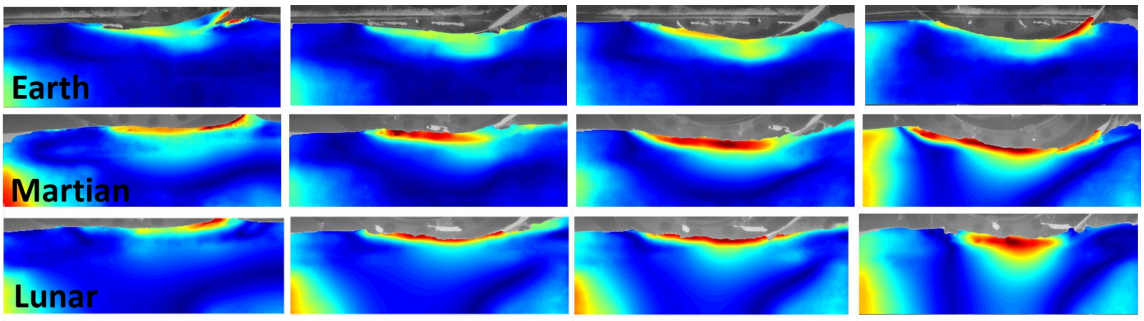

Figure 4.36: Comparison of wheel-terrain interaction on Earth, Martian & Lunar gravity at slip 40% wheel loading 164 N

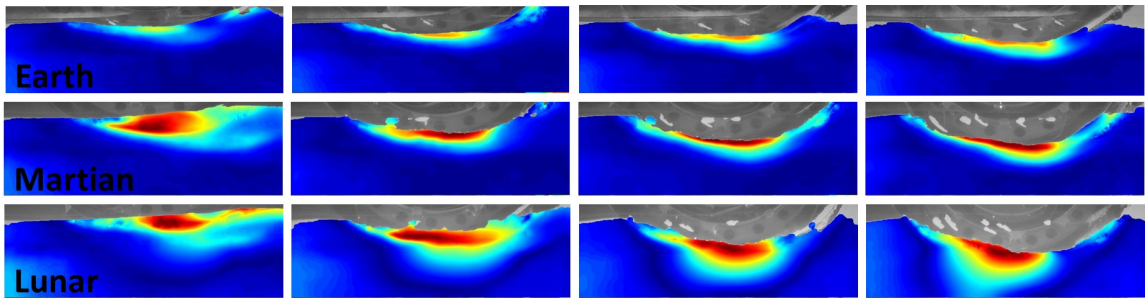

Figure 4.37: Comparison of wheel-terrain interaction on Earth, Martian & Lunar gravity at slip 70% wheel loading 164 N

Another observation is that in both Earth and Martian gravities increasing the wheel loading from 164 N to 225 N doesn't significantly impact the soil mobilization; Figure 4.38 and Figure 4.39 illustrate the effect of this variation at 30% slip. From the figures, it is clear that the influence of gravity on the soil mobilization is much more prominent than the influence of the normal force. This may be related to the flexible wheel's large contact patch distributing the normal load and possibly diminishing the effect.

Maximum velocity magnitude of the soil in PGE are close to the rim speed but in OGE are significantly lower. It is hypothesized that in PGE the thin layer of soil between the deformable rim and the glass is mobilized by the wheel-soil interactions much more than it is in OGE. The regions of mobilized soil in PGE also are substantially larger than OGE.

In summary, gravity has a significant effect on the wheel-soil interaction at equal slip and wheel loading. Moreover, under the influence of lower gravity, these interactions are more sensitive to slip than in Earth gravity. Soil mobilization appears to increase more with respect to time and with respect to increasing slip in partial gravity compared to in Earth gravity. In Earth gravity the magnitude/depth of soil motion is small, and any changes in slip and wheel loading do not have obvious impact on the soil behavior. Recall that the wheel loading is the same for all tests in Figures 4.35 through 4.37, so the gravity acting on the soil is the only variable changed between the tests in Earth, Martian, or Lunar gravity in any given figure. Further, in both Martian and Earth gravities increase in wheel loading does not appear to have a significant effect on soil mobilization. From these results, it appears that the lower gravity reduces soil strength enough to induce more soil motion and lower drawbar pull.

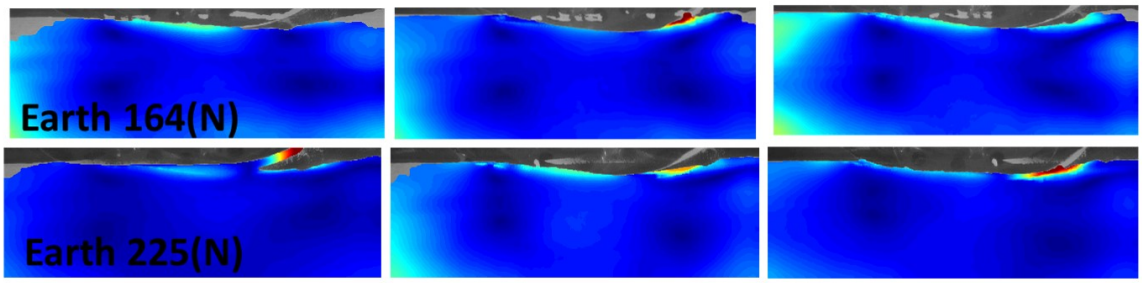

Figure 4.38: Effect of wheel loading on wheel-terrain interaction on Earth gravity at slip 30% wheel loading 164 N and 225 N

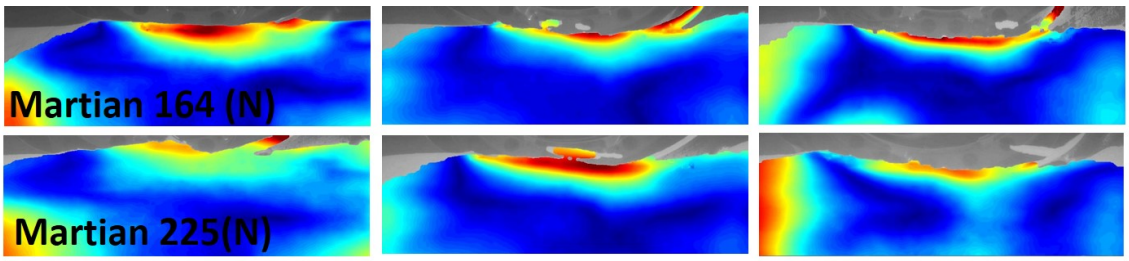

Figure 4.39: Effect of wheel loading on wheel-terrain interaction on Martian gravity at slip 30%, wheel loading 164 N and 225 N

Chapter 5

Conclusion & future work

5.1 Conclusions

This thesis investigates the mobility of the ExoMars rover wheel in low gravity environments. It studies the effects of gravity, wheel loading, and slip on traction and sinkage. Controlling the wheel slip and normal load ensures that the only difference between experiments is the effect of gravity on the soil particles themselves. It is important to consider that these differences between experiments are equivalent to the difference between actually driving a rover on Mars and testing a reduced-mass version of the rover (i.e. with equal wheel normal load) in similar soil on Earth.

When evaluating the rover performance on Earth it is a common practice to reduce the mass of the rover to 1/3 in order to adjust for the effect of reduction in gravity on Mars and thus test with equal wheel loading. However, this work reveals important differences in performance when wheel loading is equal but gravity and thus its effect on the soil itself is different.

This work is the first to directly observe rover wheel-soil interactions in reduced gravity, aboard parabolic flights achieving Martian and Lunar gravitational accelerations. An ExoMars rover prototype wheel is operated against a glass window along

the side of a sandbox, and the interactions are visualized using an optical flow-based technique. Results are compared to the experiments conducted in Earth gravity.

The study illustrates that Drawbar pull (DP) and motor drive current are reduced while sinkage is increased in partial gravity, and the variation with gravity doesn't have a simple (e.g. linear) influence on these parameters. Furthermore, the optical flow analysis presents clear evidence that the properties and characteristics of soil in partial gravity are significantly different.

All the above-mentioned results are consistent with a reduction in the soil's shear strength in reduced gravity. Lower shear strength leads to lower thrust, which can contribute to lower DP. It generates lower bearing capacity, contributing to higher sinkage. Reduced reaction forces generated by the soil both ahead and beneath the wheel reduces the torque (and thus current) required to balance them. Lower strength can enable more soil to be mobilized by the wheel's shearing action.

The results, datasets, novel apparatus and techniques presented in this thesis can help further the understanding of soil flow in reduced gravity and support the development of powerful and advanced models.

Effect of gravity on the DP

On ground experiments (OGE) overestimate DP measured in Martian-g by 16-52% and Lunar-g by 18-100%, **at equal wheel loading**. This comparison is equivalent to comparing 1/3 mass rover in 1-g to full mass rover in 1/3-g, and the results are significantly different. The difference between Martian and Lunar DP are small at slip levels up to and including 40%. However, at 70% slip Lunar gravity DP is a further 30% lower compared to Martian. Lower DP is consistent with a reduction in the soil's shear strength which is what is used to develop thrust. It is unclear what effect reduced gravity has on the other component of drawbar pull (i.e. resistance); this was elaborated further in Section 3.1.3.

Comparing DP value in OGE where **wheel loading is 37% less** than the Martian leads to similar trends and closely approximates the DP at lower gravity for lower slip ratios.

When studying and modeling partial gravity **DP** on earth, wheel loading may need to be **decreased** by up to 40% for more comparable results, but this requires further study.

Effect of Gravity on Sinkage

The sinkage data in PGE indicates 25% more sinkage experienced compared to OGE at equal wheel loading. At the same wheel loading, no significant difference is observed in sinkage values between Martian and Lunar gravities, while the OGE's sinkage values are noticeably lower than tests performed in either of these partial gravities. Higher sinkage is consistent with a reduction in the soil's strength, as its bearing capacity is related to this. Higher sinkage is normally associated with higher resistance forces acting on the driven wheel, but this assumes constant soil strength. In reduced gravity, it is unclear what the net effect of higher sinkage and lower shear strength is on resistance forces.

Increasing the wheel loading 37% in OGE, compared to PGE, results in analogous measured sinkages for all slip rates. Thus, when studying and modeling partial gravity **sinkage** on earth, wheel loading may need to be **increased** by 30% to 40% for more comparable and accurate results.

Effect of gravity Observed in Optical Flow Analysis

Optical flow-based visualization of the soil flow (imaged with a high-speed camera) shows that more soil is mobilized by the wheel in reduced gravity. More soil motion is observed in Martian-g than in Earth-g and, especially at high slip, even more is observed in Lunar-g. The greater amount of soil motion may be associated with a

weakening of soil strength in reduced gravity. Soil strength relies on friction, and thus gravity. Analysis of the force/torque data from the instrumented wheel experiments supports this by showing reduced traction in partial gravity compared to Earth-g (at equal normal load and slip). Another observation that can be concluded from the data is that the amount of soil mobilized by the wheel is more sensitive to slip in lower gravity. The difference between the amount of soil motion at 70% slip vs. 20% slip is much more obvious in Lunar gravity than in Earth gravity, for example.

In summary, soil mobilization appears to increase more with respect to time and with respect to slip rate in partial gravity than in Earth gravity. In Earth gravity the magnitude/depth of soil motion is small, and any changes in slip and wheel loading do not have a significant impact on the behavior. Recall that the wheel loading is the same for all tests in Figures 4.35 through 4.37, so the gravity acting on the soil is the only variable changed between the tests in Earth, Martian, or Lunar gravity in any given figure. From these results, it appears that the lower gravity reduces soil strength enough to induce more soil motion and lower drawbar pull.

Effect of Gravity on Sensitivity to Wheel Loading

In Martian gravity, the effects of wheel loading are not as significant as in OGE. The data demonstrate that increasing the wheel loading in partial gravity has less bearing on sinkage value compared to OGE. Another observation is that increasing the wheel loading increases DP values at a higher proportion in OGE than Martian gravity.

Effect of Gravity on Drive Motor Current

Motor current is lower in PGE despite higher sinkage. This lower current is another feature that can be explained by the reduced shear strength of the soil in PGE, thus generating lower reaction forces in the soil ahead and beneath the wheel balancing wheel torque. Lower soil reaction forces are consistent with reduced thrust, and

thus lower DP, and consistent with the greater soil motion observed in optical flow analysis. At 70% slip in Martian and Lunar gravities sinkage is nearly identical, therefore the significantly lower motor current and DP observed in Lunar gravity can only be explained by lower soil strength due to lower gravity.

Rapid Automated Soil Preparation, Repeatability & Performance in Reduced-gravity

The automated soil preparation and terramechanics testing system developed and studied in this work makes important contributions to the experimental study of planetary rover terrain interactions in relevant environments. It provides the capability to perform consistently repeatable soil preparation, a critical element of such experiments, in under 15 seconds while satisfying the many constraints and requirements stemming from operating on board a reduced-gravity flight aircraft. The main design features that enable the contribution are pneumatic manifolds to blow jets of air that loosen the soil and a vibrator that then compacts and levels the soil in the sandbox.

The consistency of the achieved soil preparation was studied both across locations in the sandbox and between subsequent preparations. ES-2 Martian soil simulant, a very fine sand, presents significant challenges for soil preparation as well as soil property measurement. Nonetheless, cone penetrometer readings show that repeatable soil preparation is achieved in the central 280 mm of the sandbox consistently. The height and levelness of the soil preparation are also observed to be highly repeatable with little variation ($<2\%$). Furthermore, sinkage and drawbar pull data collected from terramechanics experiments conducted in triplicate also demonstrate very high concordance with low variability.

The effects of the parabola maneuver itself, with 2 g maneuvers at its start and end, do not appear to have a significant effect on the soil preparation, as demonstrated

by cone penetrometer readings taken post-parabola in-flight and compared to readings from soil preparations conducted aboard the aircraft on the ground. It is the first research of its kind to develop rapid automated soil preparation and to study in-flight soil preparation in depth.

5.2 Contributions

A major contribution of this thesis is in evaluating the reduced-gravity interaction of the flexible ExoMars rover wheel while traversing soft terrain to characterize performance and risks related to future planetary rover missions.

The advanced soil preparation system developed for the reduced gravity flight is the first of its kind to be automated and rapid and expands the number of reduced-gravity parabolas that can be flown within a fixed flight campaign with soil consistently prepared before each and every parabola.

The rich data collected through the experimental campaign are unique. Controlling slip and wheel load, and directly measuring DP and visualizing wheel-soil interactions have never been conducted in reduced gravity. The key findings on the effect of gravity on wheel thrust, net traction of the rover, and sinkage combined with the corresponding visualization of the wheel-soil interaction fill the gap in the terramechanics research, scientific experiments, and literature.

Another key finding is that the Earth-based tests with reduced mass overestimate mobility performance of a full-mass rover in reduced gravity. The results establish direction and provide information on ways to perform on-ground experiments that resemble reduced gravity conditions.

5.3 Future Work

This study revealed the apparent disparity between the common assumptions in terramechanics and experimental data. Thus, to clearly identify the differences between reduced-gravity and on-ground experimentation, there need to be further experimental studies in low gravity environments.

There is an opportunity to further enhance the spatial consistency of the soil preparation, perhaps by altering the locations and quantity of output port while using the guidelines provided in this thesis to more evenly disturbing the soil.

A high priority direction for future work is to expand the types of soils and terramechanics experiments being studied with this system and its associated experimental framework. In addition, collection of extensive data is imperative to support and model the relationship between the soil motions at different gravities and the resulting rover mobility performance. Future research needs to be done on developing reduced-gravity terramechanics models based on the recent data collected in these gravity conditions.

Bibliography

[1] *Threaded fasteners handbook*. European Space Agency, 2010.

[2] *Requirements for threaded fastening systems in spaceflight hardware*. National Aeronautics and Space Administration, 2012.

[3] *Global exploration roadmap (3rd edition)*. International Space Exploration Coordination Group (ISECG), 2018.

[4] M. Apfelbeck, S. Kuss, B. Rebele, and B Schafer. A systematic approach to reliably characterize soils based on Bevameter testing. *Journal of Terramechanics, vol. 48, no. 4*, 2011.

[5] A. Azimi, J. Kovecses, and J. Angeles. Wheel-soil interaction model for rover simulation and analysis using elastoplasticity theory. *Robotics, IEEE Transactions*, pages 1271–1288, 2013.

[6] M. G Bekker. Photographic method of determining the soil action beneath footings. *2nd International Conference on Soil Mechanics and Foundation Engineering*, pages 193–194, 1948.

[7] M. G. Bekker. *Theory of land locomotion*. University of Michigan Press, 1956.

[8] M Black and P Anandan. The Robust Estimation of Multiple Motions: Parametric and Piecewise-Smooth Flow Fields. *Computer vision and image understanding*, pages 75–104, July 1996.

[9] A. Blake and A. Zisserman. *Visual Reconstruction*. MIT Press, 1987.

[10] W.W. Boles, W. D. Scott, and J. F. Connolly. Excavation forces in reduced gravity environment. *Journal of Aerospace Engineering, vol. 10, no. 2*, pages 99–103, 1997.

[11] I. Bolling. Soil compaction and driving force Behavior of tires - new measuring and calculation methods. *Dissertation, TU Munchen*, 1987.

[12] K. Bourne, C. Reddy, K.R. Kumar, and A. Ooi. An investigation of fundamental flow structures in ground effect with application to development of brownout conditions in hover. In *In 40th European Rotorcraft Forum*, Southampton, UK, September 2014.

[13] C. Brunskill, N. Patel, T. P. Gouache, C. M. Scott, G. P. Saaj, M. Matthews, and L. Cui. Characterisation of martian soil simulants for the exomars rover testbed. *Journal of Terramechanics,*, pages 419–438, 2011.

[14] C. Brunskilla. Characterisation of Martian Soil Simulants for the ExoMars rover testbed. *Journal of Terramechanics*, pages 19–438, December 2011.

[15] M. Budhu. *Foundations and earth retaining structures*. John Wiley & Sons, 2008.

[16] H. H. Bui, T. Kobayashi, R. Fukagawa, and J. C. Wells. Numerical and experimental studies of gravity effect on the mechanism of lunar excavations. *Journal of Terramechanics, vol. 46, no. 3*, pages 115–124, 2009.

[17] Carsten, K. Parabolic Flight. `http://carsten-killer.de/Dusty%20Plasmas/Parabolic%20Flights.html`, Online: accessed July 2018.

[18] D Chambers. Active Response Gravity Offload System. `http://www.nasa.gov/centers/johnson/engineering/integrated_environments/active_response_gravity/`, January 2013.

[19] N. Costes, G. Cohron, and D. Moss. Cone penetration resistance test-an approach to evaluating in-place strength and packing characteristic of lunar soil. *Proceedings of second Lunar science conference, Vol. 3,*, pages 1973–1987, 1971.

[20] C. Creager, V. Asnani, H. Oravec, and A. Woodward. Drawbar pull (dp) procedures for off-road vehicle testing. *NASA, Tech. Rep. TP-2017-219384*.

[21] L. Ding, Z. Deng, H. Gao, J. Tao, K. D. Iagnemma, and G. Liu. Interaction mechanics model for rigid driving wheels of planetary rovers moving on sandy terrain with consideration of multiple physical effects. *Journal of Field Robotics, vol. 32, no. 6*, pages 827–859, 2015.

[22] L. Ding, H. Gao, Z. Deng, K. Nagatani, and K. Yoshida. Experimental Study and Analysis on Driving Wheels' Performance for Planetary Exploration Rovers Moving in Deformable Soil. *Journal of Terramechanics*, pages 27–45, 2011.

[23] D.R. Freitag, A.J. Green, and K.J. Melzer. Performance evaluation of wheel for lunar vehicles. *Marshall Space Flight Center National Aeronautics and Space Administration*, pages 1–53, May 1970.

[24] A. Fujiwara, J. Kawaguchi, D. Yeomans, M. Abe, T. Mukai, T. Okada, J. Saito, H. Yano, M. Yoshikawa, and D. Scheeres. The rubble-pile asteroid itokawa as observed by hayabusa. *Science, vol.312*, pages 1330–1334, Jun 2006.

[25] E. P. Gnanamanickam, S. Lee, J. P. Sullivan, and S. Chandrasekar. Direct measurement of large-strain deformation field in machining. *SEM Annual Conference and Exposition*, pages 1080–1087, 2007.

[26] R. C. Gonzalez. Digital image processing using MATLAB. 2009.

[27] J. Guoa, H. Gaoa, H. Dinga, T. Guob, and Z. Deng. Linear Normal Stress under a Wheel in Skid for Wheeled Mobile Robots Running on Sandy Terrain. *Journal of Terramechanics*, pages 49–57, 2017.

[28] W. L. Harrison. Soil failure under inclined loadsII. *Journal of Terramechanics*, pages 11–50, 1973.

[29] G.H. Heiken, D. T. Vaniman, and B. M. French. *The Lunar sourcebook: A users guide to the Moon*. Cambridge University Press, 1991.

[30] K. Iizuka, Y. Sato, Y. Kuroda, and T. Kubota. Experimental study of wheeled forms for lunar rover on slope terrain. *9th IEEE International Workshop on Advanced Motion Control*, 2006.

[31] R. Irani, R. Bauer, and A. Warkentin. A dynamic terramechanic model for small lightweight vehicles with rigid wheels and grousers operating in sandy soil. *Journal of Terramechanics, vol. 48, no. 4*, pages 307–318, 2011.

[32] Z. Jia, W. Smith, and H. Peng. Terramechanics-based wheelterrain interaction model and its applications to off-road wheeled mobile robots. *Robotica, Vol. 30.3*, pages 491–503, 2012.

[33] M. A. Knuth, J. B. Johnson, M. A. Hopkins, R. J. Sullivan, and J. M. Moore. Discrete element modeling of a Mars Exploration Rover wheel in granular material. *Journal of Terramechanics*, pages 27–36, 2012.

[34] T. Kobayashi, Y. Fujiwara, J. Yamakawa, N. Yasufuku, and K. Omine. Mobility performance of a rigid wheel in low gravity environments. *Journal of Terramechanics, vol. 47, no. 4*, pages 261–274, 2010.

[35] J. Liu, H. Gao, Z. Deng, and J. Tao. Effect of Slip on Tractive Performance of Small Rigid Wheel on Loose Sand. *ICIRA*, pages 1109–1116, 2008.

[36] M. Lyasko. Multi-pass effect on off-road vehicle tractive performance. *Journal of Terramechanics, vol. 47, no. 5*, pages 275–294, 2010.

[37] G. Meirion-Griffith and M. Spenko. A modified pressuresinkage model for small, rigid wheels on deformable terrains. *Journal of Terramechanics, vol. 48, no. 2*, pages 149–155, 2011.

[38] S. Michaud, L Richter, T. Thueer, T. Gibbesch, T. Huelsing, N. Schmitz, S. Weiss, A. Krebs, N. Patel, L. Joudrier, R. Siegwart, and A. Schafer, B. Ellery. Rover chassis evaluation and design optimisation using the RCET. *Proceedings of the 9th ESA Workshop on ASTRA, Noordwijk*, 2006.

[39] N. Murdoch, B. Rozitis, S. F. Green, T-L. Lophem, P. Michel, and W. Losert. Granular shear flow in varying gravitational environments. *Granular Matter*, pages 129–137, 2013.

[40] T. G. Murthy, E. P. Gnanamanickam, C. Saldana, and S. Chandrasekar. Deformation field in indentation of granular materials. *6th International Conference on Micromechanics of Granular Media*, pages 263–266, 2009.

[41] H. Oravec, X. Zeng, and V. Asnani. Design and characterization of grc- 1: A soil for lunar terramechanics testing in earth-ambient conditions. *Journal of Terramechanics*, pages 361–377, 2010.

[42] N. Patel, R. Slade, and C. Jim. The ExoMars rover locomotion subsystem. *Journal of Terramechanics, Vol. 47.4*, pages 227–242, 2010.

[43] N. Patel, R. Slade, and C. Jim. Sensing Techniques to Characterize Locomotion on Soils to be Traversed by a Rover. *Proceedings of ASTRA, Noordwijk*, 2017.

[44] G. Pillinger, Geczy, Z. A. Hudoba, and P. Kiss. Determination of soil density by cone index data. *Journal of Terramechanics,*, pages 69–74, 2018.

[45] L. Rahmatian and P. Metzger. Soil Test Apparatus for Lunar Surfaces. *American Society of Civil Engineers, (ASCE)*, 2010.

[46] L. Raura, A. Warren, and J. Thangavelautham. Spherical Planetary Robot for Rugged Terrain Traversal. In *IEEE Aerospace Conference*, pages 1–10, Big Sky, MN, October 2017.

[47] A. Reece. Principles of Soil-Vehicle Mechanics. *Proceedings of the Institution of Mechanical Engineers, vol. 180, part 2A*, 1965.

[48] P. Reiss, P Hager, and A Hoehn. Flowability of lunar regolith simulants under reduced gravity and vacuum in hopper-based conveying devices. *Journal of Terramechanics*, pages 61–72, May 2014.

[49] B. Rozitis, E. MacLennan, and J. P. Emery. Cohesive forces prevent the rotational breakup of rubble-pile asteroid (29075) 1950 da. *Nature, vol.512*, page 174, Jun 2014.

[50] C. Senatore and K. Iagnemma. Analysis of stress distributions under lightweight wheeled vehicles. *Journal of Terramechanics, vol. 51*, pages 1–17, 2014.

[51] C. Senatore and K. Iagnemma. Analysis of stress distributions under lightweight wheeled vehicles Author links open overlay. *Journal of Terramechanics, Vol. 51*, pages 1–17, 2014.

[52] C. Senatore and C. Sandu. Off-road tire modeling and the multi-pass effect for vehicle dynamics simulation. *Journal of Terramechanics, vol. 48, no. 4*, pages 265–276, 2011.

[53] K. Skonieczny, S. J. M. Moreland, and D. S. Wettergreen. A grouser spacing equation for determining appropriate geometry of planetary rover wheels. *IEEE/RSJ International Conference on Intelligent Robots and Systems*, 2012.

[54] K. Skonieczny, S.J. Moreland, H. Inotsume, D. S. Wettergreen, V.M. Vivake M. Asnani, and C.M. Creager. Visualizing and Analyzing Machine-soil Interactions using Computer Vision. *Journal of Field Robotics*, pages 753–769, January 2014.

[55] K. Skonieczny, D. S. Wettergreen, and W. L. Whittaker. Considering the Effects of Gravity when Developing and Field Testing Planetary Excavator Robots. In Field and Service Robotics. *Field and Service Robotics: Results of the 10th International Conference*, pages 299–312, 2015.

[56] K. Skonieczny, D. S. Wettergreen, and W. L. Whittaker. Advantages of continous excavation in lightweight planetary robotic operations. *International Journal of Robotics Research*, pages 1121–1139, 2016.

[57] AE. Sommer, M. Nikpay, S. Heitkam, and M. Rudolph. A novel method for measuring flotation recovery by means of 4D particle tracking velocimetry. *Minerals Engineering*, pages 116–122, 2018.

[58] S. et al Strure. Mechanics of granular materials at low effective stresses. *Mechanics of granular materials at low effective stresses*, pages 67–72, July 1998.

[59] D. Sun, S. Roth, and M Black. Long range motion estimation using point trajectory. *IEEE Computer Society Conference on Computer Vision and Pattern Recognition*, Jun 2006.

[60] D. Sun, S. Roth, and M Black. Secrets of optical flow estimation and their principles. *IEEE Computer Society Conference on Computer Vision and Pattern Recognition*, pages 2432–2439, Jun 2010.

[61] R. Szeliski. *Computer vision: Algorithms and applications*. Springer, 2011.

[62] R. Szeliski and H. Shum. Motion Estimation with Quadtree Splines. *IEEE Transactions on Pattern Analysis & Machine Intelligence*, pages 1199–1210, 1996.

[63] K. Terzaghi. *Theoretical soil mechanics*. Wiley and Sons, INC., 1943.

[64] J. Wang. Pressure drop and flow distribution in parallel-channel congurations of fuel cells: U-type arrangement. *International Association for Hydrogen Energy*, pages 6339–6350, September 2011.

[65] J. Wang. Theory of flow distribution in manifolds. *Chemical Engineering Journal, 168*, pages 1331–1345, March 2011.

[66] W. Wang, F. Nicolleau, and N Qin. Comparison of turbulent flow through hexagram and hexagon orifices in circular pipes using large-eddy simulation. *Fluid Dyn. Res. 48 021408*, February 2016.

[67] Y. et al Wang. Hierarchical model-based interferometric synthetic aperture radar image registration. *Journal of Applied Remote Sensing*, 2014.

[68] C. V. White, J. K. Frankovich, P. Yates, G. Wells Jr, and L. Robert. A canble and temporary test facility on a shoestring budget: the MSL Touchdown test facility. Manhattan Beach, California, April 2008.

[69] M. Winnendael. Technical note-Martian reference soils for rover mobility. *ESA TEC-MMA*, November 2014.

[70] J.-Y. Wong. Behaviour of soil beneath rigid wheels. *Journal of Agricultural Engineering Research, vol. 12, no. 4*, pages 257–269, 1967.

[71] J. Y. Wong. *Terramechanics and Off-Road Vehicle Engineering. Terrain Behaviour, Off-Road Vehicle Performance and Design).* Elsevier, 2009.

[72] J.-Y. Wong and A. Reece. Prediction of rigid wheel performance based on the analysis of soil-wheel stresses part i. performance of driven rigid wheels. *Journal of Terramechanics, vol. 4, no. 1*, pages 81–98, 1967.

[73] Jo. Wong. Optimization of the Tractive Performance of Four-Wheel-Drive Off Road Vehicles. *SAE Transactions, Vol. 79*, pages 2238–2246, 1970.

[74] J. Xiao. Bilateral filtering-based optical flow estimation with occlusion detection. pages 650–656, 2006.

[75] K.J Yoon and I. S. Kweon. Adaptive support-weight approach for correspondence search. *IEEE Transactions on Pattern Analysis and Machine Intelligence*, pages 650–656, April 2006.

Appendix A

System Development

Development of Advanced Reduced Gravity Terramechanics Testbed

The advanced reduced gravity terramechanics testbed is consist of the experiment subsystem, control-box and the supply air for the pneumatic systems. The Experiment subsystem itself can be broken down into 3 modules: The main frame module, the sandbox module, and horizontal axis module.

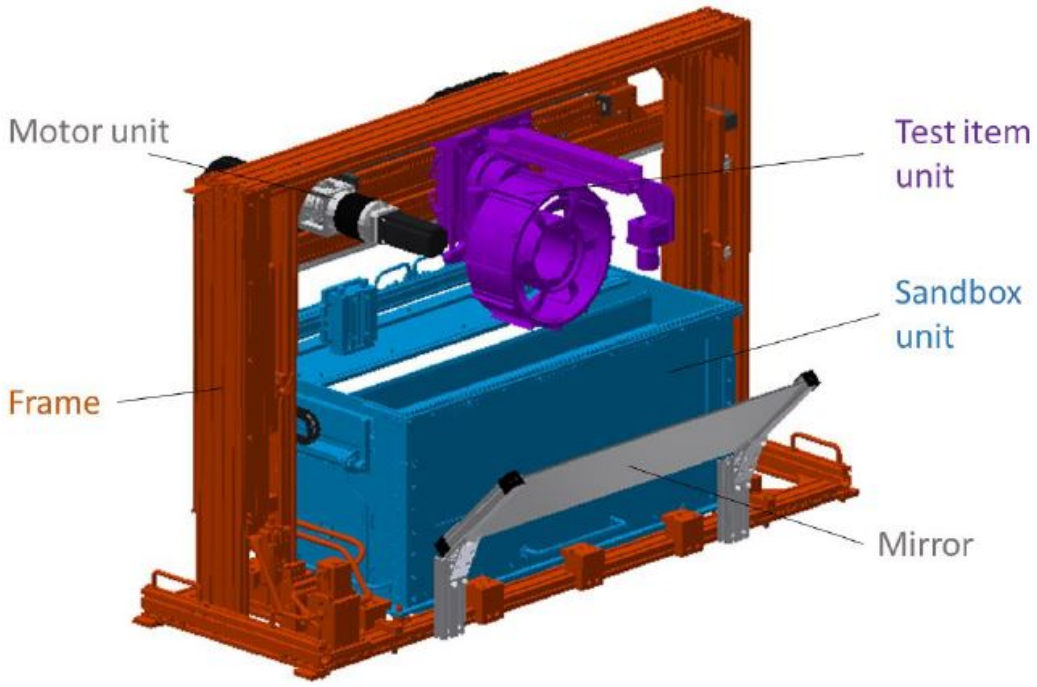

The Electronic Control Unit is utilize NRCs 10U instrumentation panel. The electronics is mounted inside, and a fully ruggedized laptop and E-stop is secured to the top, as shown in Figure A.1. Figure A.2 shows the schematic of power supplies and wiring for electrical devices in the controlbox. The number on the current lines (connecting wires) are the gauge numbers. As an additional safety precaution, the

system is commanded to enter home/safe configuration using a toggle switch. Figure A.3 represents the communication network between the Rrio controller which sends the command to Maxpos, AKD and IO extension. Through the toggle switch, the signal will be sent to the system to reset to the home position which is the safe and compact position of the system. Trio will be the main controller that sends commands to the drivers and digital modules. MaxPos is a driver for Maxon Motor that controls the motion of the wheel. AKD will be used to control the sliding motion of the wheel in the X axis, in addition to sending/reading analog signals and read digital input signals to/from the sensors. There is an I/O extension which sends digital output signals to the sensors. Once the toggle switch is activated, the home position will be set by trio sending command to the drivers and sensors. All vibration and sand preparation action is set to be off. Immediately the upper unit is up, wheel is up and move to a safe home location, and the plate covers the sand box.

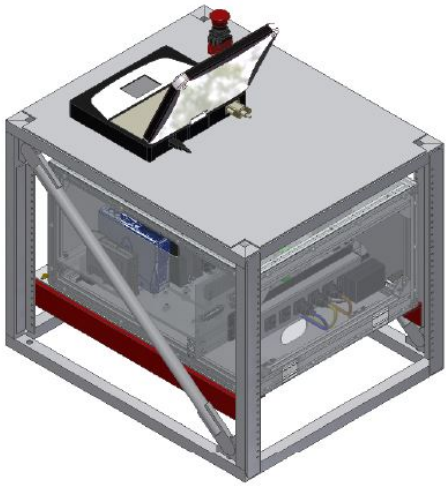

Figure A.1: Electronic Control Unit

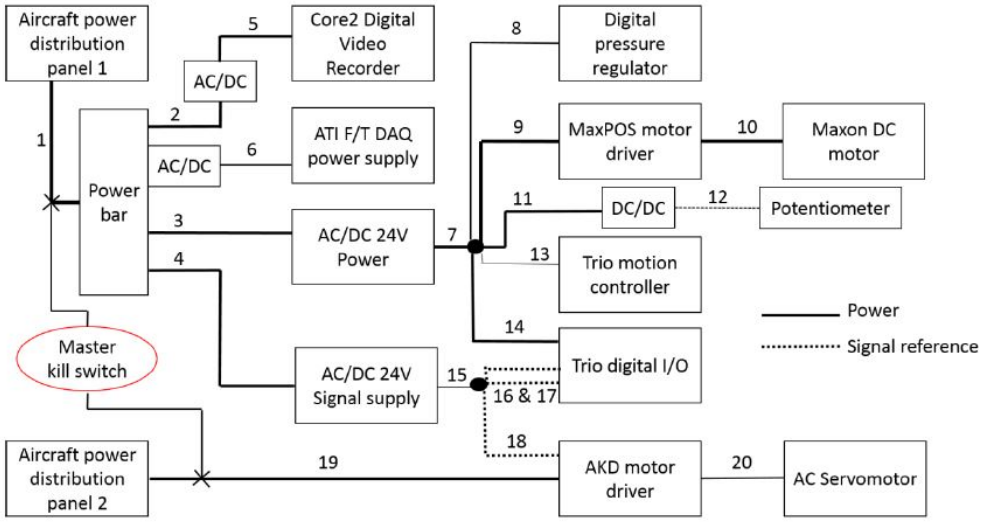

Figure A.2: Electronic schematic, lines after the power-bar is enclosed inside the control-box

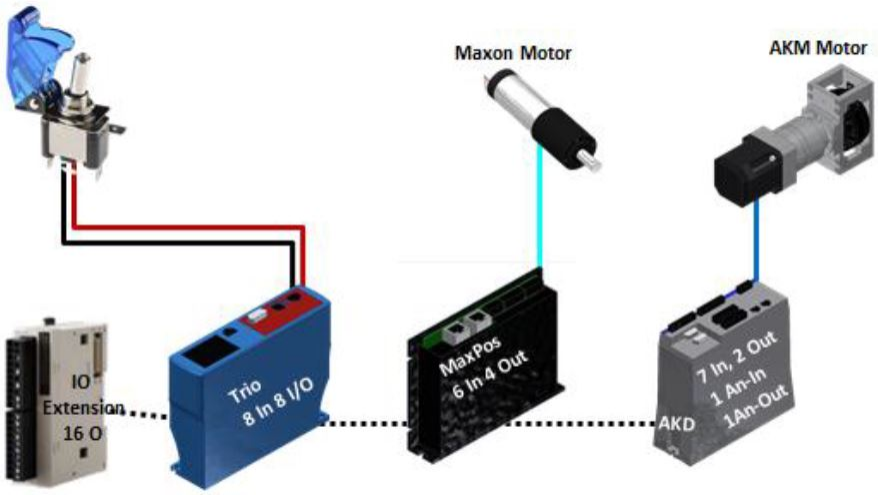

Figure A.3: Toggle switch and communication network for entering home/safe configuration

A.1 Flight Structural Verification

For structural analysis purposes, the Experiment subsystem can be broken down into 3 modules: The main frame module, the sandbox module, and horizontal axis module. The Experiment subsystem (Apparatus) is mounted to the aircrafts seat tracks via 2 aluminum bars (referred to subsequently as base bars), using 8 single-stud connectors.

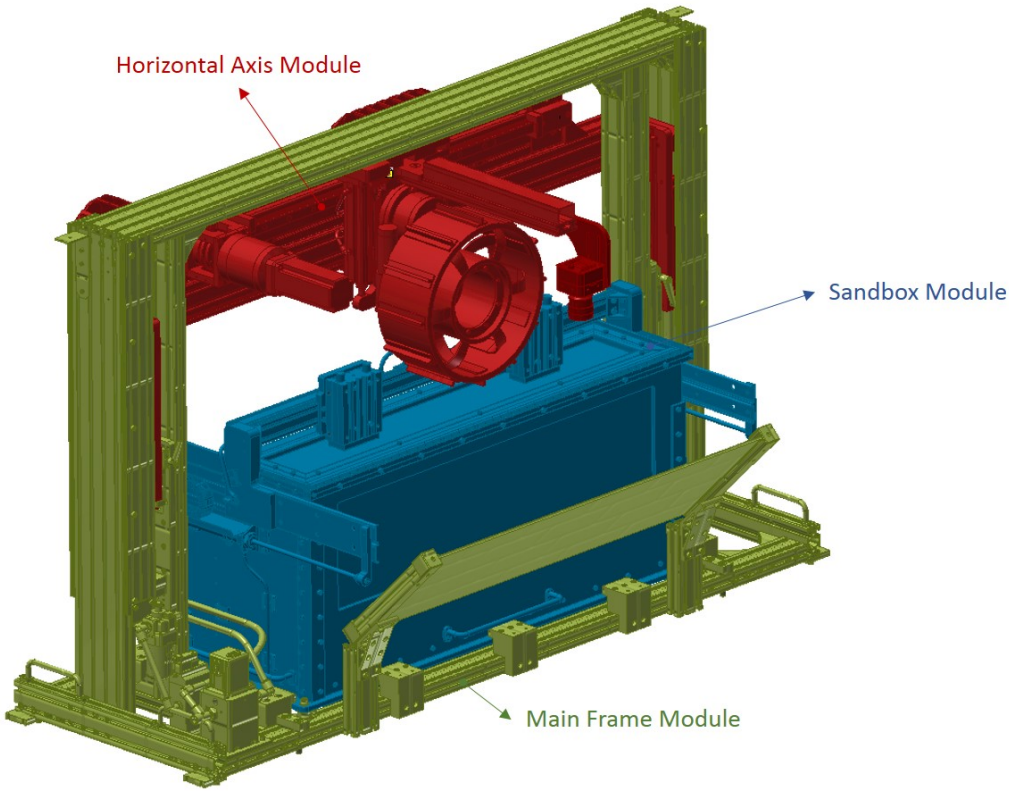

Figure A.4: Breakdown of Experiment subsystem into modules for structural analysis

All joints with bolts threaded directly into the aluminum extrusion include brackets for additional strength and stiffness. The bolts for fastening brackets pass through holes drilled through the extrusions and typically fasten to t-slot nuts in slots on the opposite side of the extrusion. In some cases there is another bracket on the opposite side of the extrusion, and then the bolts are fastened to hex nuts located at that opposite bracket. Examples of joint fastening techniques described above can be seen in Figure A.6.

Due to the motion (and vibration) required for the experiment, not all subassemblies are rigidly fastened to the system. In several places, for example, subassemblies are connected via sliders. In all such instances, the connection points themselves (sliders, etc.) are built to withstand or resist separation during the relevant load cases. At places where such non-fastened connections hold subassemblies of mass above 10 kg, additional 2-fold protection in the case of detachment is implemented: First, if detachment were to occur any detached subassemblies would remain captive

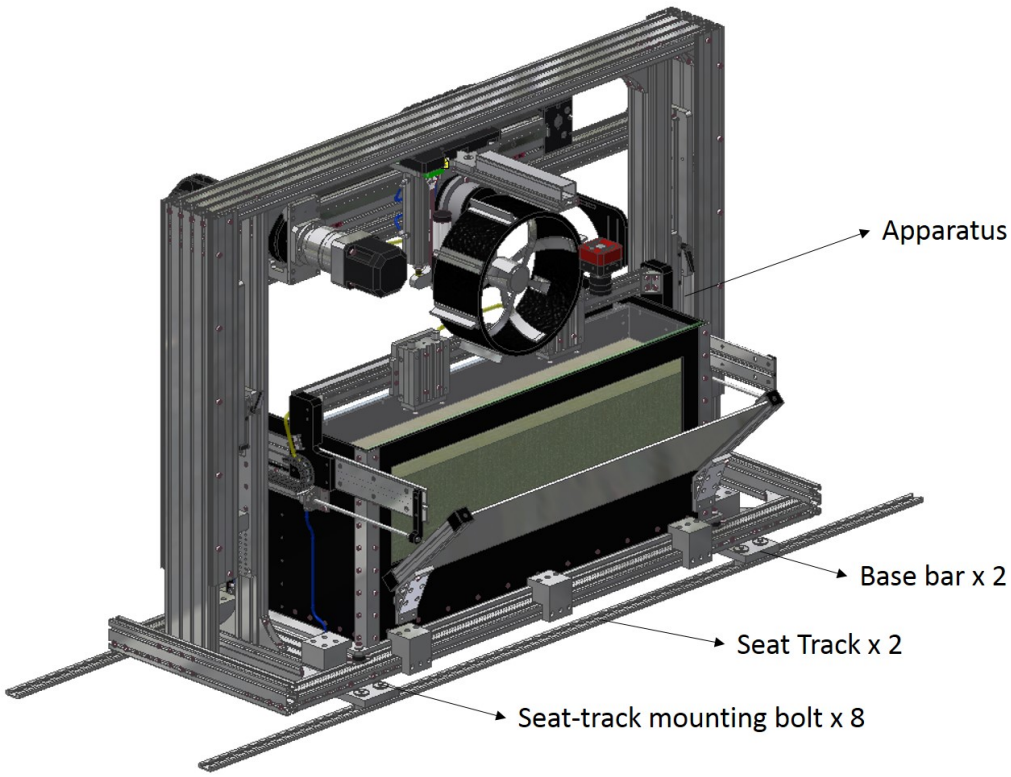

Figure A.5: Breakdown of Experiment subsystem into modules for structural analysis

within cage-like structures rigidly fastened to the structural frame; second, dampers are strategically located at such non-fastened connections to prevent impact loading in the unlikely event of detachment. Three connections, indicated in Figure structure3, meet the criteria described above: between the sandbox unit and the frame, between the horizontal axis unit and the frame; and between the test item unit and the horizontal axis unit.

The sandbox unit must be able to vibrate, and so is attached to the frame via 4 rubber mounts. These rubber mounts are not relied upon for the structural connection, though. Instead, the base plate of the sandbox unit is fully captive between the base of the frame and 10 rigid aluminum catcher blocks (fastened with bolts to the frame). The structural analysis ignores the rubber mounts entirely and assumes the only reaction forces on the sandbox base are from the blocks.

This is a worst case scenario as, with a nominal spacing of 3 mm between the sandbox base plate and the blocks, elastic deformation of the rubber (again, ignored here) would likely carry some of this structural load. The horizontal axis unit drives the test item unit horizontally, but itself is also actuated vertically to displace the test item into and out of the sandbox. This vertical motion is along a pair of sliders and is actuated via a pair of pneumatic cylinders. The sliders are mounted to the frame facing opposite directions (fore and aft), such that a load acting to separate one

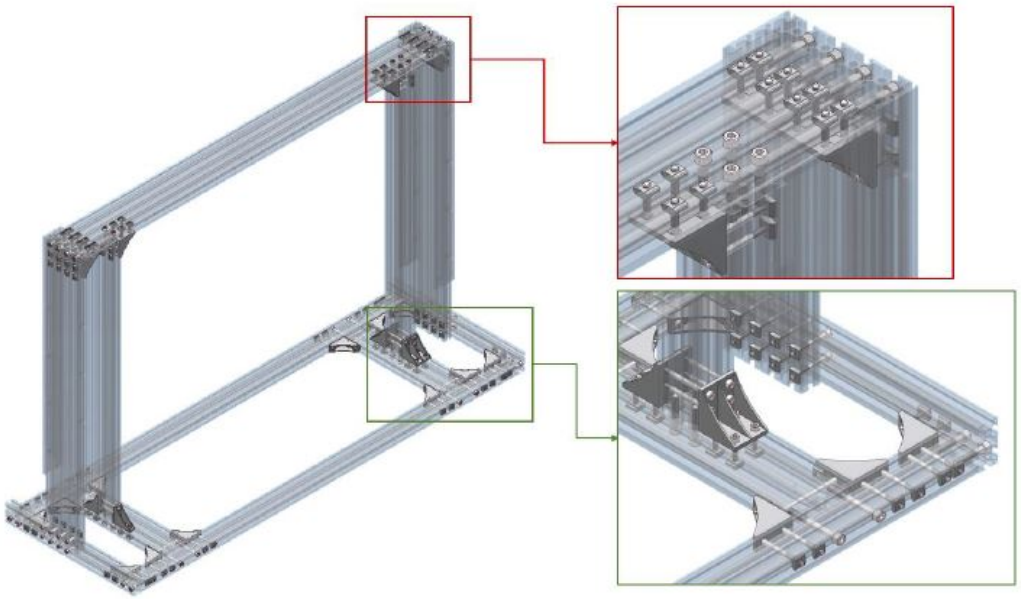

Figure A.6: Examples of joint fastening techniques

slider would simultaneously push the other sliders two halves together. Vertically (i.e. along the sliding direction), the pneumatic cylinder would first reach its maximum stroke and then the horizontal axis unit would contact the frame before the two side of the sliders ever separate. In addition to such an inherently captive design, additional side-walls are fastened to the frame to further cage the unit. Further, rubber dampers are mounted to the frame in the locations the unit would impact if its primary captive measures failed (and were to become detached and free within the secondary (side-wall) cage. The test item unit, which can move fore and aft along the horizontal axis unit, is prevented from coming off its slider at either end with rigid structural blocks. Rubber dampers are also placed at both ends of the slider to mitigate the impact of any contact between the test unit and the rigid blocks.

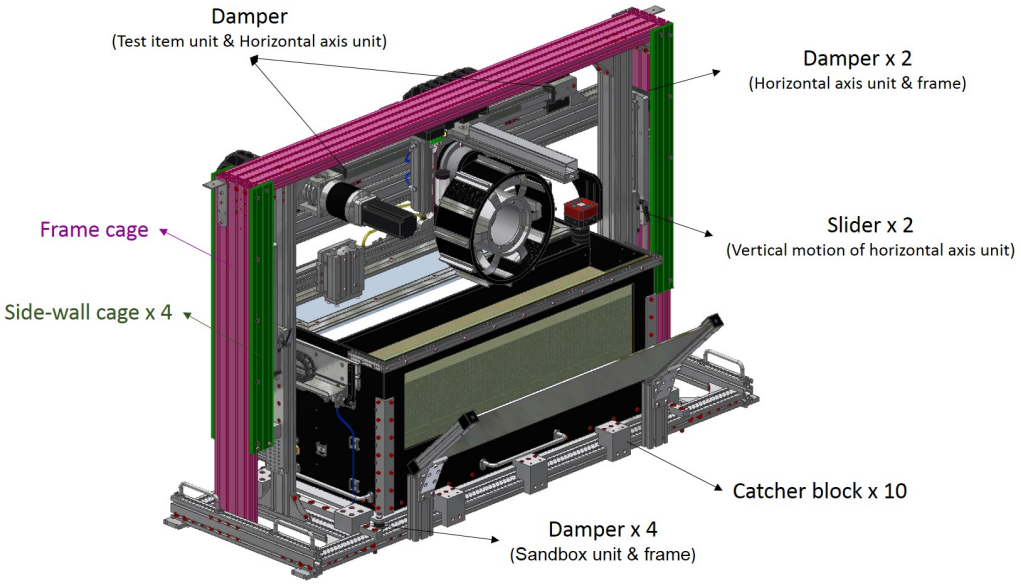

Figure A.7: Experiment subsystem mounting interface

A.2 Flight Structural Modeling

A.2.1 Modeling main frame module

To simplify the modeling of the main frame structure for analysis, it was divided to two separate modeling units as shown in Figure A.8. The structural frame as one unit and additional hardware, including fasteners, brackets, side-walls, sliders as another unit. To model the structural frameunit, the aluminum extrusions and blocks that make up the frame are simplified within the structural model to enable practical analysis (see Figure A.9). The complex extruded cross-sections are replaced with hollow rectangular beams of the same cross-sectional area and moment of inertia. The recovery point on these beams is selected to match the outer dimensions of the extrusions (as the outer dimensions of the simplified beams may not be the same). The final model of the structural frame-unit that is simplified by hollow rectangular beams is presented in Figure A.10. Note that the coordinate system in CAD model is modified for the analysis to be compatible with the Femap software.

Additional hardware are modeled as point masses at their respective centers of mass and rigidly connected to the structure. As shown in Figure A.12, the mass and the center of gravity (COG) for each part is calculated, then each part and the fastener-module is represented as a point mass for the analysis

The model of the structural frame unit with additional hardware point masses and the finalized model of the main frame structure are presented in Figure A.13 and Figure A.14, respectively.

Note that the mirror is modeled as a point mass with a physical offset to account for its protrusion from the frame; it is connected in the structural model with massless rigid bars.

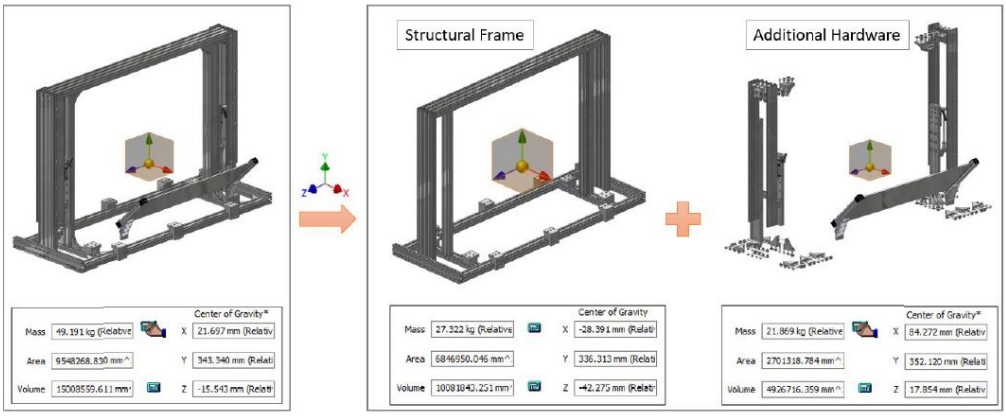

Figure A.8: Division of main frame module into structural frame & additional hardware

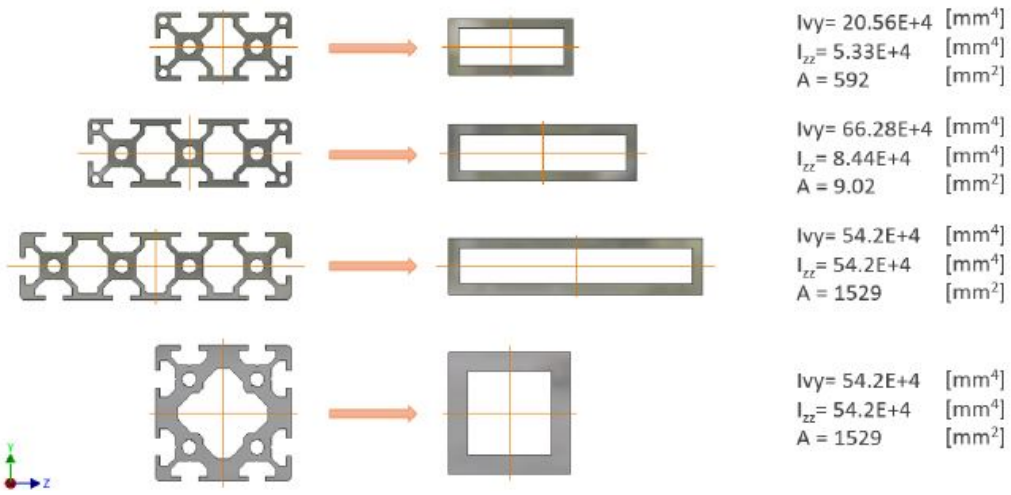

Figure A.9: Simplified modeling of aluminum extrusions as hollow rectangular beams

A.2.2 Evaluating main frame module model

To represent the 8 single-stud connectors, the structural model is constrained at 8 points where the main structural frame is mounted to the seat-tracks via 2 base bars (refer to Figure A.5). To check that the elements within the structural model are correctly connected in Femap, accelerations are applied to the model in the x, y, and z directions in turn. The total reaction forces summed across all the model constraint points (i.e. places where the structure is connected to the seat-tracks) are checked to make sure they equal the mass of the full model, "M", multiplied by the applied acceleration, "A" (See Figure A.16). To ensure the connectivity of the nodes in a way that there would be no floating point in the model, check/Merge Coincident Node is applied before the analysis.

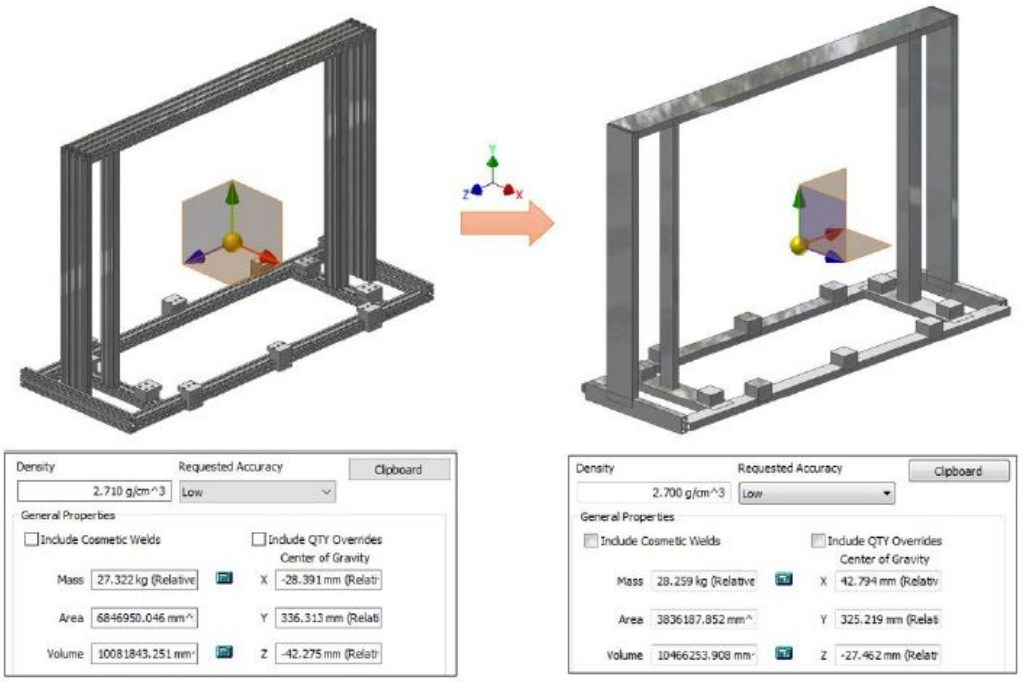

Figure A.10: Structural frame modeled with hollow rectangular beams

A.2.3 Modeling horizontal axis module

The horizontal axis module is replaced by a single point mass for structural analysis purposes and rigidly connected to the frame. Figure A.16 shows the calculation of mass and the COG of the module.

A.2.4 Modeling sandbox module for overall structural analysis

For the purposes of analyzing the sandboxs effect on the main frame modules and overall Experiment subsystems structural integrity, it is treated as a rigid body constrained only by the frames catcher blocks. A static analysis of force and moment equilibria, based on the acceleration load case and the sandbox mass (and COG), yields the reaction forces on the 4 relevant catcher blocks as shown in Figure A.17. The resulting forces are applied to the structural model at the respective catcher blocks.

Note that for analyzing the structural integrity of the sandbox itself, a separate model is created and introduced in section A.3.

A.2.5 Integrating the final model, overall structural analysis

The representations of the horizontal axis module (as a point mass) and sandbox module (as reaction forces), described in the preceding subsections, are integrated

into the overall structural model developed in previous sections A.2.2 - . The resulting model (visualized in Femap) is shown in Figure A.18.

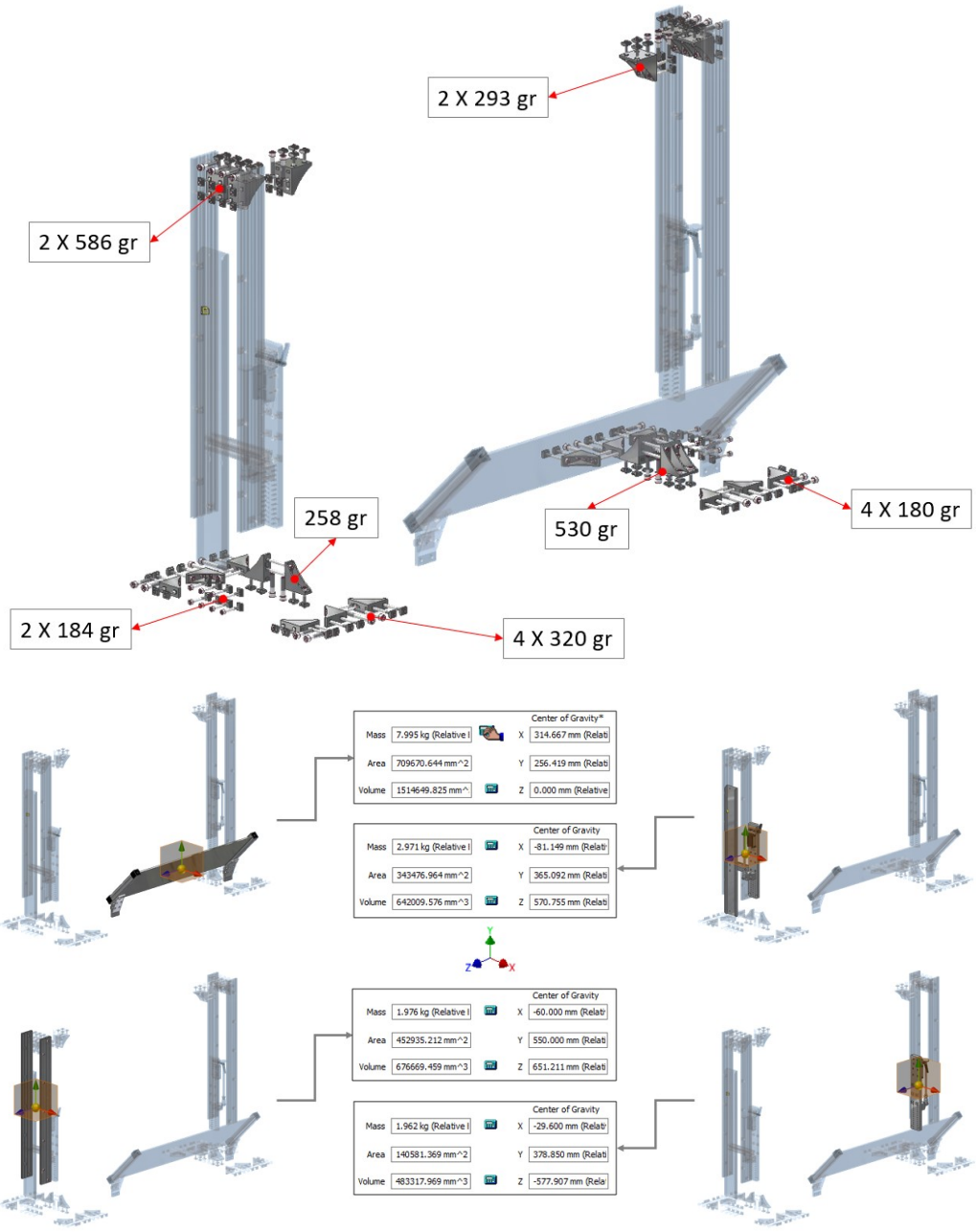

Figure A.11: Mass and COG of additional hardware elements

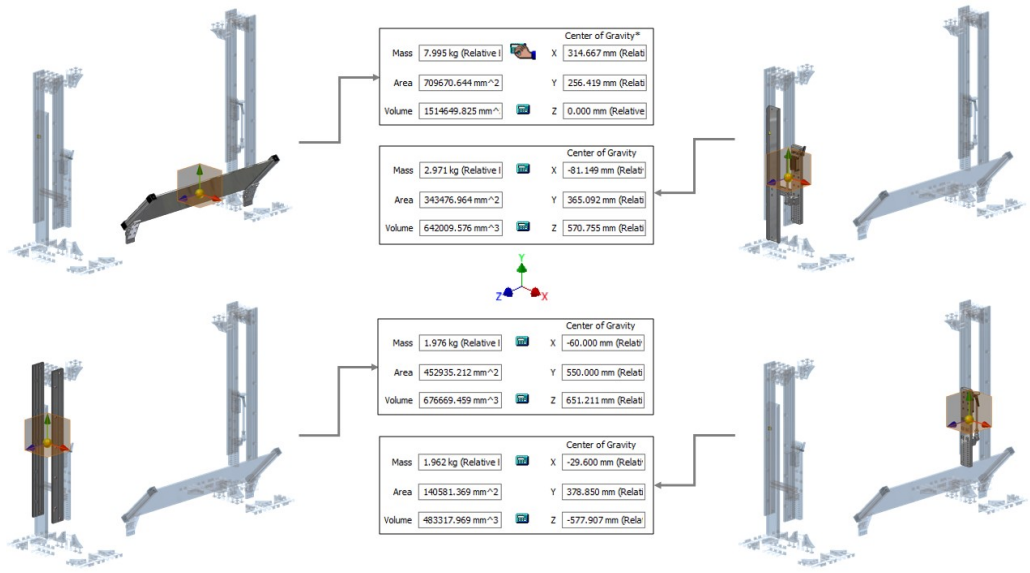

Figure A.12: Mass and COG of additional hardware elements

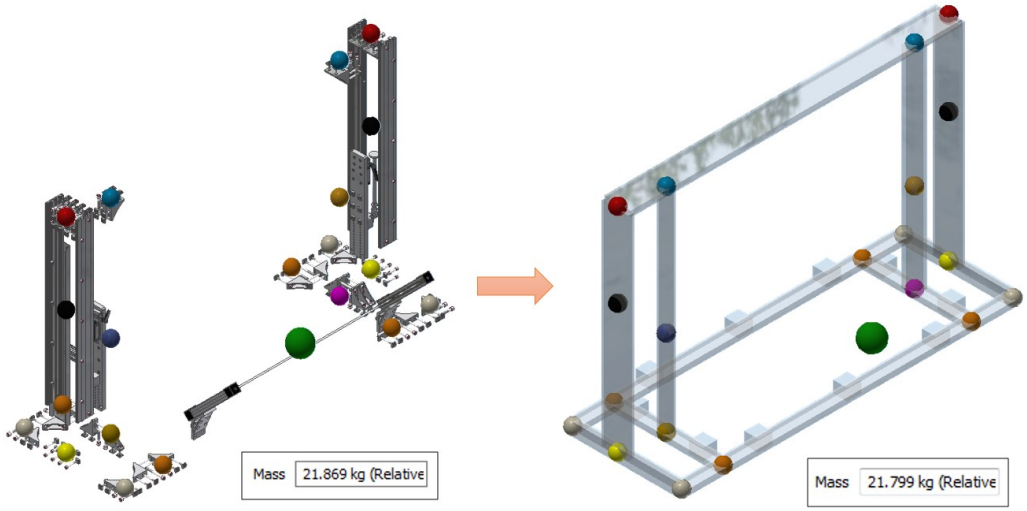

Figure A.13: Additional hardware point masses merged with structural frame model

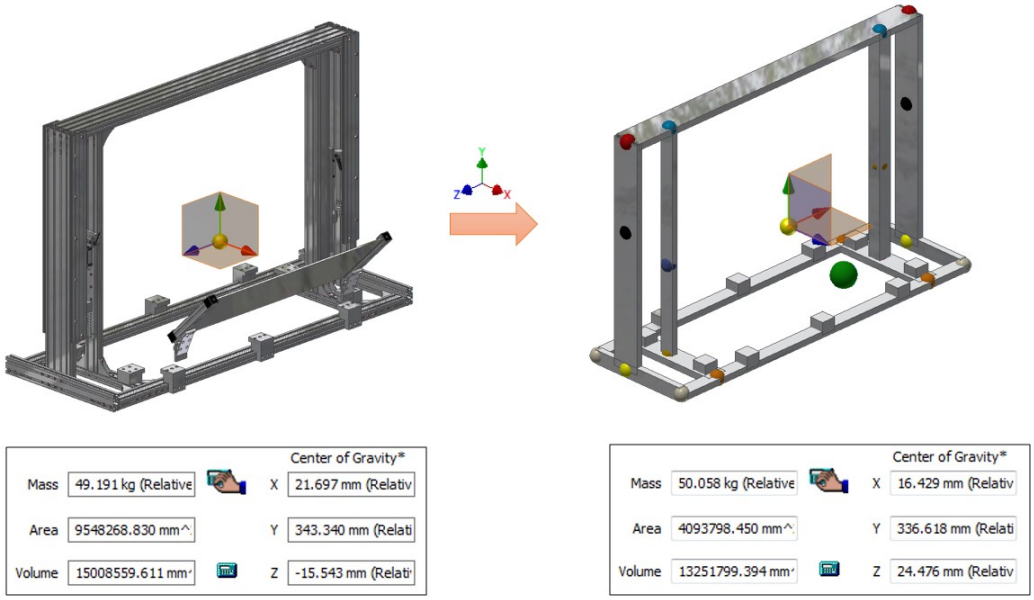

Figure A.14: Comparison of design model (left) to structural model (right)

	M (kg)	A (m/s^2)		C1	C2	C3	C4	C5	C6	C7	C8
CAD	54.439										
Femap	54.439	Ay = -10	Fy (N)	61.938	56.837	73.117	71.959	62.29	67.212	74.962	76.07
Femap	54.438	Ax = 10	Fx (N)	93.286	93.286	98.843	98.843	34.618	34.618	45.445	45.445
Femap	54.438	Az = 10	Fz (N)	51.901	73.183	54.369	82.334	70.892	51.538	91.963	68.204

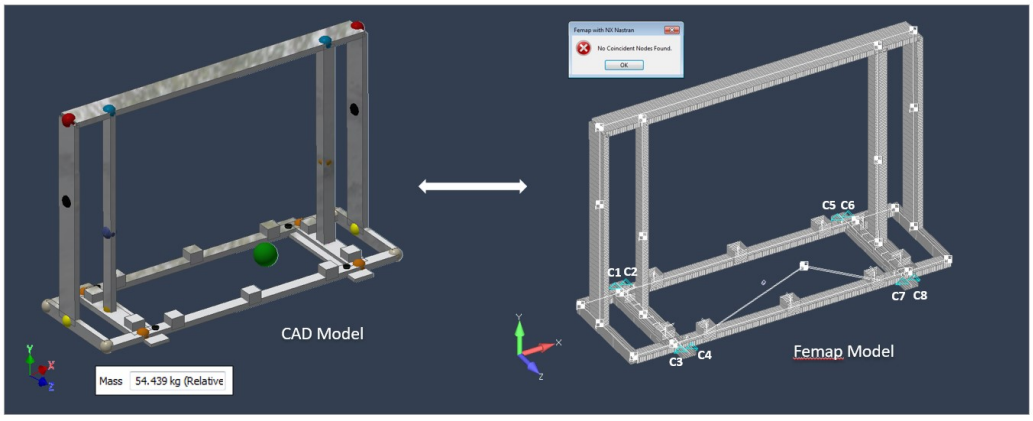

Figure A.15: Checks performed on main frame structural model

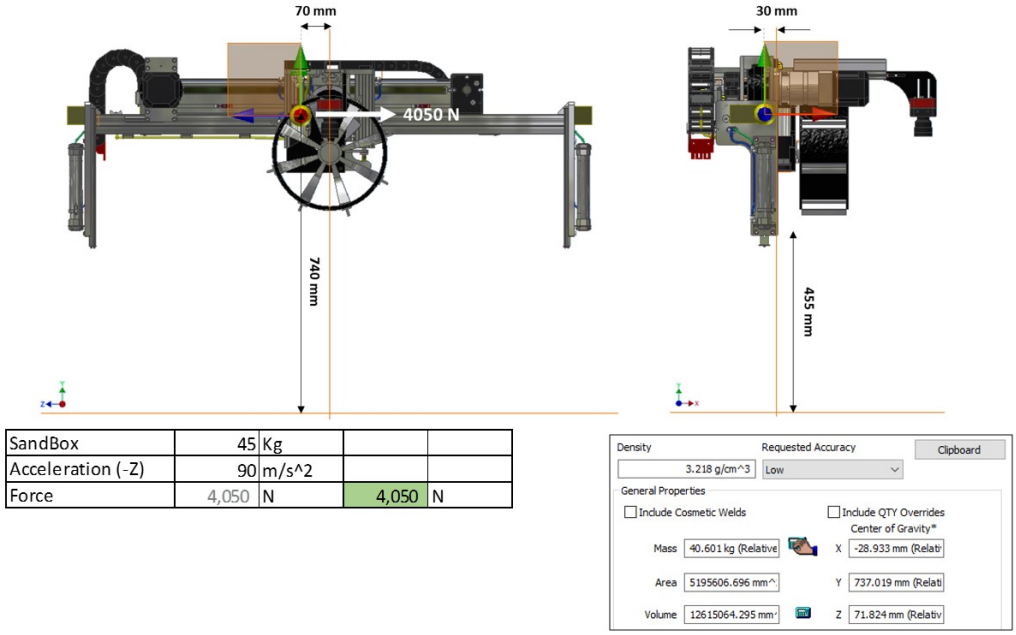

Figure A.16: Mass and COG of horizontal axis module

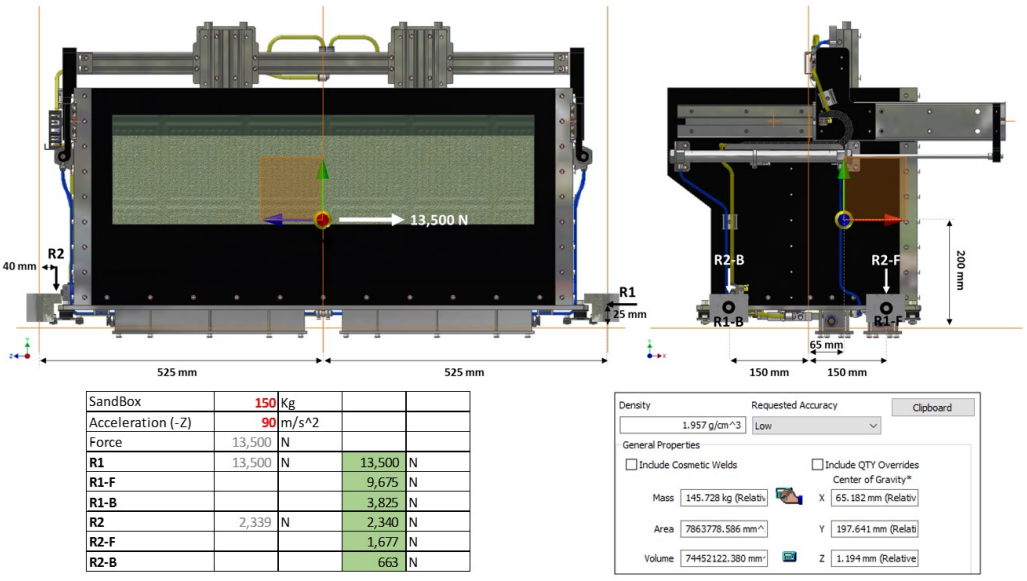

Figure A.17: Rigid sandbox model for determining reaction forces on the sandbox catchers (9g-fore load case shown)

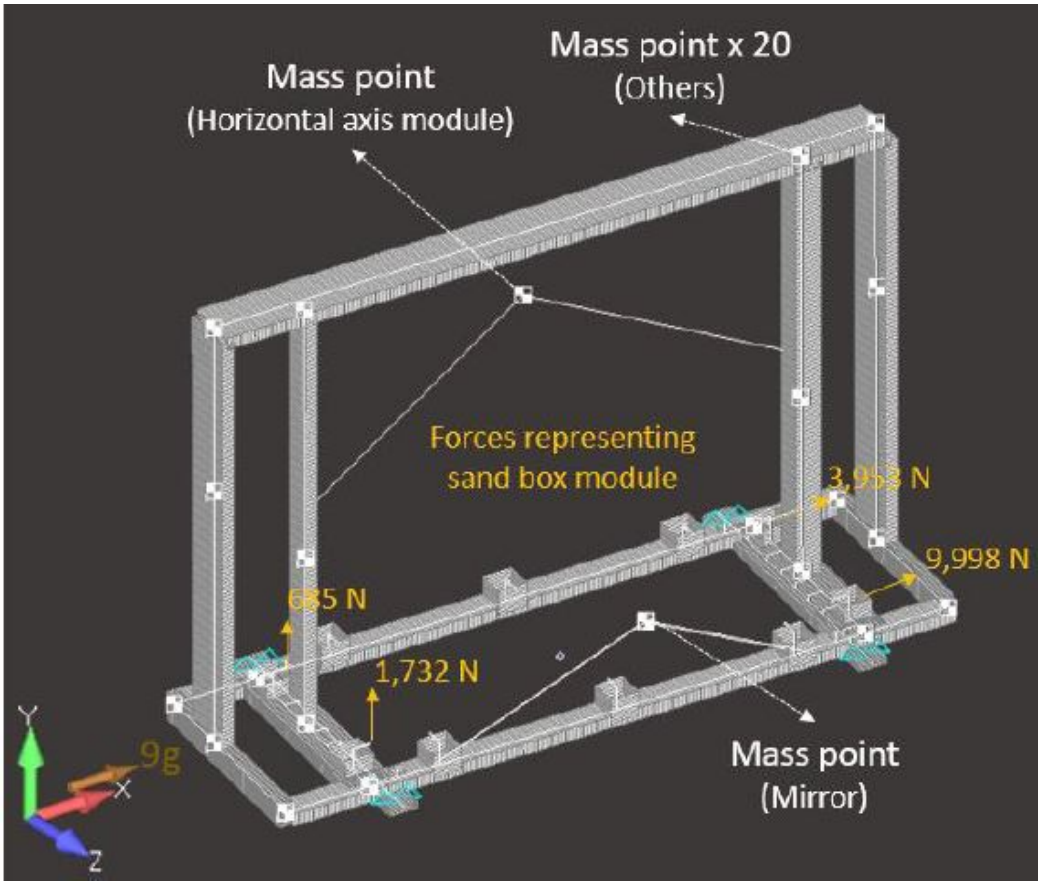

Figure A.18: Overall structural analysis model of Experiment subsystem, shown with 9g-fore load case applied

A.3 Structural Analysis

The structural modeling and visualization is done using Femap v11.3.2. Analyses are conducted using NX NASTRAN engine. Of the following subsections, A.3.1-A.3.3 deal with the analysis of the main structural frame, A.3.5 deal with the analysis of the sandbox, and later subsections deal with other subassemblies separately. Sample analysis and outputs are provided for the 9g fore load case.

A.3.1 Base bar bolt analysis - 9g fore load case

As mentioned above, the main frame module is connected to the seat-tracks via 2 base bars. It is crucial to analyze how the frame is fastened to these base bars, handled here, and how these base bars are fastened to the seat-tracks, handled in the next subsection. One-dimensional cylindrical bar elements are used in the structural model where fasteners link two elements, such as an aluminum extrusion to a base bar. Force and moment outputs are extracted at these fastener elements from the analysis.

At locations B2-B6 and B9-B14 (see Figure A.19 through Figure A.21) the analysis points represent a single fastener. At locations B1, B7, B8, and B14 the analysis points represent a pair of fasteners in close proximity.

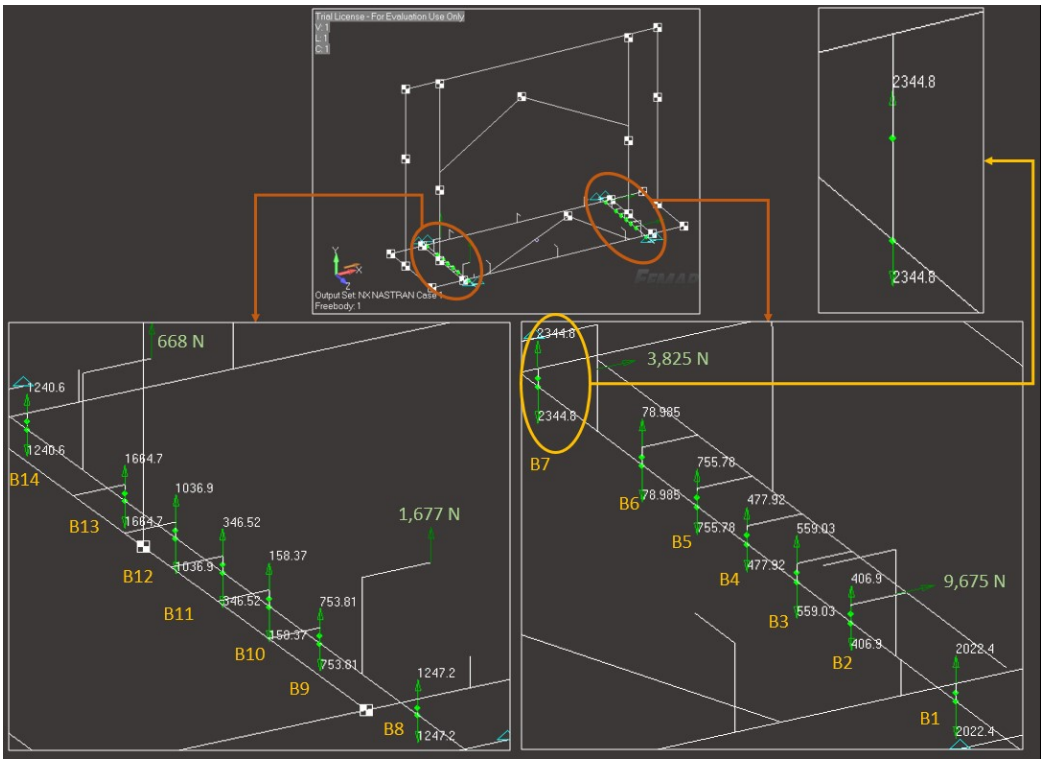

Figure A.19: Axial force results at the interface between the main frame module and the base bars

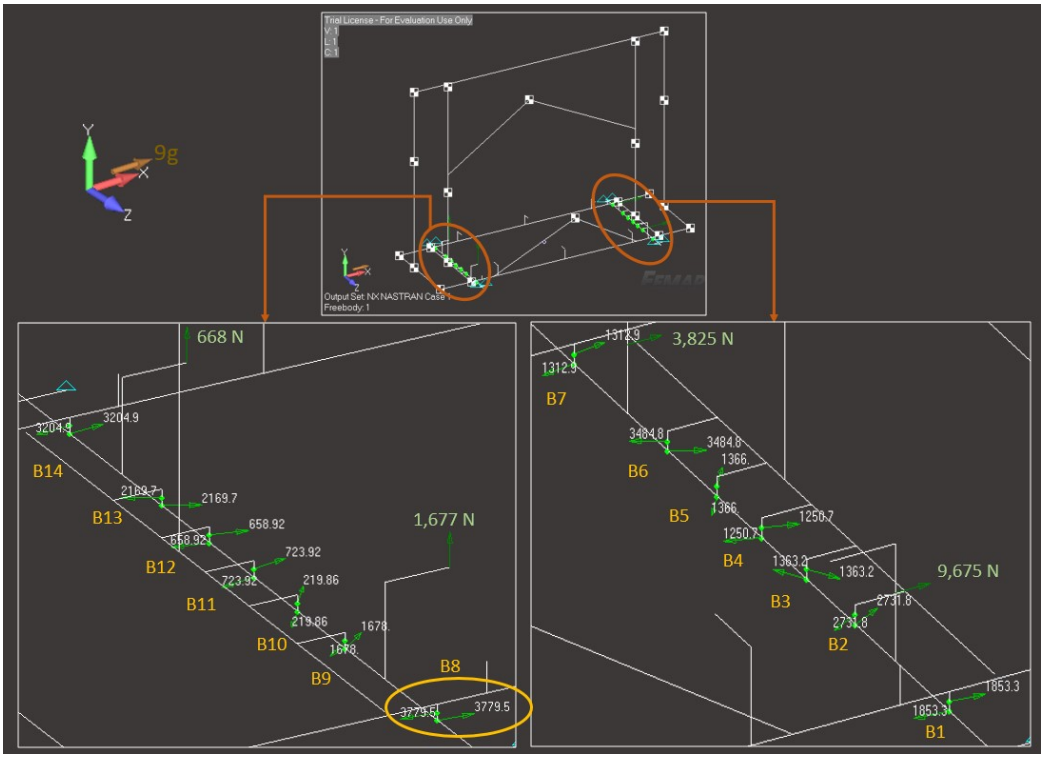

Figure A.20: Shear force results at the interface between the main frame module and the base bars

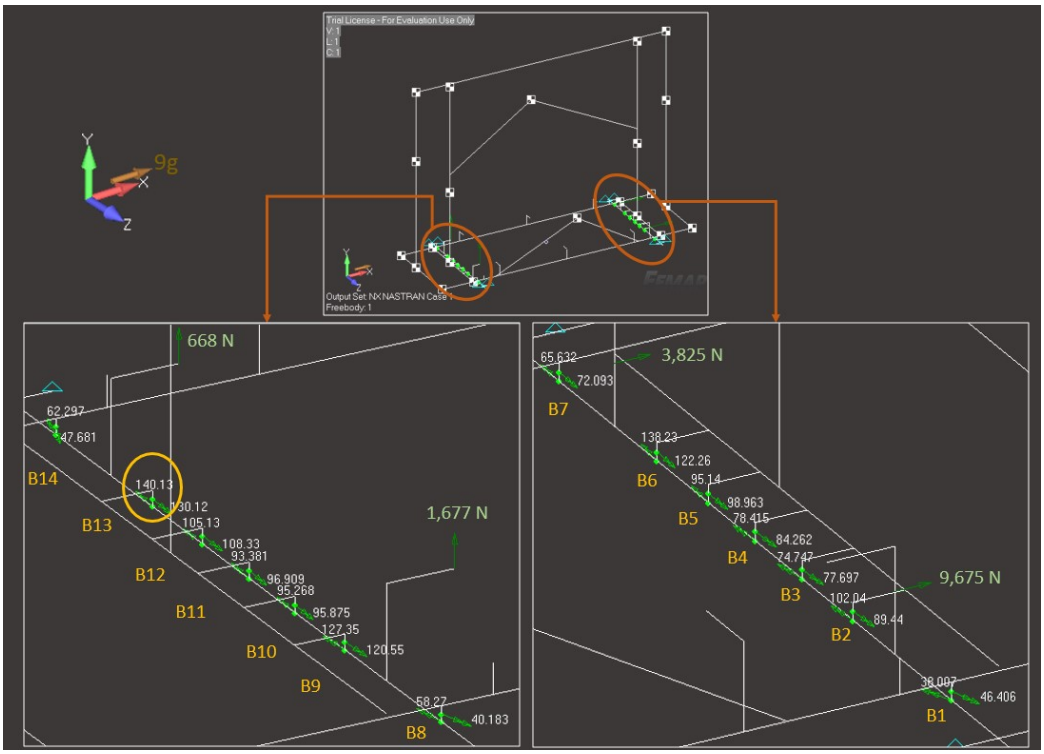

Figure A.21: Bending moment results at the interface between the main frame module and the base bars.Location of maximum bending moment indicated

From investigation of the analysis points, taking into consideration that some represent 2 fasteners and others 1, B13 is subject to the highest axial load, highest shear load, and highest bending moment. It is thus considered the worst case fastener for further analysis. Bolts are fastened to a preload of 60% of the bolts yield strength (note, this will be achieved in practice with a torque wrench and Loctite). The actual applied torque is calculated as a proportion (6/7 in the case of 60% preload) of the reference torque provided by Unbrako , which is given for a 70% preload. For the M10 base bar bolts discussed here, for example, the required torque is 66N (585 in-lbs). For a bolt, the maximum permitted axial load is calculated as the bolts tensile strength multiplied by effective cross-sectional area; this is compared to the preload + axial tension extracted from the analysis. The axial tension for each bolt is calculated as the sum of the axial force extracted from the Femap analysis plus the axial force induced by the moments extracted from the Femap analysis. Specifically, at each bolt Femap outputs 3 forces and 3 moments. One of the forces is the axial force (referred to as the "axial force from Femap" in Table A.22), as per the assigned coordinate system. Of the moments, one acts about the axis of the bolt; the other 2 can cause stress on the joint that results in additional axial loading of the bolt. To compute a worst-case scenario of this additional loading, both moments are combined regardless of their orientation and this total moment is divided by a distance to a relevant center of rotation close to the bolt. In the case of the base bar bolts analyzed here, for example, the center of the bolt is 15 mm away from the edge of the frame bar that is being bolted down to the base bar, so the total moment is divided by 15 mm to find the additional axial force (referred to as "axial force produced by $\sqrt{Mx^2 + Mz^2}$ " in Table A.22). The total axial force for any particular load case (in this case, "Axial force in 9g") is the sum of the "axial force from Femap" and axial force produced by moments.

The normal force between the two elements being fastened is computed as the preload minus the axial tension. Maximum allowable shear force is computed as this normal force multiplied by the friction coefficient (0.21 for Al-Al contact); this is compared to the shear force output by the analysis (vector sum of the 2 non-axial forces). To facilitate the comparison of the forces, the safety factor for axial and shear forces is calculated. From Table A.22, it can be concluded that M10 is a suitable bolt for this interface.

A.3.2 Seat track stud bolt analysis - 9g fore load case

The aluminum base bars described above will be fastened to the seat-tracks using 8 Telair singlestud seat-track fasteners provided by NRC (C1-C8 in Figure A.23 through Figure A.25). Constraint reaction forces and moments are compared against the fasteners specified capacities in tension, shear, and bending. For tension, the capacity is compared against constraint Fy (see Figure A.23 to view the coordinate frame definition). For shear, the capacity is compared against the total constraint force in the x-z plane. For bending, the capacity is compared against the constraint moment output: $\sqrt{Mx^2 + My^2}$

	B13
	M10
Major diameter [mm]	10
Pitch [mm]	1.5
Tensile strength [Mpa]*	1,300
Yield strength [Mpa]*	1,170
Percentage of preload [%]	60%
Friction coefficient (Al to ST)	0.21
Axial force [N] (From Femap)	1664.7
Shear force [N] (From Femap)	2169.7
SQRT(Mx^2+Mz^2) [N.m] (From Femap)	140.13
Axial Force Produced by SQRT(Mx^2+Mz^2) [N]	9342
Axial force in 9g [N]	11,007
Shear force in 9g [N]	2,169.7
Minor diameter	8.376
Effective diameter [mm]	8.59
Effective cross section area [mm^2]	58.0
Preload [N]	40,709
Max permited axial force [N] (After preload)	34,678
9g Normal force [N]	29,702
9g friction force [N]	6,237
Safety Factor (Axial)	1.46
Safety Factor (Shear)	2.87

* Tensile and yield strength data taken from Unbrako product guide

Figure A.22: Calculation of axial and shear safety factors for worst case base bolt under 9g-fore load case

The specification of the single stud connectors, provided in the Telair International catalogue, lists tension, shear, and bending capacity as 27220 N, 9980 N, 265 N.m, respectively. Based on the analysis presented in Figure A.23, Figure A.24, and Figure A.25, all forces and moments at the eight constraints are within the capacity of the single stud connector specified above.

A.3.3 Frame stress analysis 9g fore load case

The results of analysis of the stress in the frame members is presented in Figure A.26. The maximum stress resulting from the 9g fore load case (the worst case encountered in the analysis) is 164 MPa. The strength of the aluminum extrusion is rated at 245 MPa and proofed at 205 MPa.

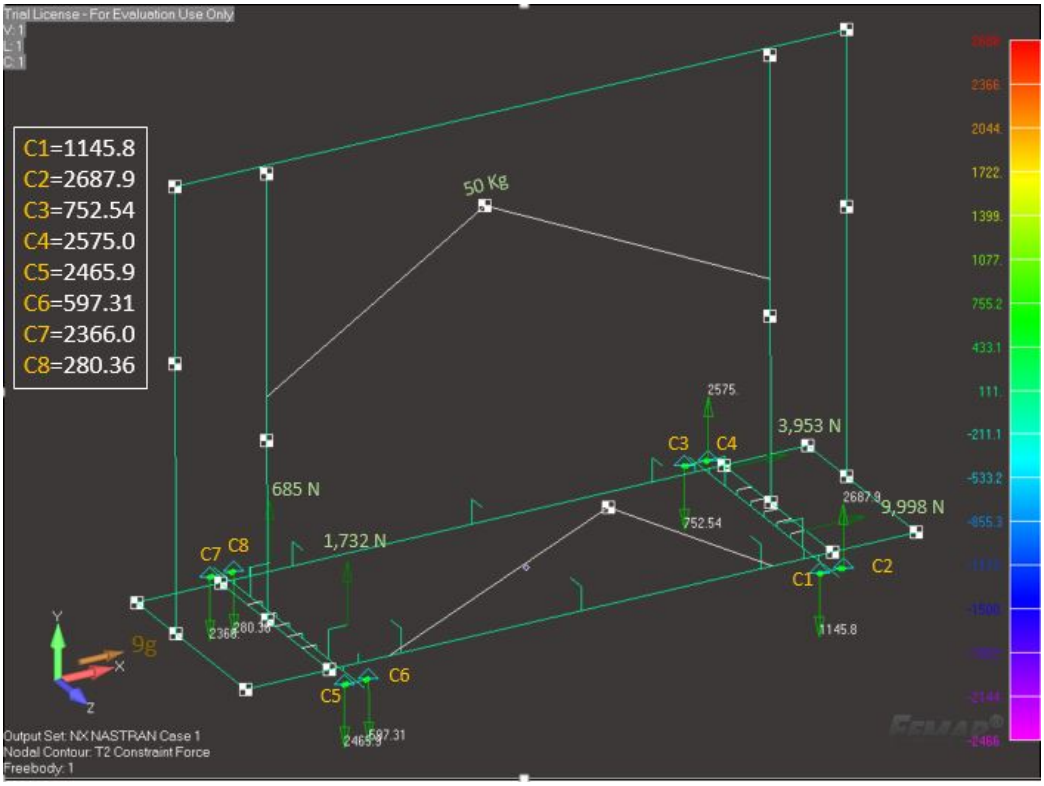

Figure A.23: Tension force analysis outputs at the interfaces between seat-track and base bar (9g fore load)

A.3.4 Frame joint analysis 9g fore load case

The elements of the frame structure are connected together at 16 joints. The joints are significantly simplified for analysis purposes. As described in section A.1, each of these joints includes bolts threaded into an element (or nut) after passing through a through-hole in the other element; these bolts are the ones analyzed here. Each joint also includes at least one bracket secured with additional bolts that pass through through-holes in both elements, but these brackets are ignored here to simplify the analysis. In reality, these brackets provide additional safety margin beyond the safety factors computed here. Figure A.27 indicates (in red) which bolts are included in the analysis of the structural frame joints. Note that for joints J-13 through J-16, no bolts are analyzed. The structural elements on either side of these joints are both connected to the same base bar, as explored in detail in section A.3.1. This allowed us to ignore the direct connection between the elements themselves (though additional bolts and brackets are indeed located at those joints to provide additional strength). An inset in Figure A.28 shows how these joints are treated as disconnected in the structural model itself. The connections between these elements and the base bars were shown in Figure A.19, for example.

At joints J-1 through J-12, forces and moments are extracted from the Femap/NASTRAN analysis, as shown in Figure A.28. These forces and mo-

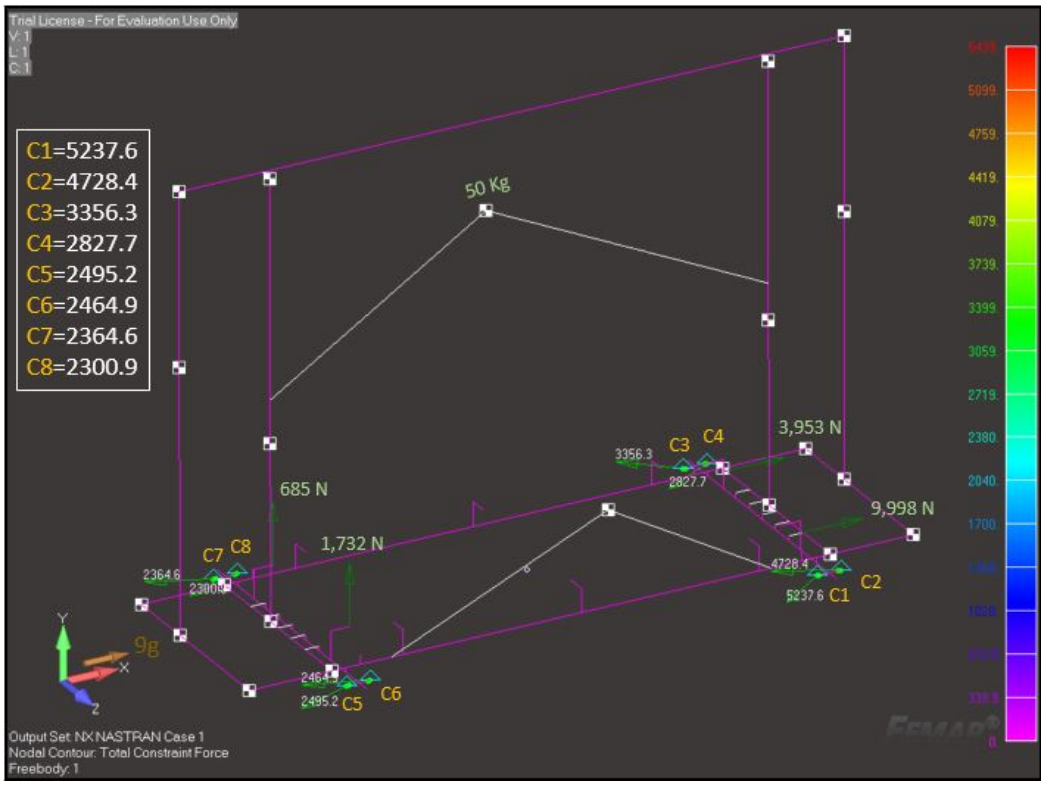

Figure A.24: Shear force analysis outputs at the interfaces between seat-track and base bar (9g fore load)

ments are rotated to a local coordinate frame, indicated for each joint in Figure A.27. The convention used for these local coordinate frames is that x is along the bolt axis and z is aligned through the line connecting the "long" direction of a bolt pattern (i.e. through the 2 bolts in a 2x1 bolt pattern, through the 4 bolts in a 4x1 bolt pattern, through the 4 bolts in a 4x2 bolt pattern, through 2 bolts in a 2x2 bolt pattern).

With all forces and moments converted into a standardized local frame for all joints, the axial and shear and forces for each joint are calculated based on the extracted forces and moments. For each different bolt pattern, moments are converted into additional axial and shear forces in a different way. Diagrams indicating these relationships for various joint examples are provided in Figure A.29 through Figure A.31.

Sample Femap joint force and moment outputs for the 9g-fore load case are provided in Table 4, and then converted into axial and shear forces on the worst case bolt for each joint. The worst case factors of safety for the 9g-fore load case are 1.1 at joints J-3 and J-6, for axial loading. Recall that these analyses ignore the additional brackets at each joint that would increase the margin of safety further.

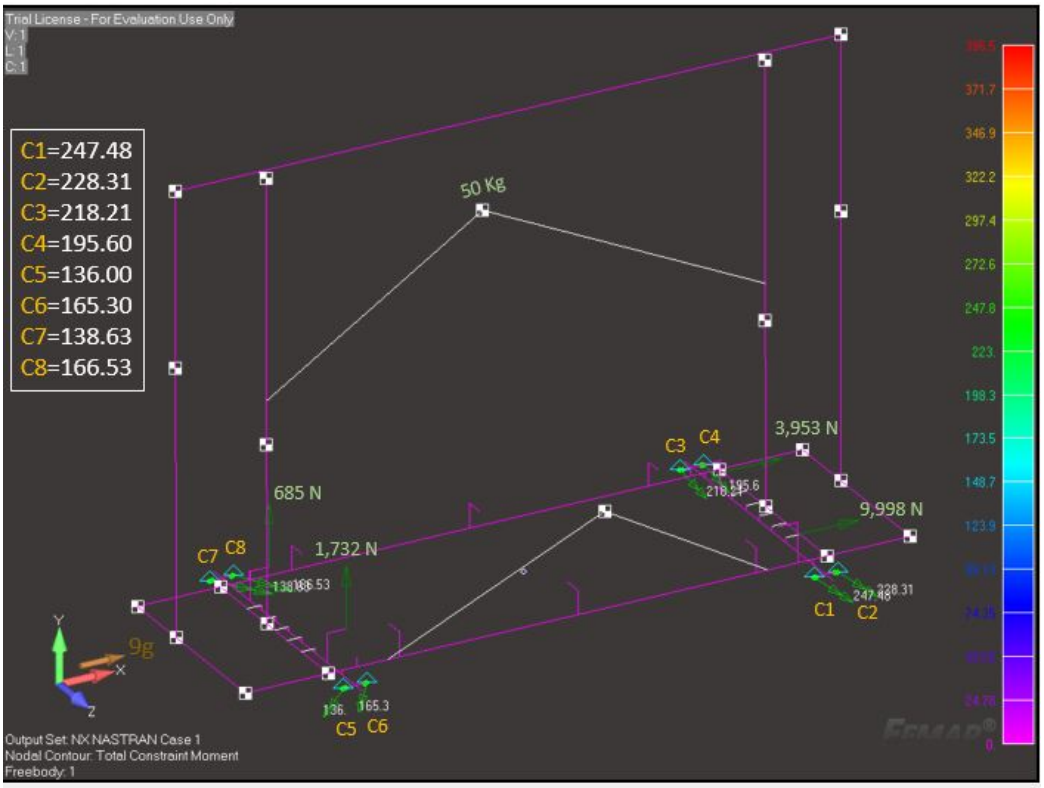

Figure A.25: Total bending moment analysis outputs at the interfaces between seat-track and base bar (9g fore load)

A.3.5 Sandbox catcher analysis -9g fore load case

To select the proper bolts for the sandbox catcher blocks interfacing the frame structure, sandbox reaction forces, as derived and, are applied to each of the blocks (see Figure A.32). Axial forces in each bolt and shear forces at the base of each block, are calculated by static equilibrium equations. The worst case bolt(s) (with highest axial and/or shear force) are used to size the fasteners. M8 bolts provide sufficient safety factor. The bolts will pass through through-holes in the structural frame and be threaded directly into the base bars to a depth of at least 2x bolt diameters.

A.3.6 Sandbox joint analysis -9g fore load case

For analyses of the sandboxs structural integrity, a separate Femap model was created of the sandbox itself. The model consists of 2D plate elements joined together with glue constraints. For the front face of the sandbox, two plates are stacked representing the aluminum wall (with window cut-out) and the pane of tempered glass behind it. Modeling and analysis of the glass is discussed in more detail in the subsequent subsection.

The load applied to this model consists of the geostatic stress caused by the soil itself as it is accelerated. In the 9g-fore load case, for example, the soil is pressed into

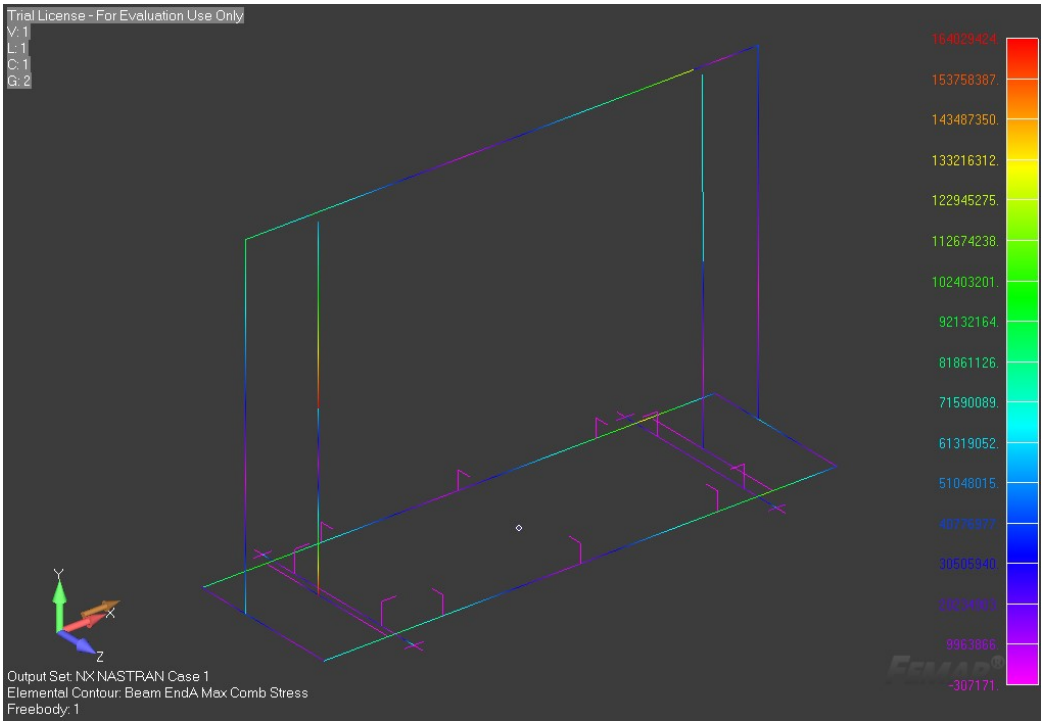

Figure A.26: Total bending moment analysis outputs at the interfaces between seat-track and base bar (9g fore load)

one side of the sandbox. The pressure load on this face is analogous to that applied to a foundation, based on the effective weight of the soil acting in the direction of the acceleration (p = $\rho_{soil} * V_{soil} * 9g/A_{wall} = \rho_{soil}$*L*9g). The pressure loads on the front and rear walls of the sandbox are analogous to lateral pressure applied to a retaining wall. Such pressure loads increase linearly from the surface of the soil along the direction of the acceleration; specifically, p(x) = (1-sinϕ) ρ_{soil}*x*9g for x $\in$ (0, L), where is the soils angle of internal friction [1]. For the soil being used, ϕ=(32^o,42^o) [2]. Therefore, the worst case pressure occurs when the soil is loosest (ϕ=32^o).

Glue forces/moments resulting from the above modeling and loading are extracted from Femap/NASTRAN, and further analyzed at each of the 8 sandbox joints. The joints in the system consist of brackets fastened to both plates with a pair of bolts (usually combined with lock nuts, or in some cases threaded into the sandbox wall plate itself). The glue constraint in Femap/NASTRAN provides force and moment outputs at many nodes along each joints line of contact. These node outputs are grouped by their proximity to a pair of bolts in the system, and summed to evaluate the groups total effect on that closest pair of bolts. As the two bolts are always oriented at right angles to one another, the summed glue forces and moments are applied and analyzed separately for each bolt (i.e. that fastened to one surface of the bracket, and the other). Because of the different orientations, glue force that acts axially on one bolt of the pair will act in shear on the other. The 8 joints thus can be viewed as 16 lines of bolts, as identified in Figure A.34.

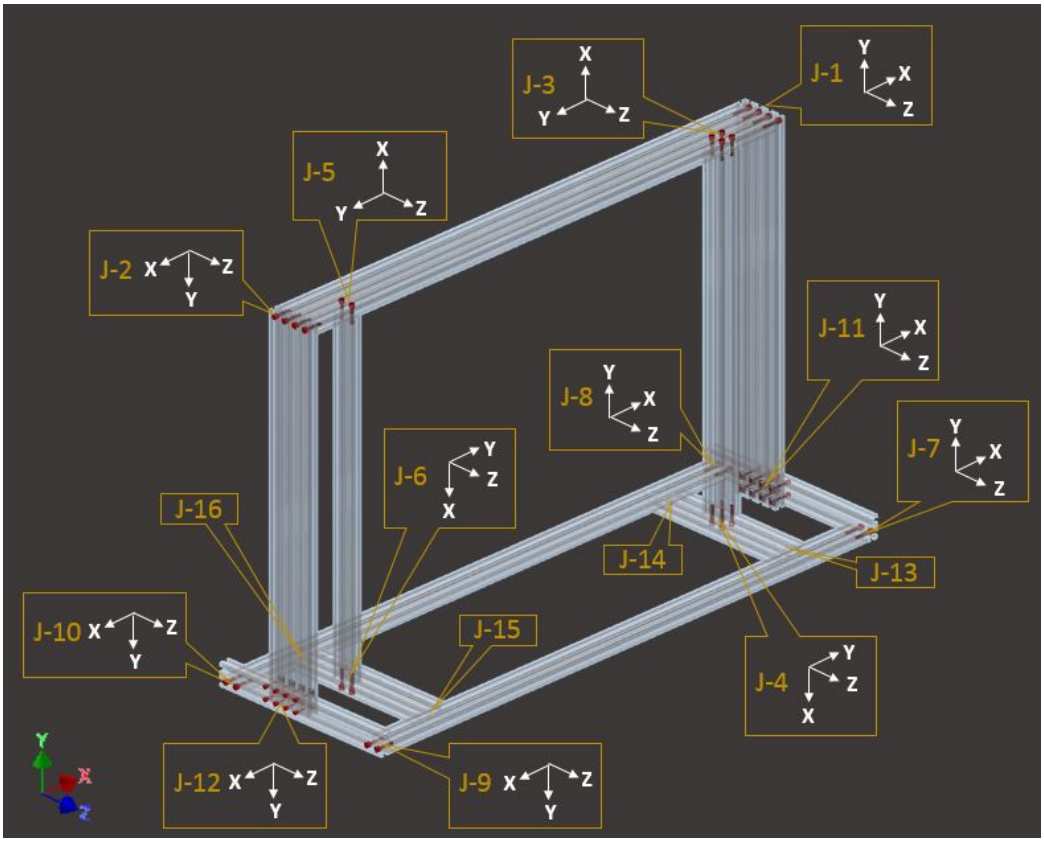

Figure A.27: Total bending moment analysis outputs at the interfaces between seat-track and base bar (9g fore load)

The analysis described above is done for every bolt associated with a sandbox joint.

A.3.7 Sandbox glass stress analysis - 9g fore and 3g lateral starboard load cases

Stress analysis is performed to quantify the risk of the glass breaking due to the geo-static loads described in the previous subsection. The pane of glass that constitutes the window of the sandbox is secured behind the front aluminum plate. Some of the glass is behind the window opening (the window section) and some is behind the aluminum plate (non-window section). The structural response of these 2 sections will be different. In the Femap/NASTRAN model, the Youngs modulus of the non-window section of glass is considered to be 1000 times smaller than the window section (72 GPa and 72 MPa, respectively). The FEM uses a glued condition between the glass and aluminum while the actual condition is a contact-only press fit. In the modeled glued condition, the glass artificially increases the stiffness. By reducing the glass modulus, the glass is removed from the stiffness calculation resulting in a conservative calculation. Modeling the full glass pane with a modulus of 72 GPa results

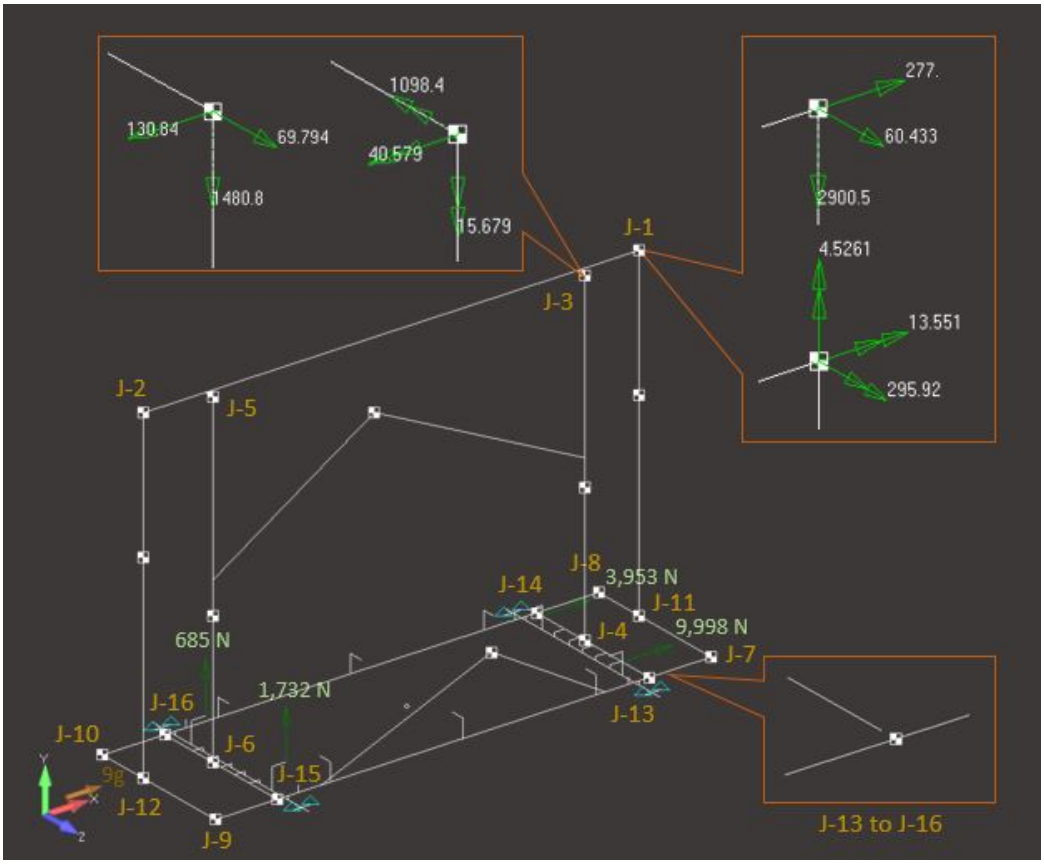

Figure A.28: Total bending moment analysis outputs at the interfaces between seat-track and base bar (9g fore load)

in a lower maximum stress (i.e. less conservative result). The stress distribution in the glass structural element is analyzed and compared to typical design stress for tempered glass (77 MPa) to compute a safety factor. As shown in Figure A.35, the maximum VonMises stress for the 9g fore load case is 43 MPa, resulting in a safety factor of 1.8.

As shown in Figure A.35, the maximum VonMises stress for the 3g lateral starboard load case (where the soil is bearing mainly on the glass wall) is 10 MPa, resulting in a safety factor of 7.6.

A.3.8 Pressing plate unit analysis

Figure A.37 shows the design of the pressing unit and its integration into the sandbox unit. It can be observed in this figure that the aluminum extrusion is encapsulated inside the slider attachment and the whole structure is rigidly connected. The pressing plate is enclosed from three sides (z+,x+, x- in the figure) within the sandbox, so for any emergency load cases along these three directions, the pressing plate unit will be constrained/captive by the sandbox structure.

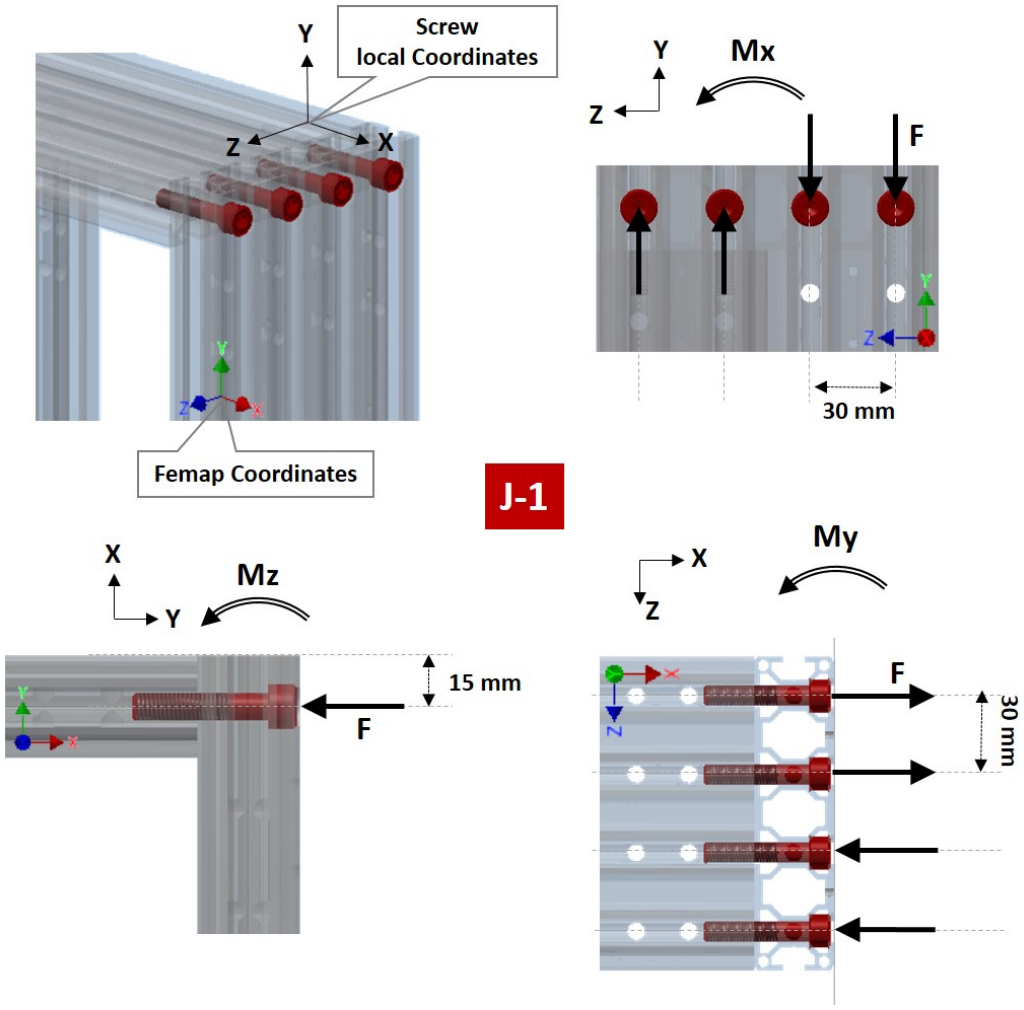

Figure A.29: Diagram relating moments to additional components of axial and shear force, for joint J-1 (4x1 bolt pattern)

The sliders load capacity is 1070 N / pair, and the calculated load of the pressing plate unit for 3g and 6g acceleration are 345, and 690 N, respectively (see Figure A.38). Therefore the minimum safety factor relative to the load applied by the 3g (y+) and 6g (y-) of the pressing plate unit is 1.5

In the z- direction (see Figure A.38) the motion of the sliders is constrained, both by the closing of the pneumatic cylinders and by stopper ends on the sliders themselves. However, analysis is performed to ensure the pressing plate unit does not detach from the sliders. 8 fasteners (M4 screw) at the interface between the pressing plate unit to the sliders is analyzed for 3g acceleration in z- direction (see Figure A.39), resulting to a safety factor of 6.5 for each M4 screw.

As shown in Figure A.40, aluminum blocks prevent the test unit from exiting its slider in the fore or aft directions. Dampers are mounted to these blocks to absorb any potential shocks and ensure any contact between the test item unit and blocks can be analyzed statically. Depending on the final placement and orientation of

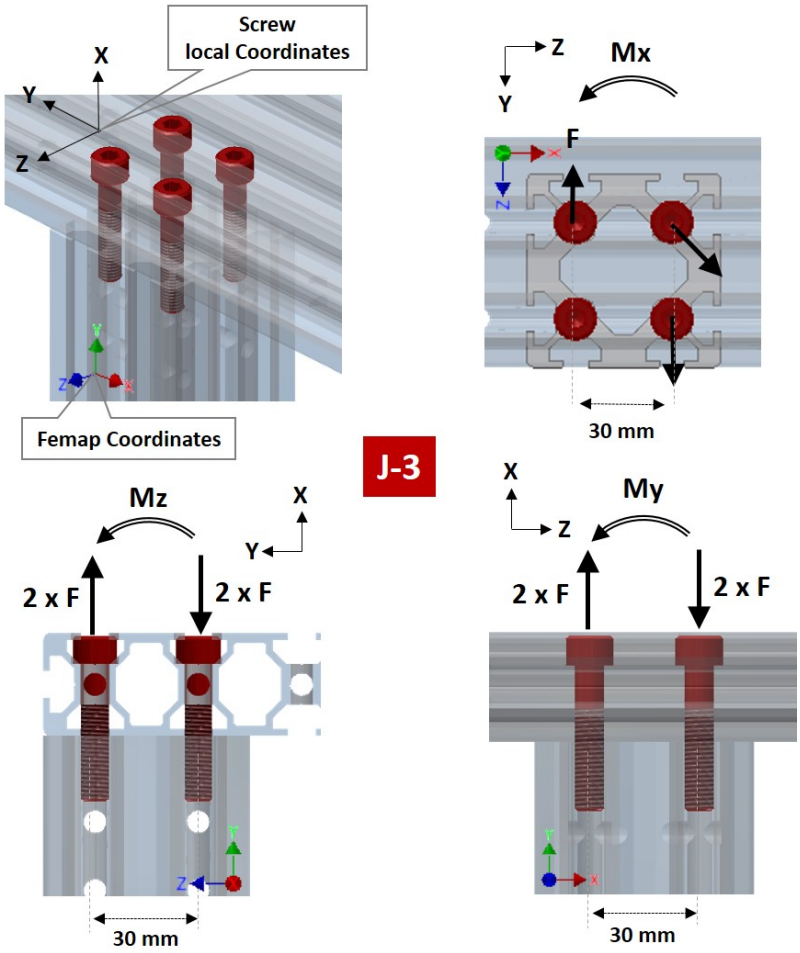

Figure A.30: Diagram relating moments to additional components of axial and shear force, for joint J-3 (2x2 bolt pattern)

the experiment in the Falcon 20 cabin, the 9g-fore load case may see the test unit contacting one or the other end of the slider. At one end, there are simple aluminum stopper blocks fastened to the end of the slider (also made of aluminum). Mounted to the other end of the slider, the motor unit acts as a stopper block in the other direction.

The fastener preload (and Al-Al friction coefficient) defines a maximum shear load, analogously to analyses in prior subsections. With the selected fasteners, the factor of safety relative to the force applied by the wheel test unit is 9 (See Figure A.41). At the motor unit end, an additional load is applied due to the acceleration of the motor mass in 9g. Here, both axial and shear loads are analyzed analogously to analyses in prior subsection (See Figure A.42).

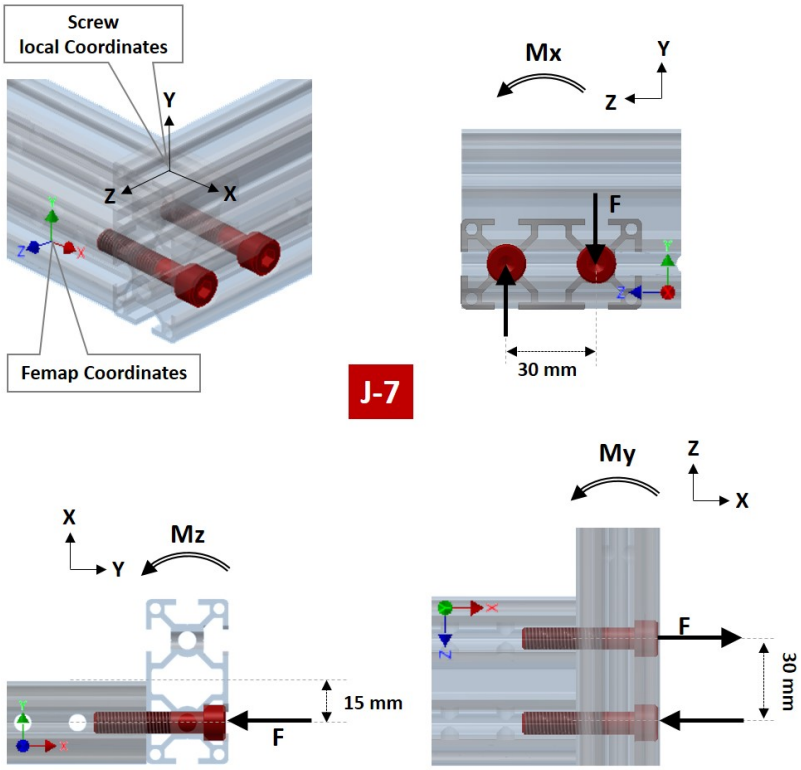

Figure A.31: Diagram relating moments to additional components of axial and shear force, for joint J-7 (2x1 bolt pattern)

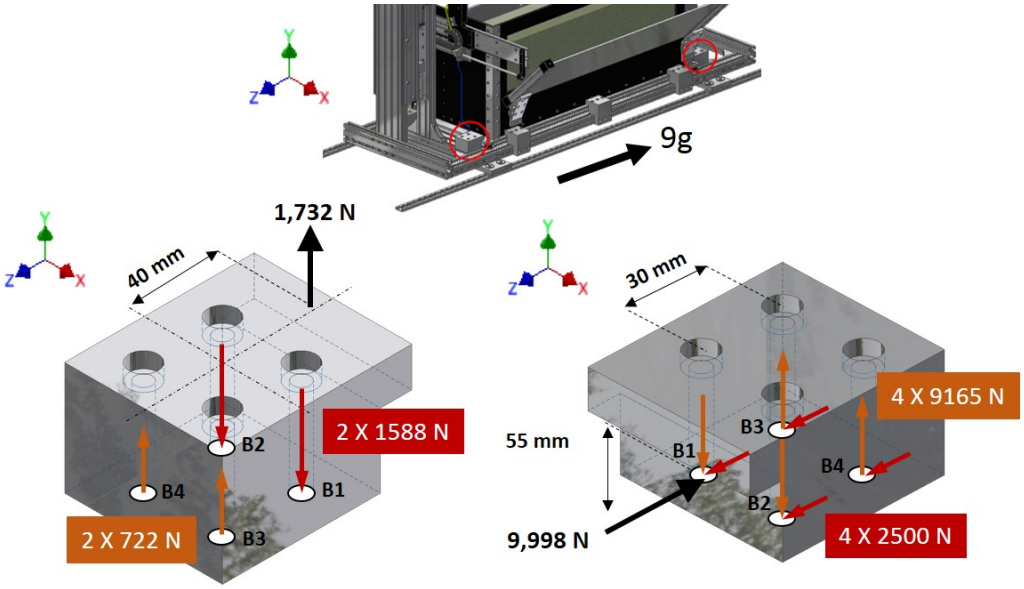

B1 & B2	M6	M8
Major diameter [mm]	6	8
Pitch [mm]	1	1.25
Tensile strength [Mpa]*	1,300	1,300
Yield strength [Mpa]*	1,170	1,170
Percentage of preload [%]	70%	70%
Friction coefficient (Al to Al)	0.21	0.21
Axial force in 9g [N] (From Calculation)	1,588	1,588
Shear force in 9g [N] (From Calculation)	0	0
Minor diameter	4.917	6.647
Effective diameter [mm]	5.06	6.83
Effective cross section area [mm^2]	20.1	36.6
Preload [N]	16,481	29,982
Max permited axial force [N] (After preload)	9,679	17,609
9g Normal force [N]	14,893	28,394
9g friction force [N]	3,128	5,963
Safety Factor-Axial	6.10	11.09
Safety Factor-Shear	Not/C	Not/C

B1 to B4	M6	M8
Major diameter [mm]	6	8
Pitch [mm]	1	1.25
Tensile strength [Mpa]*	1,300	1,300
Yield strength [Mpa]*	1,170	1,170
Percentage of preload [%]	70%	70%
Friction coefficient (Al to Al)	0.21	0.21
Axial force in 9g [N] (From Calculation)	9,165	9,165
Shear force in 9g [N] (From Calculation)	2,500	2,500
Minor diameter	4.917	6.647
Effective diameter [mm]	5.06	6.83
Effective cross section area [mm^2]	20.1	36.6
Preload [N]	16,481	29,982
Max permited axial force [N] (After preload)	9,679	17,609
9g Normal force [N]	7,316	20,817
9g friction force [N]	1,536	4,372
Safety Factor-Axial	1.06	1.92
Safety Factor-Shear	0.61	1.75

Figure A.32: Calculation for bolt selection of catcher block interface to frame structure (9g fore load)

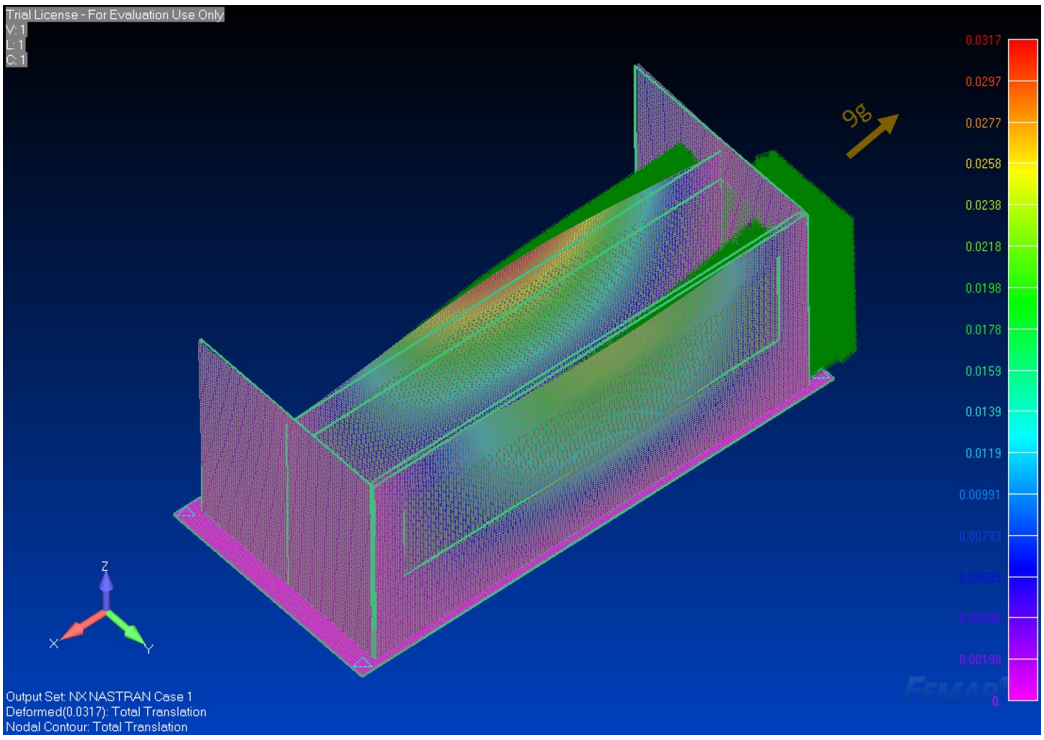

Figure A.33: Femap model of sandbox with geostatic loading (9g-fore load case)

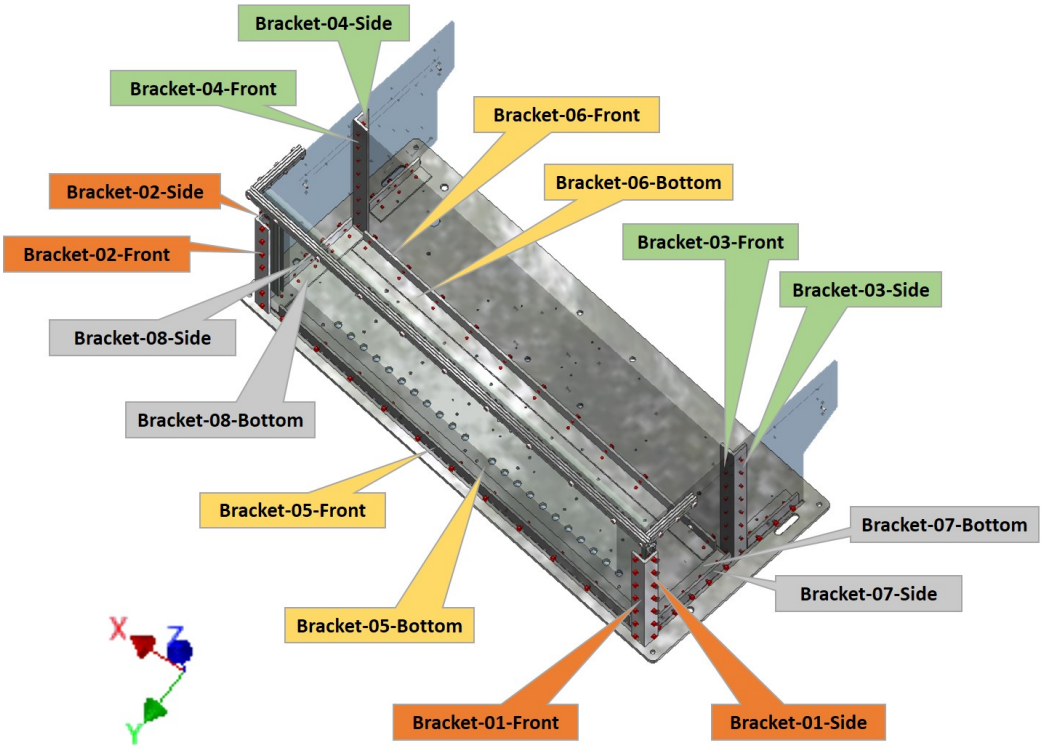

Figure A.34: Sandbox joints, with bracket faces at each of the 8 joints identified

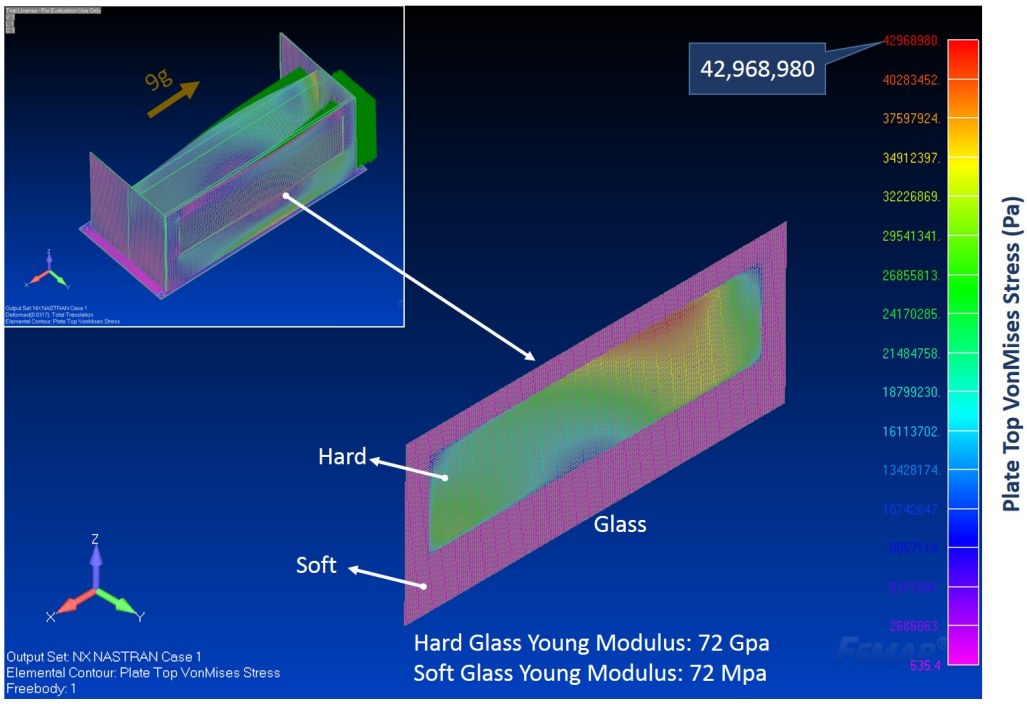

Figure A.35: VonMises stress (9g fore load case) in the tempered glass constituting the window of the sandbox. Higher deflection and stress occurs in the section of exposed glass than in the section fixed behind aluminum.

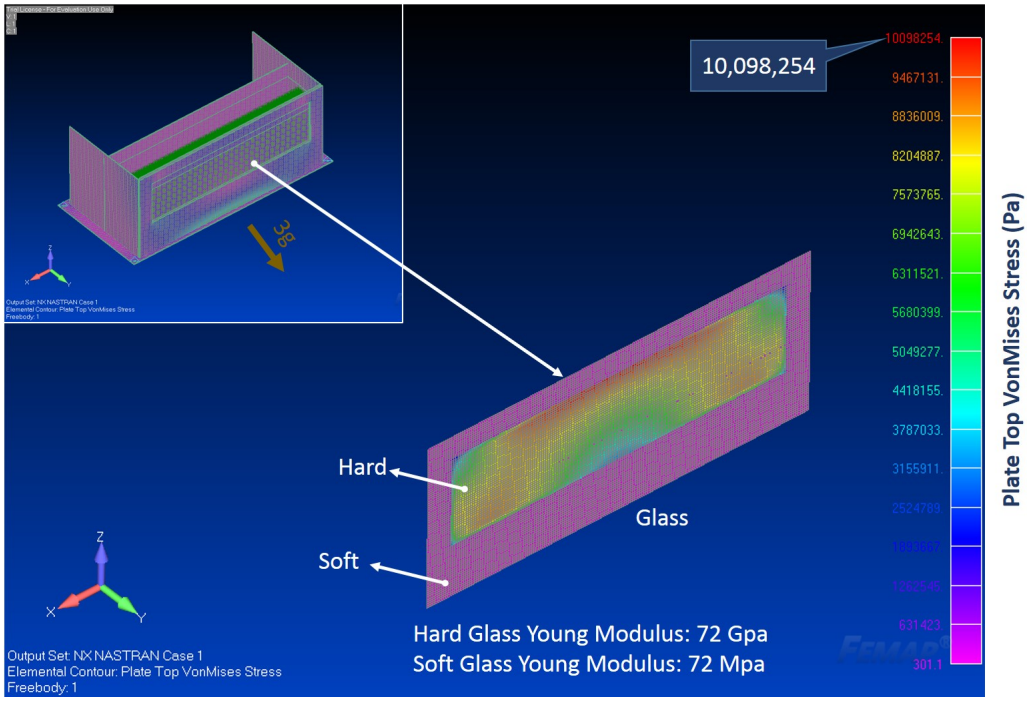

Figure A.36: VonMises stress in the tempered glass of the sandbox (3g lateral starboard load case).

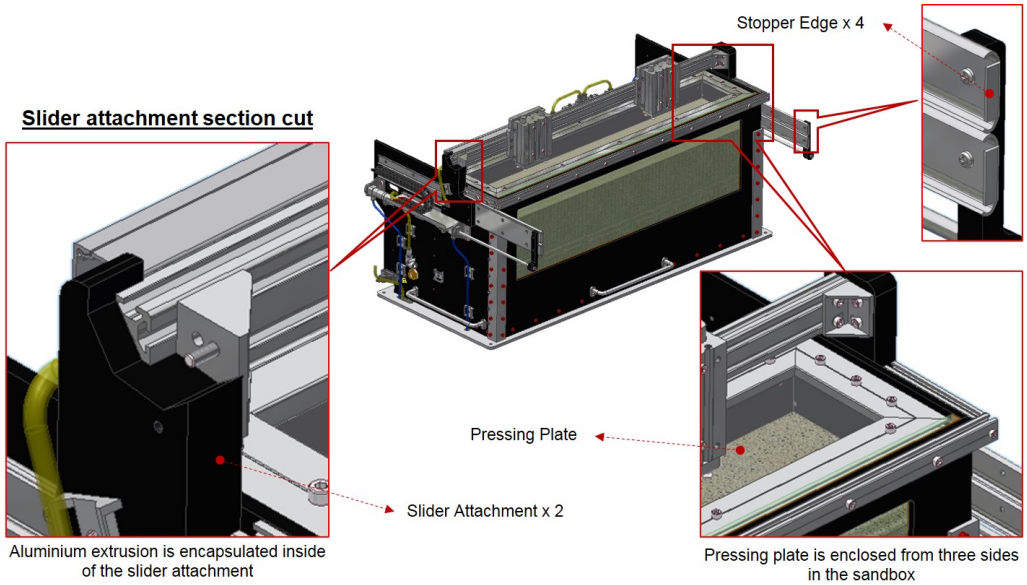

Figure A.37: Pressing plate unit, highlighting captive/constrained elements of the design.

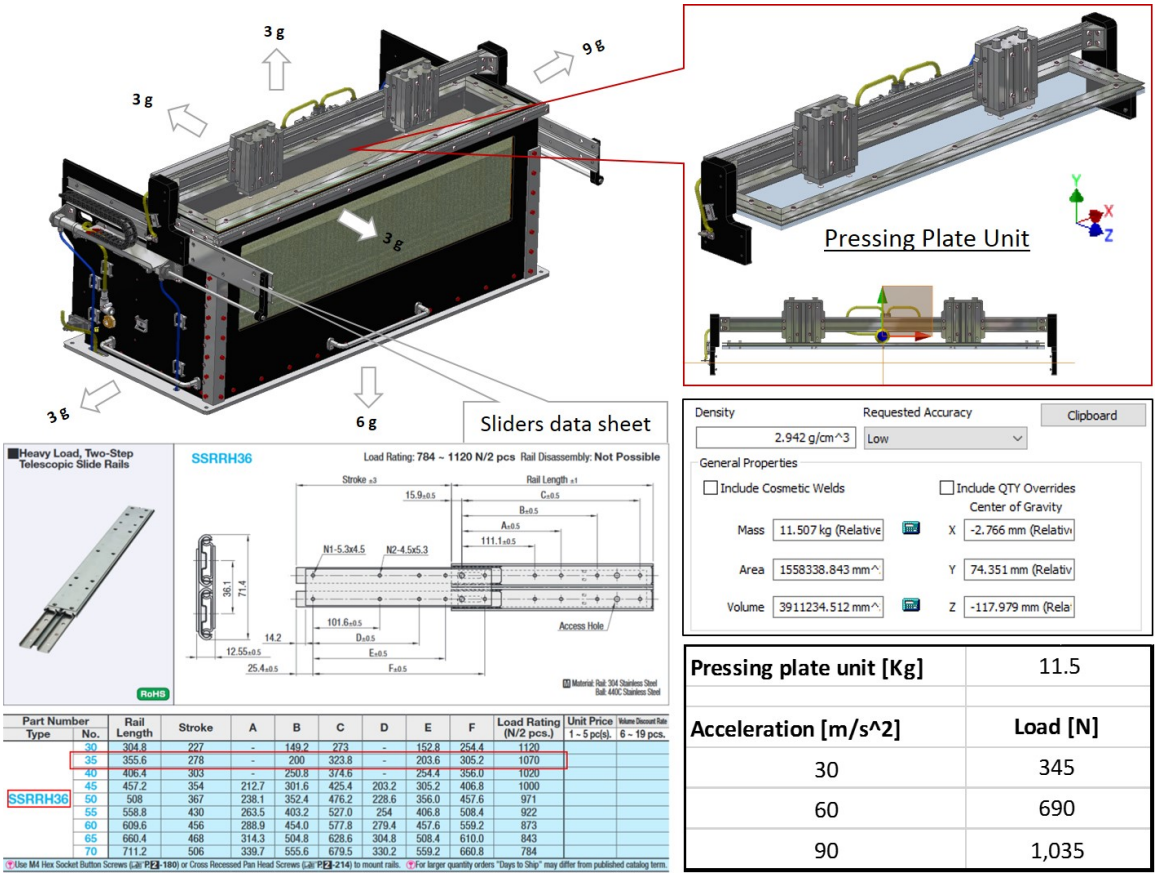

Part Number Type	No.	Rail Length	Stroke	A	B	C	D	E	F	Load Rating (N/2 pcs.)	Unit Price 1 ~ 5 pc(s).	6 ~ 19 pcs.
SSRRH36	30	304.8	227	-	149.2	273	-	152.8	254.4	1120		
	35	355.6	278	-	200	323.8	-	203.6	305.2	1070		
	40	406.4	303	-	250.8	374.6	-	254.4	356.0	1020		
	45	457.2	354	212.7	301.6	425.4	203.2	305.2	406.8	1000		
	50	508	367	238.1	352.4	476.2	228.6	356.0	457.6	971		
	55	558.8	430	263.5	403.2	527.0	254	406.8	508.4	922		
	60	609.6	456	288.9	454.0	577.8	279.4	457.6	559.2	873		
	65	660.4	468	314.3	504.8	628.6	304.8	508.4	610.0	843		
	70	711.2	506	339.7	555.6	679.5	330.2	559.2	660.8	784		

Use M4 Hex Socket Button Screws (PZ3-180) or Cross Recessed Pan Head Screws (PZ3-214) to mount rails. For larger quantity orders "Days to Ship" may differ from published catalog term.

Pressing plate unit [Kg]	11.5
Acceleration [m/s^2]	**Load [N]**
30	345
60	690
90	1,035

Figure A.38: Details of pressing plate unit for static analysis

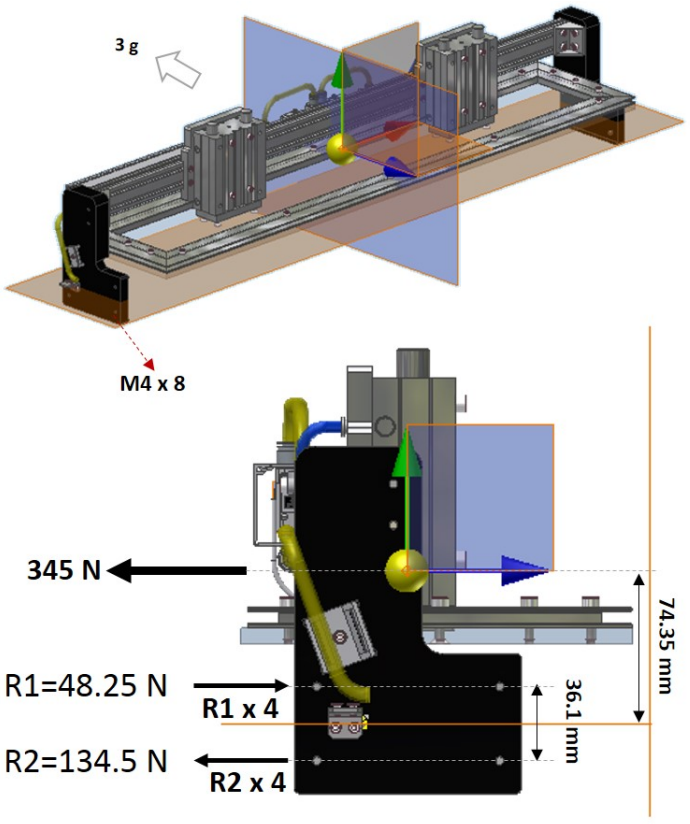

	M4
Major diameter [mm]	4
Pitch [mm]	0.7
Tensile strength [Mpa]*	1040
Yield strength [Mpa]*	945
Percentage of preload [%]	70%
Friction coefficient (Al to ST)	0.15
Axial force in 9g [N] (From Calculation)	0
Shear force in 9g [N] (From Calculation)	134.5
Minor diameter	3.242
Effective diameter [mm]	3.34
Effective cross section area [mm^2]	8.8
Preload [N]	5,807
Max permited axial force [N] (After preload)	3,323
9g Normal force [N]	5,807
9g friction force [N]	871
Safety Factor (Axial)	1.57
Safety Factor (Shear)	6.48

* Tensile and yield strength data taken from Unbrako product guide

Figure A.39: Analysis results of fasteners for pressing plate unit (3g lateral load)

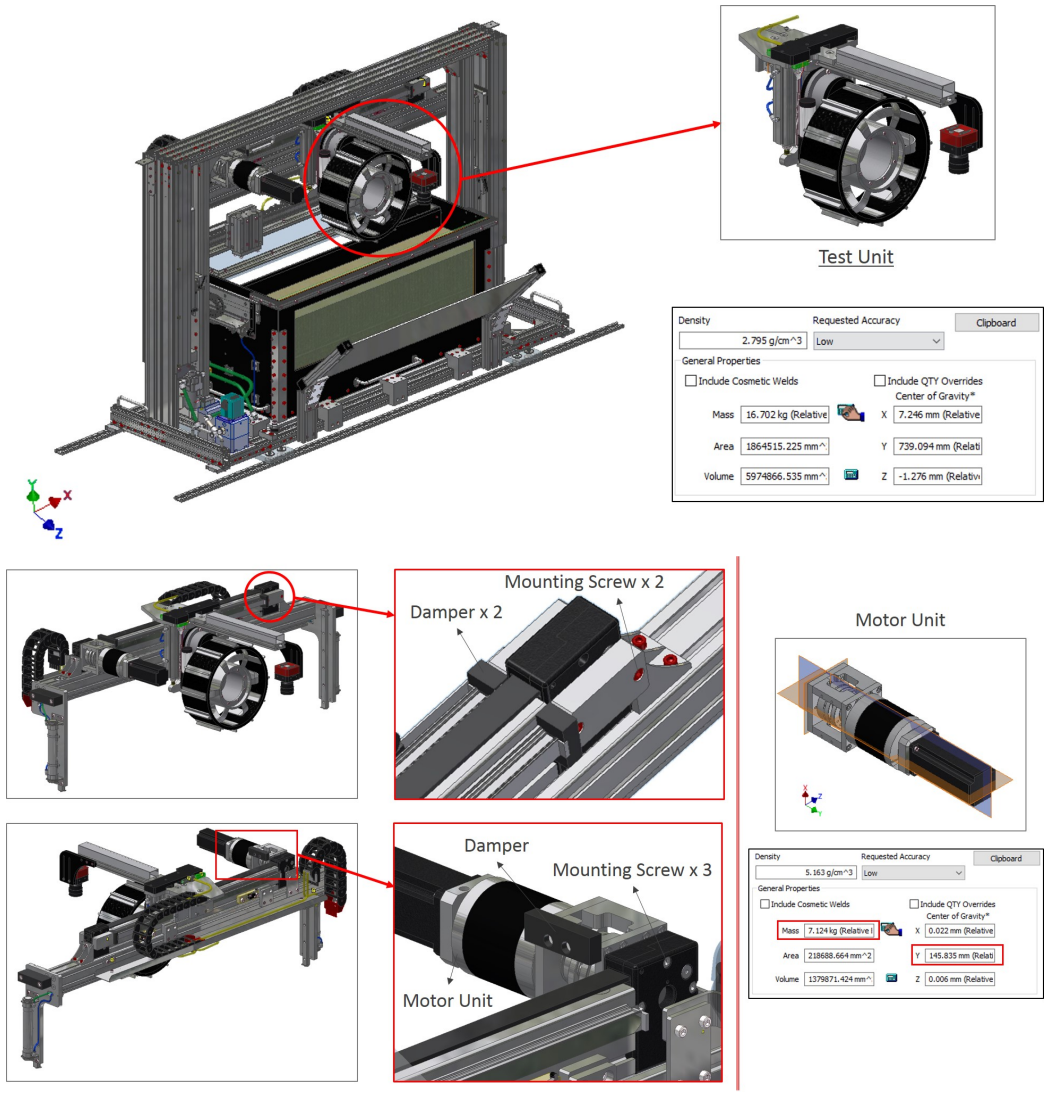

Figure A.40: Test item unit capture and damping hardware

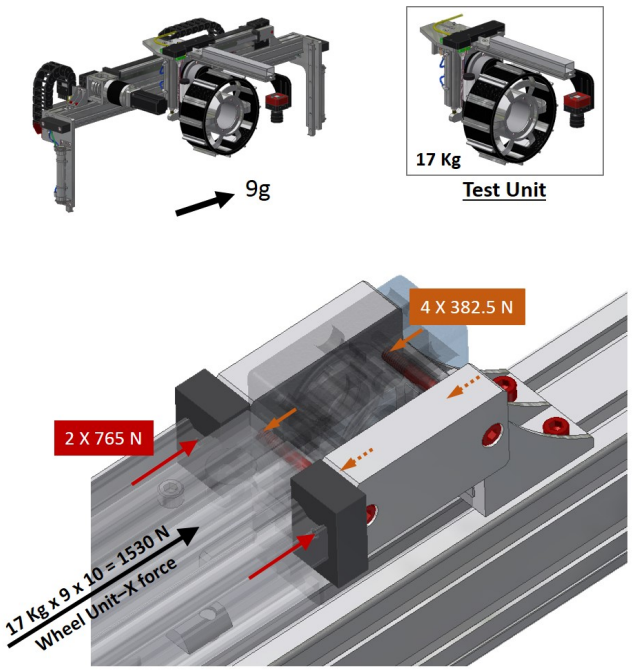

	M6
Major diameter [mm]	6
Pitch [mm]	1
Tensile strength [Mpa]	1,300
Yield strength [Mpa]	1,170
Percentage of preload [%]	70%
Friction coefficient (Al to Al)	0.21
Axial force in 9g [N] (From Calculation)	0
Shear force in 9g [N] (From Calculation)	382.5
Minor diameter	4.917
Effective diameter [mm]	5.06
Effective cross section area [mm^2]	20.1
Preload [N]	16,481
Max permited axial force [N] (After preload)	9,679
9g Normal force [N]	16,481
9g friction force [N]	3,461
Safety Factor (Axial)	Not/C
Safety Factor (Shear)	9.05

* Tensile and yield strength data taken from Unbrako product guide

Figure A.41: Analysis of stopper blocks at end of linear actuator (9g load case)

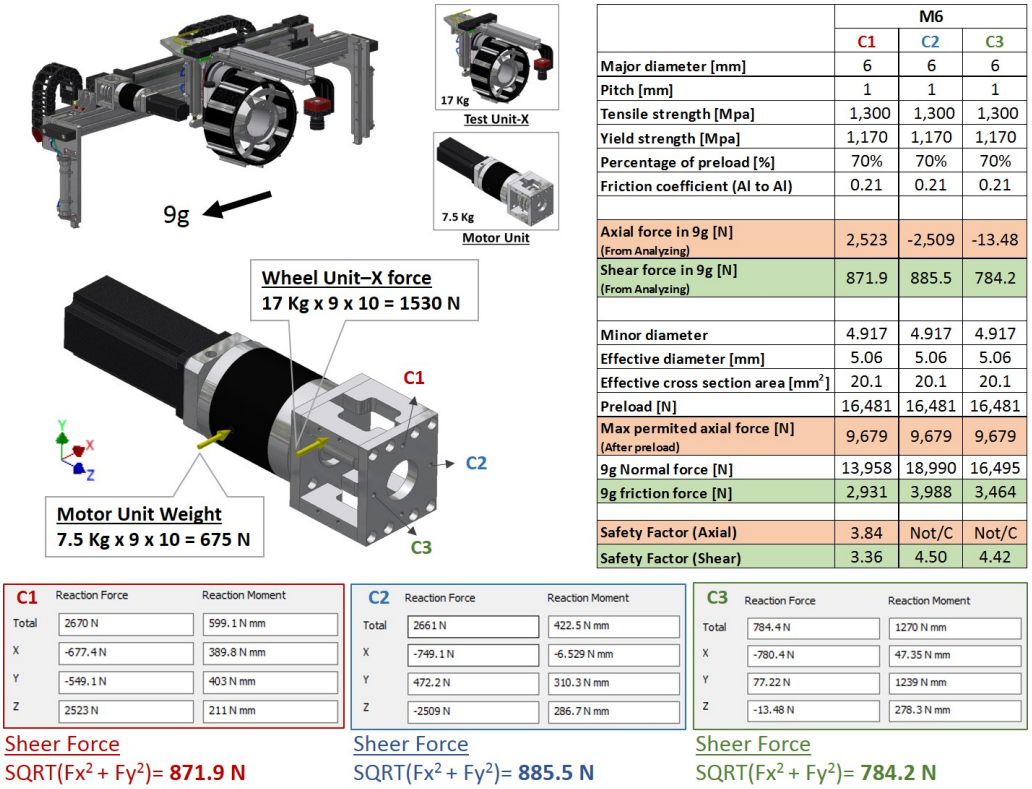

	M6		
	C1	C2	C3
Major diameter [mm]	6	6	6
Pitch [mm]	1	1	1
Tensile strength [Mpa]	1,300	1,300	1,300
Yield strength [Mpa]	1,170	1,170	1,170
Percentage of preload [%]	70%	70%	70%
Friction coefficient (Al to Al)	0.21	0.21	0.21
Axial force in 9g [N] (From Analyzing)	2,523	-2,509	-13.48
Shear force in 9g [N] (From Analyzing)	871.9	885.5	784.2
Minor diameter	4.917	4.917	4.917
Effective diameter [mm]	5.06	5.06	5.06
Effective cross section area [mm^2]	20.1	20.1	20.1
Preload [N]	16,481	16,481	16,481
Max permited axial force [N] (After preload)	9,679	9,679	9,679
9g Normal force [N]	13,958	18,990	16,495
9g friction force [N]	2,931	3,988	3,464
Safety Factor (Axial)	3.84	Not/C	Not/C
Safety Factor (Shear)	3.36	4.50	4.42

Figure A.42: Analysis of motor unit as a stopper block for test item unit (9g load case)

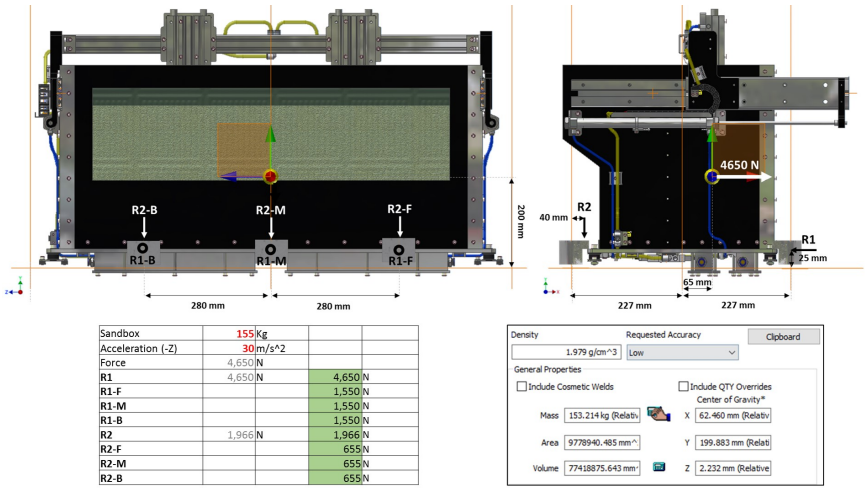

Sandbox	155	Kg		
Acceleration (-Z)	30	m/s^2		
Force	4,650	N		
R1	4,650	N	4,650	N
R1-F			1,550	N
R1-M			1,550	N
R1-B			1,550	N
R2	1,966	N	1,966	N
R2-F			655	N
R2-M			655	N
R2-B			655	N

Figure A.43: Rigid sandbox model for determining reaction forces on the sandbox catchers (3g-port load case shown)

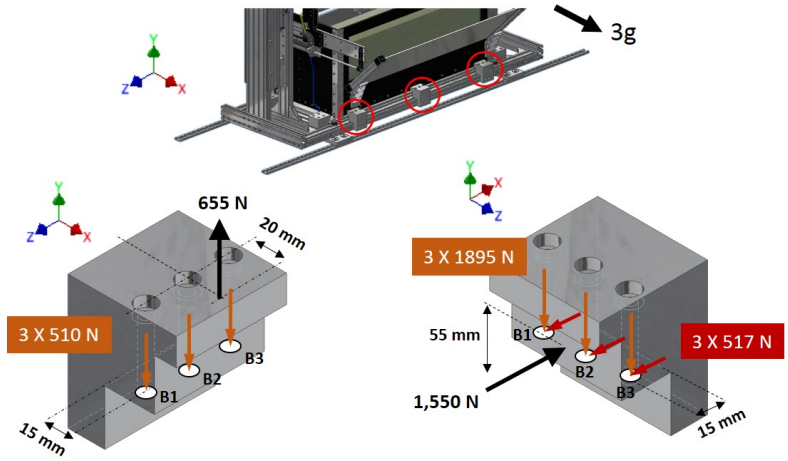

B1 to B3	M6
Major diameter [mm]	6
Pitch [mm]	1
Tensile strength [Mpa]*	1,300
Yield strength [Mpa]*	1,170
Percentage of preload [%]	60%
Friction coefficient (Al to Al)	0.21
Axial force in 9g [N] (From Calculation)	510
Shear force in 9g [N] (From Calculation)	0
Minor diameter	4.917
Effective diameter [mm]	5.06
Effective cross section area [mm^2]	20.1
Preload [N]	14,127
Max permited axial force [N] (After preload)	12,034
9g Normal force [N]	13,617
9g friction force [N]	2,859
Safety Factor-Axial	23.60
Safety Factor-Shear	Not/C

B1 to B3	M6
Major diameter [mm]	6
Pitch [mm]	1
Tensile strength [Mpa]*	1,300
Yield strength [Mpa]*	1,170
Percentage of preload [%]	60%
Friction coefficient (Al to Al)	0.21
Axial force in 9g [N] (From Calculation)	1,895
Shear force in 9g [N] (From Calculation)	517
Minor diameter	4.917
Effective diameter [mm]	5.06
Effective cross section area [mm^2]	20.1
Preload [N]	14,127
Max permited axial force [N] (After preload)	12,034
9g Normal force [N]	12,232
9g friction force [N]	2,569
Safety Factor-Axial	6.35
Safety Factor-Shear	4.97

Figure A.44: Calculation for bolt selection of catcher block interface to frame structure (3g-port load)